Investigating the evolution of large-scale, cyclic solar magnetic fields by Babcock-Leighton flux-transport dynamo model

PhD dissertation

Bernadett Belucz

Eötvös Loránd University, Ph.D. School in Physics
Director: Dr László Palla
Particle Physics and Astronomy Ph.D. program
Director: Dr László Palla

Supervisor
Dr Emese Forgács-Dajka
Astronomy Department,
Eötvös Loránd University
Hungary

Co-supervisor
Dr Mausumi Dikpati
High Altitude Observatory,
National Center for Atmospheric Research
Untited States of America

Budapest
2016

All we have to decide is what to do
with the time that is given us.
J.R.R. Tolkien

Foreword

Anywhere we look in the Universe, the magnetic fields exist and can be observed, whether we investigate the planetary magnetic field, solar and star activity, the role of magnetic fields in the evolution of dense clouds, or the star formation process or the large-scale magnetic fields of galaxies. Dynamo theory branch of fluid mechanics explains the origin of these magnetic fields and describes the variations over astronomical time scales. In streaming conductive fluid, electrical currents are induced from the initial magnetic field, described by the Faraday's law of induction, named after Michael Faraday who discovered in 1831 that the magnetic field interacts with an electric current to produce an electromotive force, called electromagnetic induction. According to Ampre's law, the electric currents produce magnetic field that reacts to the fluid motion, and this magnetic field is added to the initial field that is, the magnetic field grows.

The Sun's large-scale magnetic field varies on wide spatial and temporal scales. The cyclic regeneration of large-scale magnetic field produces sunspots, flares, filaments, and all phenomena at the surface and in the atmosphere, known as solar activity collectively. The cyclic variation of the large-scale component of the solar magnetic field occurs approximately 11 years. This short cycle period points to the Sun's large-scale magnetic field being created by a hydromagnetic dynamo working in the convection zone. The origin of solar activity is one of the greatest unsolved problems in astrophysics. To find the answers, over the past half a century several dynamo models have created what can be divided into four classes of large-scale dynamo models. One of them is the widely used Babcock-Leighton flux transport dynamo model, responsible to a number of successes in recent years.

This thesis is organized in five parts. The first part gives a brief history of solar physics and highlights the most important milestones in the discovery of the solar cycle and the phenomena of solar activity, as the "toolbar" of solar physics. The second part describes the mechanisms of the magnetic field generation and gives a detailed picture of the Babcock-Leighton solar dynamo model with its success and drawbacks. The remaining three parts submit our results, what are mainly grouped into two topics. One is the observed North-South asymmetry on the Sun. The other is the effect of meridional circulation, which has a key role in the Babcock-Leighton fluxtransport dynamo models.

My thesis is an overview of my research during the doctoral fellowship at the Eötvös Lorand University and the fellowships at the High Altitude Observatory (HAO) of the National Center for Atmospheric Research (NCAR) in the United States. For the help and support, for the unforgettable and very useful time at NCAR HAO, as well as for the work of publicated papers I am indebted to my co-supervisor, Mausumi Dikpati.

1. Discovering the Solar Cycle

1.1. Milestones in the Discovery of the Solar Cycle

Earliest records of visible dark spots on the Sun came from the 4th century BC. In Europe, sunspots were first observed telescopically by Fabricius and Herriot in 1610. In 1612, Scheiner also published his observations, and he thought that spots are planets. Galileo Galilei disagreed, he inferred in the "Istoria e demonstrazioni alle machi solari" that sunspots are on the solar surface. Starting from 1645 to 1715, sunspots became extremly rare, as noted by solar observers, Cassini and Hevelius (Ribes & Nesme-Ribes, 1993).

The solar cycle, average eleven-year cycle for the frequency of sunspot presence, was discovered by Samuel Heinrich Schwabe in 1843 (Schwabe, 1843). Five years later, Wolf defined the relative sunspot number, that measures the number of sunspots and groups of sunspots present on the solar surface (Wolf & Brunner, 1936). When Schwabe discovered the sunspot cycle, some years later, Wolf, Sabine and Gautier recognized that solar cycles affected the Earth's magnetic field, connected with the geomagnetic storms (Cliver, 2005). Carrington's work is given a lot to solar physics. Carrington observed the sunspots for many years (1855-1861). He accurately identified the rotation rate of the Sun (Carrington, 1863) and discovered the migration of sunspots during the solar cycle (Carrington, 1858) and observed a solar flare for the first time (Carrington, 1860). In 1861, Spörer predicts the distribution of sunspot latitudes during a solar cycle, (Spörer's law, Spörer, 1889).

In 1874, Langley gave a detailed description of the Sun's photosphere structure, called granulation (Langley, 1874). He discovered that granules represented the points where hot currents were ascending from the interior of the Sun and cooler currents descend among the hot cells. Spicules were discovered three years later by Father Angelo Secchi of the Vatican Observatory in Rome. In 1908, Hale observed the Zeeman effect in sunspots using a spectroheliograph. This was the first indication that sunspots were basically magnetic phenomena (Hale, 1908). In 1909, John Evershed discovered the Evershed effect, the radial flow of plasma across the penumbra of sunspots from the inner border with the umbra towards the outer edge, (Evershed, 1909). Biermann's (1941) suggestion that sunspots are relatively cool owing to the inhibition of convection by their magnetic field, is now generally considered to be basically correct, although it is realized that significant

convective transport of energy must occur in order to maintain the brightness of umbra, (Meadows, 1970).

In 1934, Cowling published an anti-dynamo theorem, an axisymmetric magnetic field cannot be maintained via dynamo action. Hans Bethe won the Nobel Prize in Physics in 1967 for his work on the theory of stellar nucleosynthesis. He proposed the carbon-nitrogen-oxygen and proton-proton chains as an explanation for the source of solar energy in 1938 (Bethe & Critchfield, 1938). Some years later, in 1951, laboratory experiments began on the magnetic containment of plasma to fusion at 10^6 K among light atoms and release energy. In 1952, Babcock invented the magnetograph to give a great improvment to measurement of solar magnetic fields.

The five-minute solar oscillations were discovered by Leighton in 1962. Helioseismology is a powerful tool to study the interior of the Sun from surface observations of naturally-excited internal acoustic and surface-gravity waves. The fundamental data of modern helioseismology are high-resolution Doppler images of the Suns surface. Today, the development of local helioseismology is fuelled by high-quality data from space and ground based networks. The methods and the results of the helioseismology are outside of the thesis topic. A detailed summary about helioseismology is (Gizon & Birch, 2005).

1.2. Indicators of Solar Magnetic Cycle

The observation and study of sunspots was the first researches on solar activity. The 11-year solar cycle is characterized by reduction and increase in the numbers of sunspots and sunspot groups. There are other solar activity indicators on the Sun, including the solar flares, the coronal mass ejections, the 10.7 radio flux and the total solar irradiance. There are also indicators on the Earth, including ^{14}C and ^{10}Be radioisotopes in tree rings and ice cores and geomagnetic activity, what are varying in association with the sunspots. Near the spots, bright torches called faculae are seen many times. In later spectroheliograph, observations made in chromospheric lines, bright plage regions were seen across the whole disk in the chromosphere of the Sun closely to faculae and sunspots in the photosphere below. Accordingly, plage occurs most visibly near a sunspot region. The lengthwise, dark filaments also stand out by these narrow-band observations in the neighborhood of the spots and plages. A prominence is a large, bright, gaseous feature extending outward from the Sun's surface, often in a loop shape. Prominences are anchored to the Sun's surface in the photosphere, and extend outwards into the Sun's corona. Prominences

and filaments are really the same, but they look bright or dark depending on what is in the background. The extended areas where spots, faculae, plages, and filaments occur together are called active regions, are also the locations of powerful explosions observed as flares.

Based on our current knowledge, the phenomena of solar activity are directly connected with the Sun's strong and complex magnetic field. Because the so-called α-effect of the Babcock-Leighton flux-transport dynamo model originates in decay of the tilted bipolar active regions, primarily I dealt with sunspots in detail in this section of the thesis.

1.2.1. Structure of Sunspots

Sunspots are temporary phenomena on the Sun's photosphere. The grand sunspots can have a temperature of 3700°C, which is much lower than the temperature of the photosphere, about 5750°C. A typical structure of the sunspots consists of dark featureless umbra at the core of a spot and less dark penumbra that surrounds it that has a filamentary structure, with largely radial rays that are alternately bright and dark.

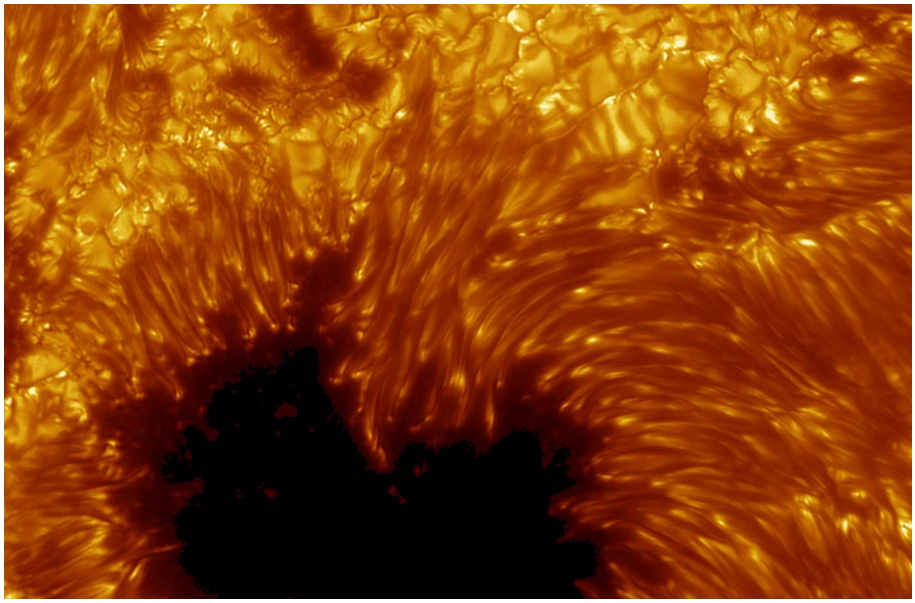

Figure 1: *High-resolution white-light images of a large sunspot. (Source: http://apod.nasa.gov)*

Solar pores are sunspots lacking penumbrae, below about 2000 km in diameter and represent the first stage of sunspot evolution. The typical lifetimes of solar pores are a

few tens of minutes, in contrast with sunspots, which last several hours up to days and even weeks. The fine structure of umbra includes umbral dots and light bridges. The penumbra extends the spot diameter to 50000 km or more in the very largest spots. The ordinary shape of the penumbra is generally irregular and depends significantly on the evolutionary stage of particular sunspot. The mainly radial fine structures of penumbra are bright and dark elongated penumbral lanes. For widespread overview the sunspot structure, read (Solanki, 2003).

The spots are grown from pores. The pores are up to about 2500 km and are brighter than a sunspot's umbra. Only near the active regions observed pores turn into spots. Not all pores develop into sunspot regions, but those that grow into sunspots by coalescence of smaller spots and development of the penumbra, go through an interesting evolution over a period of hours to days. Subsequent growth of spots can be extremely rapid, and their maximum area can be achieved within 1-5 days (Figure 2). The largest spots tend to form in the side of bipolar group. Follower spots tend to be smaller and greater in number. The Zurich classification system describe the evolution of sunspot groups through a different morphological stages.

The process of spot group decay is well observed at the photosphere. The decay rate is different for large stable spots and for small spots, independing of area. Diffusion carries away small unipolar magnetic elements from the edge of the spots into the plage, intensifying the network around active region (stages G, H and J). Horace W. Babcock developed a model to account for the varying configuration of the Sun's magnetic field and for the explaining a number of solar phenomena that are dependent on the field. The most crucial of the observations to be accounted for are taken to be (1) the reversal of the main dipolar field, (2) Spörer's law of sunspot latitudes, (3) Hale's laws governing the magnetic polarity of sunspots, and (4) the fact that bipolar magnetic regions disappear by expanding (Babcock, 1961). The tilt of sunspot pairs away from the east-west direction, as represented by Joy's law, in effect generates a North-South (poloidal) component from an initial east-west (toroidal) magnetic field. An equivalent viewpoint is that the twist imparted by the Coriolis force on the rising flux ropes inducing a mean poloidal field. Dynamo models relying on this poloidal field regeneration mechanism are labelled as "Babcock-Leighton dynamos". In Section 2 the Babcock-Leighton dynamo is presented in detail.

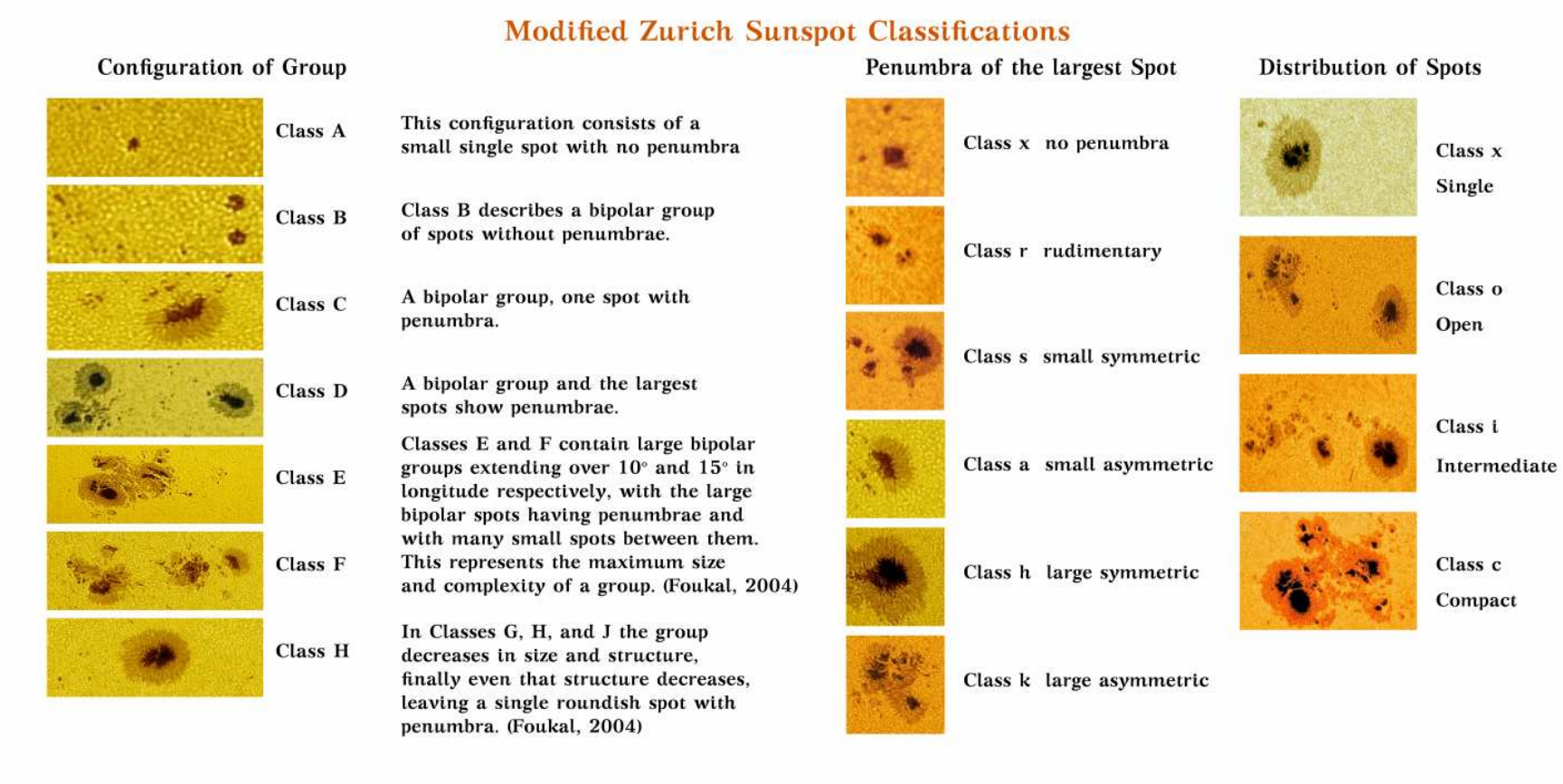

Figure 2: *The magnetic classification of sunspots based on the Zürich/McIntosh system. Using the McIntosh Sunspot Classification Scheme (McIntosh, 1990) spots are classified according to three descriptive codes. The first code is a modification of the old Zurich scheme. The second code describes the penumbra of the largest spot of the group and the third code describes the compactness of the spots in the intermediate part of the group.*

1.2.2. Magnetic Field of Spot Groups

In the convection zone large and small-scale magnetic fields are generated. Active regions on the solar surface are generally thought to originate from a strong toroidal magnetic field generated by a deep-seated solar dynamo mechanism operating at the base of the solar convection zone. Thus the magnetic fields need to traverse the entire convection zone before they reach the photosphere to form the observed solar active regions. Understanding this process of active region flux emergence is therefore a crucial component for the study of the solar cycle dynamo (Yuhong, 2009).

The magnetic field permeates sunspots; it is responsible for the coolness and darkness of sunspots by greatly reducing the convective transport of heat from below. The Sun's average field is very low, $1-2\,\mathrm{G}$. The peak magnetic field of the sunspot umbra is $3000-4000\,\mathrm{G}$ $(0.3-0.4\,\mathrm{T})$ and the field of the penumbra reaches the values of $700-1000\,\mathrm{G}$ $(0.07-0.1\,\mathrm{T})$ at the edge of the visible sunspot. Usually, the darkest part of the umbra associated with the strongest field and it is generally close to vertical, while at the penumbra it is inclined by $70-80$ degree to the vertical.

The most widely accepted explanation of the sunspot's coolness and of the fate of the missing energy is the inhibition of the convection by the magnetic field. (Biermann, 1941) suggested that the magnetic field suspends the convection completely in the first few thousand kilometers of the convection zone. Cowling's (1934) suggestion was that the magnetic field inhibits the convective heat transport partially inside the sunspots, but that it is less powerful than outside. Convective flows are inhibited if the magnetic field energy density $\mathrm{B}^2/8\pi$ is much larger than the kinetic energy density $\rho\nu^2/2$ of the convection, assuming that the effect of the magnetic freeze is working and the magnetic Reynolds number is large enough ($\mathrm{R_m} \gg 1$). The intensity of the umbral field is $3000-4000\,\mathrm{G}$, which is more than enough to the convective motions at the photosphere. In this explanation of spot coolness, an equilibrium would be reached in which the convective heat flux blocked below the spot would simply flow around it. (Foukal, 2004)

The structure of the sunspot is determined by the interaction of the magnetic field with the convection movements in the upper part of the convection zone. (Thomas et al., 2002) suggested a remarkable interlocking-comb structure to the penumbral magnetic field. The penumbral field lines dive down below the photosphere at the edge of the penumbra, but they rise up to the surface quickly by the magnetic buoyancy and they dive again.

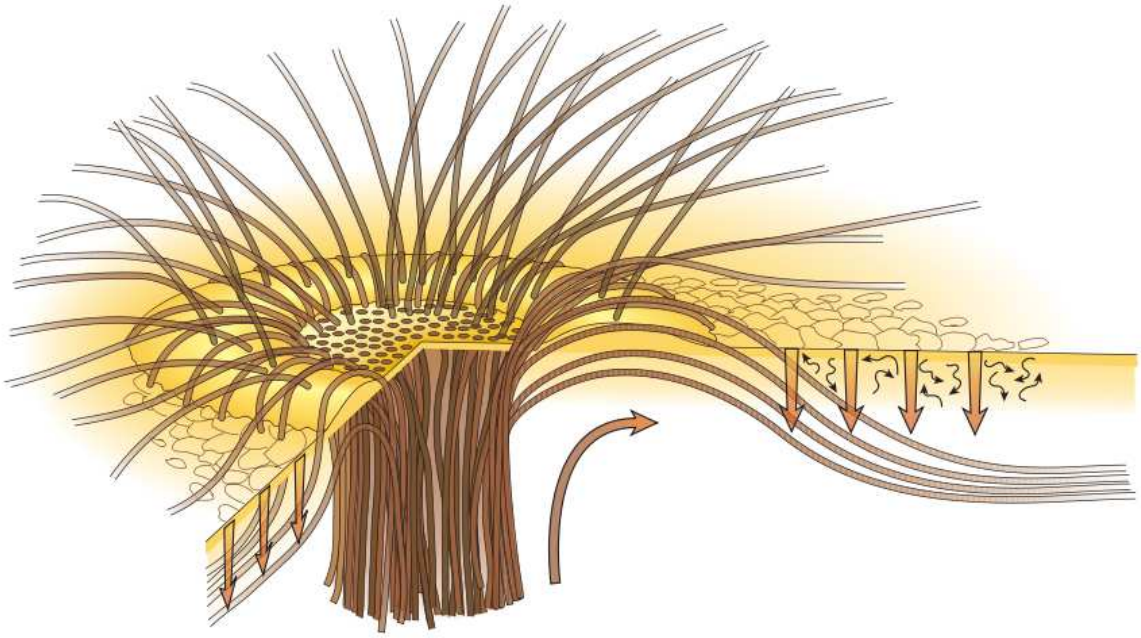

Figure 3: *Sketch showing the interlocking-comb structure of the magnetic field in the filamentary penumbra of a sunspot. The bright radial filaments, where the magnetic field is inclined (at about 40° to the horizontal in the outer penumbra), alternate with dark filaments in which the field is nearly horizontal. Within the dark filaments, some magnetic flux tubes (that is, bundles of magnetic field lines) extend radially outward beyond the penumbra along an elevated magnetic canopy while other, returning flux tubes dive back below the surface. The sunspot is surrounded by a layer of small-scale granular convection (thin squiggly black arrows) embedded in the radial outflow (thick curved brown arrow) associated with a long-lived annular supergranule (the moat cell). The submerged parts of the returning flux tubes are held down by turbulent pumping (indicated by thick vertical brown arrows) due to granular convection in the moat. There is also a persistent horizontal outflow in the penumbra (the Evershed flow), which is mostly confined to thin, nearly horizontal, radial channels within the dark filaments.*

(Source: Thomas et al., 2002)

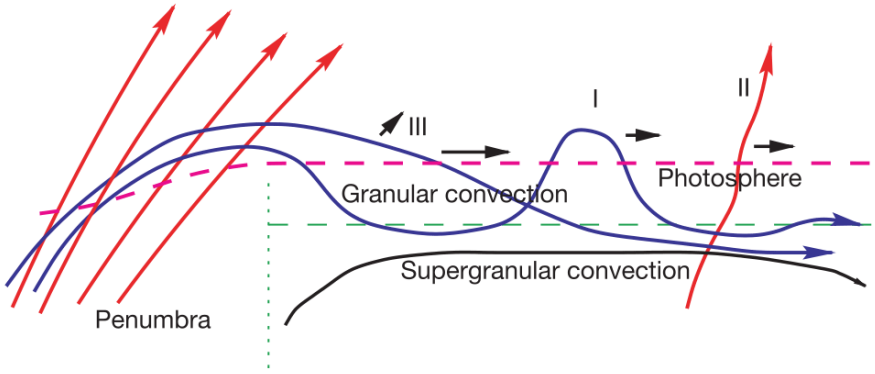

Figure 4: *Moving magnetic features (MMFs) in the moat around a sunspot. Representative magnetic field lines of both the inclined magnetic field (red) in the bright filaments and the nearly horizontal magnetic field (blue) in the dark filaments are displayed. The sketch shows the configuration of MMFs of three types (I, II, III), interpreted in terms of magnetic flux pumping by granular convection in the sunspot moat. Type I MMFs are bipolar pairs of magnetic footpoints moving outward together at speeds of* $0.5 - 1\,\mathrm{km/s}$*, with the inner footpoint usually having the same polarity as the spot. Type II MMFs are single footpoints, with the same polarity as the sunspot, moving outward across the moat at speeds similar to that of type I MMFs. Type II MMFs are associated with flux tubes peeling off the sunspot and being transported horizontally outward by convection; they cause a loss of magnetic flux and decay of the sunspot. Type III MMFs are single footpoints with polarity opposite that of the sunspot that move rapidly outward at speeds of* $2 - 3\,\mathrm{km/s}$*.*

(Source: Thomas et al., 2002)

The discovery of starpots, faculae, and magnetic cycles on other stars has brought new observations to bear on the topic of solar activity and opened new possibilities for applying the advances in understanding gained from studying these phenomena on the sun.

1.2.3. The Butterfly Diagram

More than 150 years ago, scientists learned that the number of sunspots varies cyclically, with a period of approximately 11 years. About 110 years ago, Maunder demonstrated that the location of sunspots varies throughout the sunspot cycle (Maunder, 1904). At the start of each cycle, at solar minimum, the sunspots appear at latitudes about 35°

North and South, symmetric about the equator. Sunspots emerge closer and closer to the equator in the course of a cycle, peaking in coverage at about ±15° of latitude. Towards the end of a cycle, sunspots can be seen quite close to the solar equator, around 7° North and South latitude (Spörer's law, Spörer, 1889). Edward Walter Maunder, constructed the first "butterfly diagram", showing the positions of the sunspots for each rotation. This diagram shows that these bands first form at mid-latitudes, widen, and then move toward the equator as each cycle progresses. The sunspot groups are tilted with respect to the equator, the leading spots always are closer to the equator than the following spots. The tilt angle depends on the latitude. (Joy's Law, Hale et al., 1919)

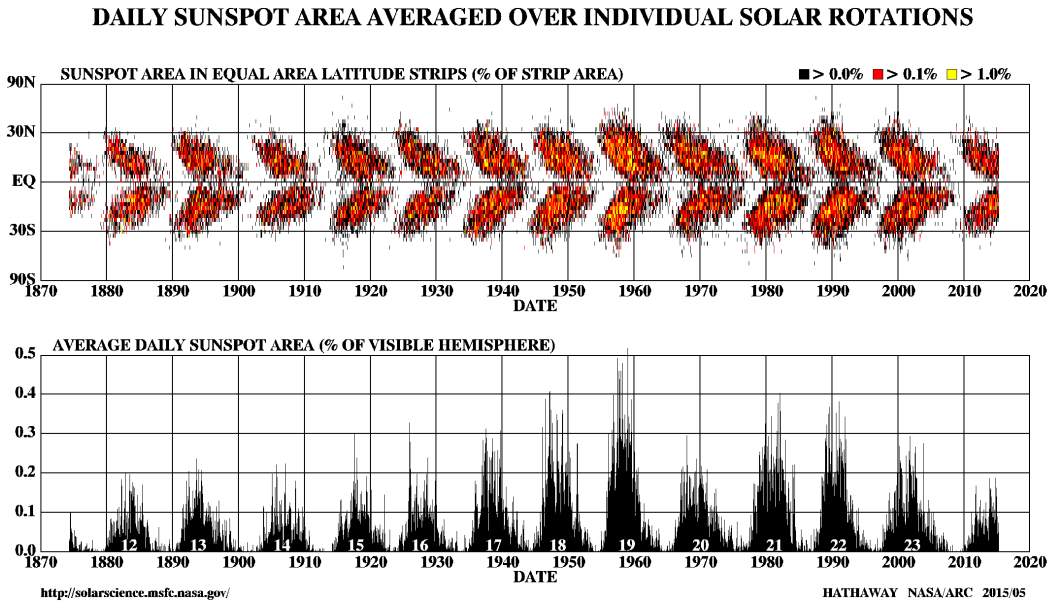

Figure 5: *The cycle of solar activity, shown as the area covered by spots each day, averaged over a month (top) and as the area covered at various latitudes each day, averaged over a month (bottom), from 1875 to 2015. The latitude graph shows the butterfly pattern caused by spots appearing near mid-latitudes at the start of a solar cycle, and closer to the Equator near the end of the cycle.*

(Source: http://solarscience.msfc.nasa.gov)

Sunspot activity cycles are average about eleven years, the shortest is eight years, the longest is fifteen years. The amplitude is variable, and the stronger cycles are shorter. The modern understanding of the sunspot cycle starts with George Ellery Hale, who observed in 1908 the Zeeman effect in the sunspots using a spectroheliograph and discovered that

sunspots have magnetic fields, reverse every 11 years and the solar magnetic activity cycle is average 22 years, covering two polar reversals of the solar magnetic dipole field. Sunspots come in pairs with opposite magnetic polarity. During a given sunspot cycle, the leading sunspots groups have the same polarity in one hemisphere of the Sun. During the next sunspot cycle, the polarity is changed, the polarity of the leading spots in each hemisphere is opposite from what it was in the previous cycle. (Hale's Polarity Law)

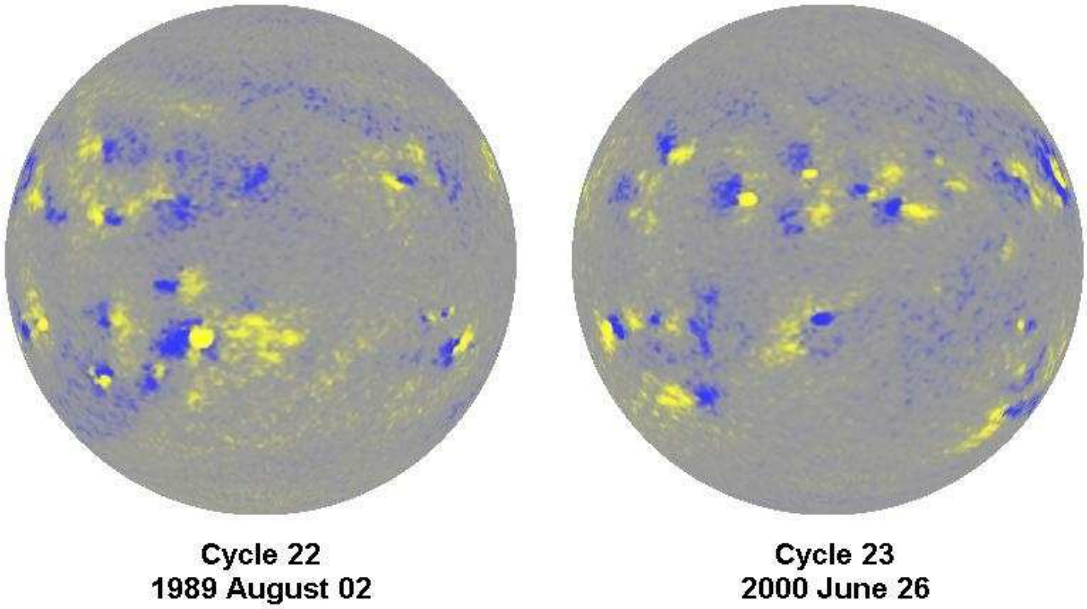

Figure 6: *Hales Polarity Law. Magnetogram from sunspot cycle 22 and 23 are shown. Yellow denote positive polarity and blue is negative polarity. Leading spots in one hemisphere have opposite magnetic polarity to those in the other hemisphere and the polarities reverse from one cycle to the next.*

(Source: Hathaway, 2010)

A number of relationships have been found between various sunspot cycle characteristics. One of the more significant relationships is the Waldmeier Effect. This is an anticorrelation between the peak in sunspot number of a cycle and the time from minimum to reach that peak. Also an empirical rule is the Gnevyshev-Ohl rule, the sum of sunspot numbers over an odd cycle exceeds that of the preceding even cycle.

2. Making a Solar Dynamo Model

2.1. Dynamo Theory

The dynamo converts kinetic energy into magnetic energy. The dynamo theory proposes a mechanism by which a celestial body such as Earth or a star generates magnetic field. The dynamo theory of astrophysical bodies uses magnetohydrodynamic equations to investigate how magnetic field can be regenerated continuously.

Physically, the dynamo produces finite strong magnetic field in a rotating, convecting, and electrically conducting fluid from an arbitrarily low energy field and maintains the magnetic field over long time scales. If the fluid motion is sufficiently complex, the magnetic field can be maintained, the intensification of adjective fluid equilibrates the diffusive decay. The dynamos are called self-sustaining dynamos. The solar dynamo is a self-sustaining dynamo, which converts kinetic energy of the convection and differential rotation within the Sun to magnetic energy.

In the kinematic dynamo theory the velocity field is prescribed, useful studying, how magnetic field strength varies with the flow structure and speed. When the magnetic field is weak that cannot affect the fluid motion by the Lorentz force, the dynamo is called linear. When the magnetic field becomes streng enough to affect the fluid motions, the dynamo is non-linear. Such dynamos are sometimes also referred to as hydromagnetic dynamos. All dynamos in astrophysics are hydromagnetic dynamos.

2.2. The History of Solar Dynamos

Larmor suggested the inductive effect of the fluid motions in 1919, as one of the few possible explanations for the origin of the magnetic field, opening the way to the solar cycle modelling. Some decades later appeared the anti-dynamo theorem, that seriously challenged Larmor's conception. According to the anti-dynamo theorems, the successful dynamos cannot possess a high degree of symmetry. The best known is Cowlings anti-dynamo theorem; an axisymmetric magnetic field cannot be maintained through self-sustaining dynamo action (Cowling, 1934). The theoretical modelling of the solar cycle began with (Parker, 1955), which laid the fundamentals of the α-Ω-dynamo theory. Toroidal field generated from poloidal field by the Ω-effect and the generation of poloidal

field by helical turbulence (α-effect) occurring in the same location inside the convection zone (Parker, 1955). Parker showed that the Coriolis force could originate twists to the rising turbulent fluid elements, breaking the axisymmetry and getting around the Cowlings antidynamo theorem. By the 1970s, mean-field electrodynamics became the fundamental theory for the solar dynamo modelling, including the α-effect of mean-field electrodynamics.

However, serious problems appeared soon, and solar dynamo modelling has not yet recovered from these troubles. First of all, the solar internal differential rotation is known satisfactorily from the helioseismology. The solar-like dynamo solutions of mean-field electrodynamics came from a markedly different differential rotation, namely the radial differential rotation was assumed to be negative inside the main bulk of the convection zone before helioseismology found that the differential rotation is primarily latitudinal in the bulk of the convection zone, and the radial gradient exists in a thin layer, called the tachocline, at/near the base of the convection zone. Furthermore, the radial gradient was found to be positive in the sunspot latitudes (Brown et al., 1989). Thus classical mean-field dynamos will produce poleward migration of the spot-producing toroidal fields. Second, the magnetic fields was not remain in the solar convection zone for sufficient lengths of time to become stong enough to produce the sunspots, because of the buoyancy effects. In addition, numerical simulations showed such a magnetic field migration, which is not observed on the Sun.

Two different approaches were proposed to solve these issues: (i) thin-layer or interface dynamos; (ii) Babcock-Leighton dynamos. The latter includes a new physical mechanism of the alpha-effect for poloidal magnetic field regeneration, namely the generation of poloidal fields at/near the photospheric surface due to the decay of tilted, bipolar active regions. Since the Omega-effect layer was taken to be at/near the base of the convection zone, the two generation layers were spatially separated (Babcock, 1961; Leighton, 1964). If the diffusion connects these two layers, the butterfly diagram will again reveal poleward migration, because the Babcock-Leighton alpha-effect is positive by virtue of its origin. Incorporating meridional circulation with poleward surface flow and an equatorward subsurface return flow and representing this circulation into the induction equations for dynamo action, the Babcock-Leighton dynamos were simulated the butterfly diagram with a new α-effect successfully. The Babcock-Leighton dynamos are the best example of flux transport dynamos undisputedly. Over the past two decades Babcock-Leighton type solar dynamo models have been successful in reproducing many solar cycle features

including equatorward migration of sunspot belts, poleward drift of poloidal fields and correct phase relationship between them (Wang et al. 1991; Choudhuri & et al. 1995; Durney 1995; Dikpati & Charbonneau 1999; Guerrero & Munoz 2004; Jouve et al 2008).

2.3. The Basic Equations of Solar MHD and Mean-Field Electrodynamics

2.3.1. The Solar Magnetohydrodynamics

This section will not discuss in every detail the stellar magnetohydrodynamics. I give a brief overview of the basic equations of magnetohydrodynamics. For a overview the solar magnetohydrodynamics, I suggest reading the (Priest, 2014).

For astrophysical plasma, we suppose the following conditions: (1) the collisional mean-free path of microscopic constituents is much shorter than competing plasma length scales, in this case, so the fluid motions are non-relativistic and the displacement current is negligible; (2) there are not current sources in the plasma; (3) the charge density is zero, the plasma is quasineutral; and (4) in the equations are prescribed the $\epsilon = \epsilon_0 = 1$ permittivity and $\mu = \mu_0 = 1$ magnetic permeability of free space.

The Maxwell equations describe how electric and magnetic fields are generated and altered by each other and by charges and currents. The four Maxwell equations in cgs units,

$$\nabla \times \mathbf{B} = \frac{4\pi}{c}\mathbf{j}, \tag{1a}$$

$$\nabla \times \mathbf{E} = -\frac{1}{c}\frac{\partial \mathbf{B}}{\partial t}, \tag{1b}$$

$$\nabla \mathbf{B} = 0, \tag{1c}$$

$$\nabla \mathbf{E} = 0. \tag{1d}$$

In these equations, $\mathbf{B}$ is the magnetic induction (units: $1\,\mathrm{T} = 10^4\,\mathrm{G}$), $\mathbf{E}$ is the electric field, $\mathbf{j}$ the current density, the speed of light in a vacuum is $\mathrm{c} = (\mu_0\epsilon_0)^{-1/2} = 2.998 \cdot 10^{10}\,\mathrm{cms}^{-1}$.

If an external **B**-field is present and the plasma is moving at a non-relativistic velocity **v** then the current induced by the Lorentz force on the charge carriers appears. Ohm's law states that the current density is proportional to the total electric field

$$\mathbf{j} = \sigma(\mathbf{E} + \mathbf{v} \times \mathbf{B}). \tag{2}$$

Maxwells equations (1a-d) can then be combined using the Ohm's law into a single evolution equation

$$\frac{\partial \mathbf{B}}{\partial t} = \nabla \times (\mathbf{v} \times \mathbf{B}) - \eta \nabla^2 \mathbf{B}. \tag{3}$$

The evolution of magnetic field described by the induction equation including the presence of the velocity in (3). The plasma motion is, in turn, governed by equations of continuity, motion and energy. The equation of mass conservation may be written

$$\frac{\partial \rho}{\partial t} + \nabla(\rho \mathbf{v}) = 0, \tag{4}$$

where ρ is the mass density.

The equation of motion, the Navier-Stokes equation with the Lorentz force may be written

$$\rho \left(\frac{\partial \mathbf{v}}{\partial t} + (\mathbf{v}\nabla)\,\mathbf{v} + 2\boldsymbol{\Omega} \times \mathbf{v} \right) = -\nabla p + \mathbf{j} \times \mathbf{B} - \nabla \mathcal{V} + \nabla \tau, \tag{5}$$

where the plasma pressure gradient ∇p, the gravitational potential gradient $\nabla\mathcal{V}$, $\nabla\tau$ is the viscosity term and the Lorentz force per unit volume is $\mathbf{j} \times \mathbf{B}$ and Coriolis force term is $2\boldsymbol{\Omega} \times \mathbf{v}$.

The Lorentz force is directed across the magnetic field and any motion or density variation along field lines must be produced by gravity or pressure gradients

$$\mathbf{j} \times \mathbf{B} = \frac{(\nabla \times \mathbf{B}) \times \mathbf{B}}{\mu} = \frac{(\mathbf{B}\nabla)\mathbf{B}}{\mu} - \nabla \left(\frac{B^2}{2\mu} \right). \tag{6}$$

The first term on the right-hand side is the magnetic tension force, which is non-zero if **B** varies along the direction of **B** and may be regarded as being produced by the effect of a tension along B of magnitude B^2/μ per unit area. The second term represents a magnetic pressure force due to a scalar magnetic pressure of magnitude B^2/μ per unit area, the same in all directions. The Lorentz force therefore has two effects. It acts both to shorten magnetic field lines through the tension force and also to compress plasma through the magnetic pressure force. The tension produces a resultant force (normal to

B) when the field is curved, while the magnetic pressure gives a resultant effect when the magnitude of **B** is changing in a direction normal to **B** (Priest, 2014).

The energy equation states the rate of increase of heat for a unit volume. The heat equation may be written

$$\rho\frac{dU}{dt} + p\nabla v = \frac{\eta_m}{4\pi}|\nabla \times B|^2 - \nabla(\mathcal{F} + \mathcal{F}_r) - \mathcal{S}_H, \tag{7}$$

where U the internal energy. The right side describes the rate of energy loss. $(\eta_\mathrm{m}/4\pi)|\nabla \times \mathrm{B}|^2$ is the Ohmic dissipation, the $\nabla(\mathcal{F} + \mathcal{F}_\mathrm{r})$ is the heat flux, and $\mathcal{S}_H$ represents the sum of all the other heating sources. The heating term is $\mathcal{S}_\mathrm{H} = \rho\epsilon + \phi_\nu$, where ϵ is the nuclear energy generation rate (per unit mass) in the interior and ϕ_ν is the viscous dissipation rate. The magnetic diffusivity is

$$\eta_m = \frac{c^2}{4\pi\sigma_e}. \tag{8}$$

2.3.1.1. Dimensionless Parameters

The magnetic Reynolds number is a measure of strength of the coupling between flow and magnetic field and indicates the dynamic behaviour of a plasma. It gives an estimate of the effects of magnetic advection to magnetic diffusion

$$R_m = \frac{l_0 v_0}{\eta}, \tag{9}$$

where $\mathrm{v_0}$ is the plasma speed and $\mathrm{l_0}$ is the length-scale. If $\mathrm{R_m} \ll 1$, the η magnetic diffusivity strong, the magnetic field will diffuse away. If $\mathrm{R_m} \gg 1$, Alfvé's theorem states that the magnetic field lines tend to remain frozen into the plasma, so that magnetic field behaves as if it moves with the plasma.

The plasma beta is the plasma pressure ($\mathrm{p_0}$) divided by the magnetic pressure ($\mathrm{p_{mag}} = \mathrm{B_0^2}/2\eta$)

$$\beta = \frac{2\eta p_0}{B_0^2}. \tag{10}$$

The Rossby number is the ratio of inertial to Coriolis terms in the equation of motion. A small Rossby number signifies strong Coriolis forces and a large Rossby number signifies that the inertial and centrifugal forces dominate

$$R_0 = \frac{v_0}{l_0\Omega}. \tag{11}$$

The magnetic Prandtl number compares the viscous and magnetic diffusion

$$P_m = \frac{R_m}{R_e} = \frac{\nu}{\eta}. \tag{12}$$

The Ekman number is the ratio of the viscous force to the Coriolis force

$$E_k = \frac{R_0}{R_e} = \frac{\nu}{(l_0^2\Omega)}. \tag{13}$$

The Taylor number measures the strength of the rotation

$$T = E^{-2}. \tag{14}$$

2.3.2. Mean-field electrodynamics

The theoretical modeling of solar cycle began with (Parker, 1955), laid down the basis of solar $\alpha - \Omega$ dynamo theory. Mean-field electrodynamics has evolved in the 1960s. The evolution of the magnetic field described by the induction equation (3). The mean-field electrodynamics expresses the velocity $\mathbf{v}$ and the field $\mathbf{B}$ as sums of slowly varying mean parts and fluctuating parts

$$\mathbf{B} = \langle \mathbf{B} \rangle + \mathbf{b}', \tag{15a}$$

$$\mathbf{v} = \langle \mathbf{u} \rangle + \mathbf{v}'. \tag{15b}$$

The induction equation is divided $\langle \mathbf{B} \rangle$ mean part and the $\mathbf{b}'$ fluctuating part

$$\frac{\partial}{\partial \mathrm{t}} \langle \mathbf{B} \rangle = \nabla \times (\langle \mathbf{u} \rangle \times \langle \mathbf{B} \rangle + \varepsilon) - \nabla \times (\eta \nabla \times \langle \mathbf{B} \rangle), \tag{16}$$

$$\frac{\partial}{\partial \mathrm{t}} \langle \mathbf{b}' \rangle = \nabla \times (\langle \mathbf{u} \rangle \times \langle \mathbf{b}' \rangle + \mathbf{v}' \times \langle \mathbf{B} \rangle + \mathrm{G}) - \nabla \times (\eta \nabla \times \langle \mathbf{b}' \rangle), \tag{17}$$

where $\varepsilon = \langle \mathbf{v}' \times \mathbf{b}' \rangle$ the turbulent electromotive force, $\mathrm{G} = \mathbf{v}' \times \mathbf{b}' - \langle \mathbf{v}' \times \mathbf{b}' \rangle$. The correlation time and length of turbulent motion are τ and λ, t_0 and l_0 are the scale time and length of variation of $\langle \mathbf{u} \rangle$ and $\langle \mathbf{B} \rangle$. If $\lambda \ll \mathrm{l}_0$, and the turbulence is homogeneous and isotropic, then ε can be expanded according to the derivatives of $\mathbf{B}$ into a series

$$\varepsilon = \alpha \langle \mathbf{B} \rangle - \beta (\nabla \times \langle \mathbf{B} \rangle). \tag{18}$$

Substitution into the induction equation yields

$$\frac{\partial}{\partial \mathrm{t}} \langle \mathbf{B} \rangle = \underbrace{\nabla \times (\langle \mathbf{u} \rangle \times \langle \mathbf{B} \rangle)}_{\text{advective term}} + \nabla \times \alpha \langle \mathbf{B} \rangle - \underbrace{\nabla \times [(\beta + \eta)(\nabla \times \langle \mathbf{B} \rangle)]}_{\text{turbulent term}}. \tag{19}$$

The parameter α is called the kinetic helicity. The parameter β is the turbulent magnetic diffusivity, which comes from random movement of macroscopic turbulent elements. If the turbulence is isotropic,

$$\alpha = -\frac{1}{3}\tau \mathbf{v}' \nabla \times \mathbf{v}', \tag{20a}$$

$$\beta = \frac{1}{3}\tau \mathbf{v}'^{\mathbf{2}}. \tag{20b}$$

Working in spherical coordinates r, θ and ϕ and assuming

$$\mathbf{U} = r \sin\theta \Omega \mathbf{e}_\phi, \tag{21}$$

the magnetic field can be expressed, the sum the toroidal and poloidal component

$$\mathbf{B}(\mathbf{r}, \theta, \mathbf{t}) = \mathbf{B_t} + \mathbf{B_p} = \nabla \times (A\mathbf{e_r}) + \nabla \times (\nabla \times A\mathbf{e_r}) = \nabla \times (A\mathbf{e_r}) + \nabla \times (A\mathbf{e}_\phi). \tag{22}$$

The poloidal component of the mean-field induction equation is

$$\frac{\partial A}{\partial t} = \alpha \mathbf{B} + \beta \left(\nabla^2 - \frac{1}{r \sin\theta} \right) A. \tag{23}$$

The toroidal component of the mean-field induction equation is

$$\frac{\partial B}{\partial t} = \left[\hat{\Omega} \times (\nabla A) \right]_\phi - \alpha \nabla^2 A + \beta \nabla^2 B, \tag{24}$$

where the shear vector is

$$\hat{\Omega} = r \sin\theta \nabla \Omega. \tag{25}$$

Equations (23) and (24) are the classical dynamo equations.

2.4. The Solar Dynamo Problem

The cycle of solar activity is maintained by the dynamo process. In the solar dynamo problem context, the circumstances and flow fields have to be identified which can sustain the cyclic regeneration of the magnetic field. A model of the solar dynamo should reproduce the observed features of the solar cycles.

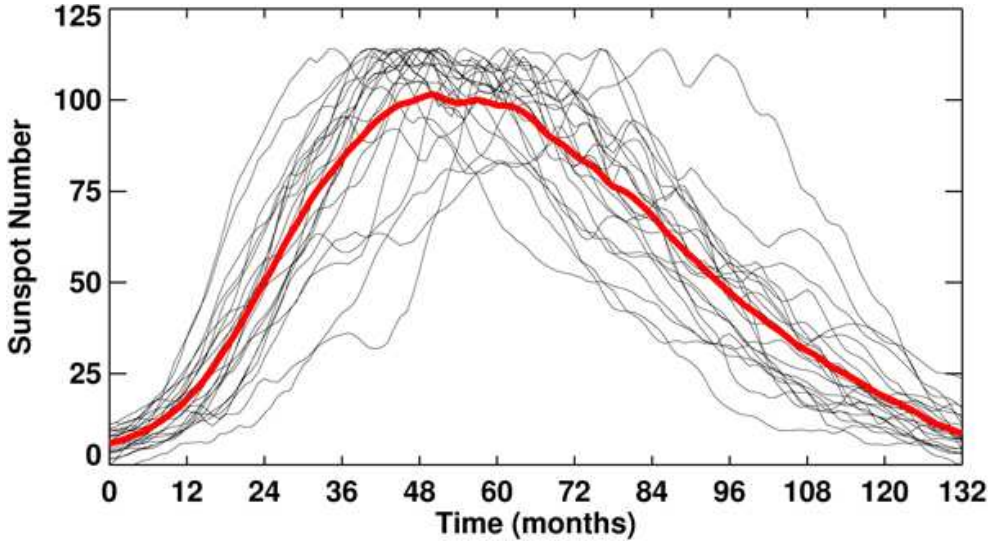

Figure 7: *The average of cycles 1 to 23 (thick red line) normalized to the average amplitude and period. The average cycle is asymmetric in time with a rise to maximum over 4 years and a fall back to minimum over 7 years. The 23 individual, normalized cycles are shown with thin black lines.*

(Source: Hathaway, 2015)

Sunspots are caused by very strong, $1-2\,\mathrm{kG}$ magnetic fields on the Sun. The sunspot pairs have opposite polarity in one hemisphere in one solar cycle. Since the field reverses from one activity cycle to the next, the magnetic cycle actually has a 22-year period, the magnetic period. The solar dynamo models have to reproduce the equatorward migration, polarity reversals and the strength of the the sunspot-generating toroidal field.

The poloidal surface field migrates poleward on photospheric magnetograms and a substantial phase lag has been observed between the poloidal and the toroidal fields. At sunspot cycle maximum, the toroidal field peaks, while the poloidal field flips over into the opposite polarity. The dynamo problem includes two sub-problems: the toroidal field is generated from poloidal fields by the Ω-effect and poloidal fields regenerated by helical

turbulence (α-effect).

A solar dynamo model should also be able to reproduce the many empirical correlations found in the sunspot record. The more significant and studied connection is the anti-correlation between rising time and amplitude, the Waldmeier Effect (Waldmeier, 1935; Waldmeier, 1939), namely the rise time for the sunspot number from minimum to maximum is inversely proportional to the cycle amplitude. (Dikpati et al., 2008) showed the Waldmeier Effect in Wolf sunspot number data, but is not present in another solar cycle index, namely sunspot area data. This is true for the spot area data both when summed over northern and southern hemispheres, and when the two hemispheres are considered separately.

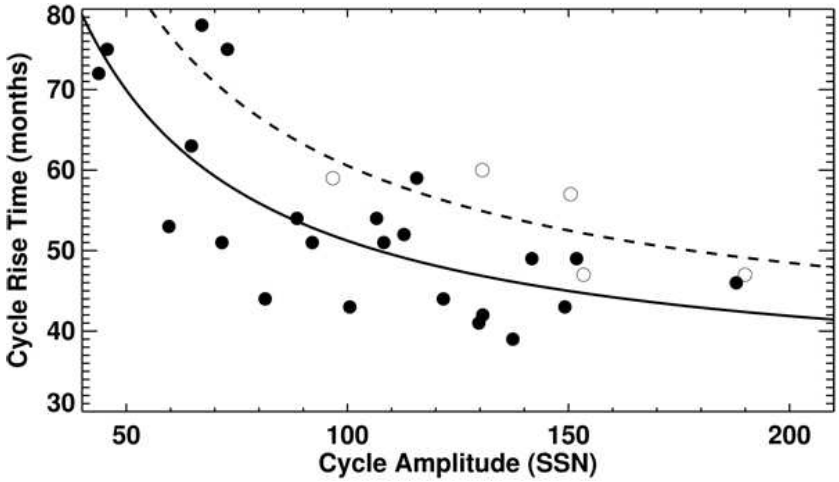

Figure 8: *The Waldmeier Effect. The cycle rise time (from minimum to maximum) plotted versus cycle amplitude for International Sunspot Number data from cycles 1 to 23 (filled dots) and for 10.7 cm radio flux data from cycles 19 to 23 (open circles). This gives an inverse relationship between amplitude and rise time shown by the solid line for the Sunspot Number data and with the dashed line for the radio flux data.*

(Source: Hathaway, 2015)

(Gnevyshev & Ohl, 1948) found that if solar cycles are arranged in pairs with an even numbered cycle and the following odd numbered cycle then the sum of the sunspot numbers in the odd cycle is higher than in the even cycle. This is referred to as the Gnevyshev-Ohl Rule or Even-Odd Effect. In about 1645 and continuing to about 1715, sunspots became drastically rare, as noted by solar observers of the time. Many historical Grand minima are known, including Maunder Minimum, Spórer Minimum or Dalton Minimum. One

should finally add to the list torsional oscillations in the convective envelope, with proper amplitude and phasing with respect to the magnetic cycle. This is a very tall order by any standard, (Charbonneau, 2010).

Individual solar cycles are characterized by their maxima and minima, cycle periods and amplitudes, cycle shape, the equatorward drift of the active latitudes, hemispheric asymmetries, and active longitudes.

There exists much observational evidence that solar cycle peak amplitude, timing and shape exhibit differences between northern and southern hemispheres.

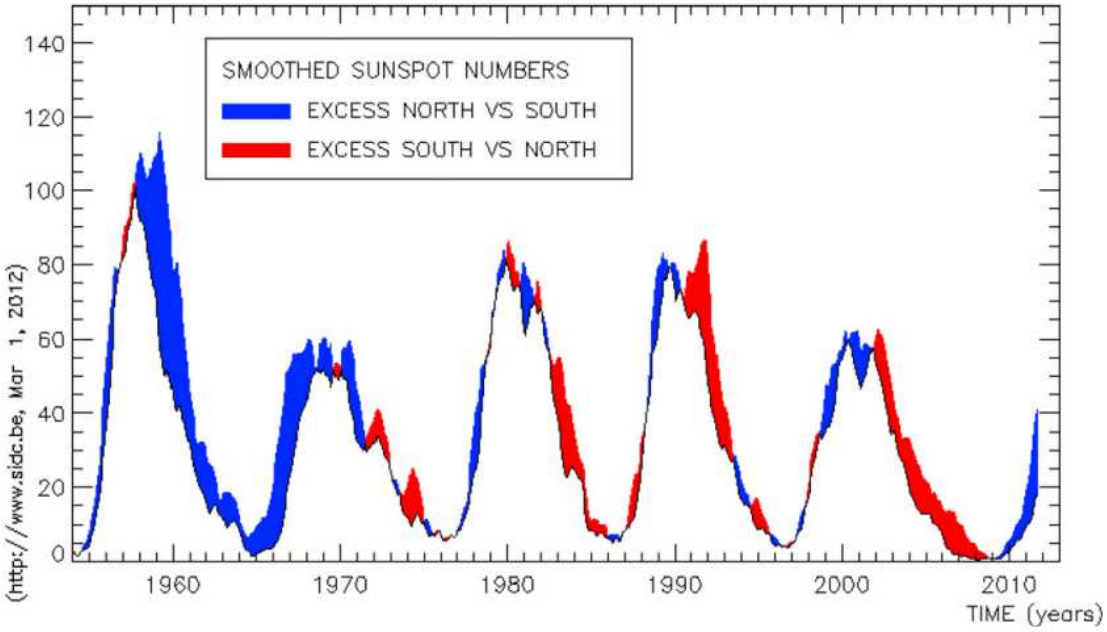

Figure 9: *Blue represents excess solar activity in the North with respect to the South, and red represents the opposite, i.e., the excess South vs. North.*

(Source: Beluczz & Dikpati, 2013)

Figure 9, taken from Royal Observatory of Belgium, shows that the solar cycle amplitude was dominated by the activity in the northern hemisphere of the Sun during both the rising and declining phases of cycle 19. For cycles 20-24, the northern hemisphere's activity dominated the cycle amplitude, while the southern hemisphere's activity dominated during the declining phase, (Beluczz & Dikpati, 2013). Statistical analyses of the differences in solar cycle properties of the North and South hemispheres have been carried out for many years by using many methods and several kinds of solar cycle data,

most commonly sunspot numbers and areas but also flares, proton events, active prominences, solar wind velocity, interplanetary magnetic fields, geomagnetic activity indices, and galactic cosmic rays (Verma, 2000; Vernova et al., 2002; Li et al., 2002; Javaraiah, 2007; Nair & Nayar, 2008; Bankoti et al., 2010; Chowdhury et. al., 2013a; Chowdhury et. al., 2013b).

2.5. The Babcock-Leighton Flux-transport Dynamo Model

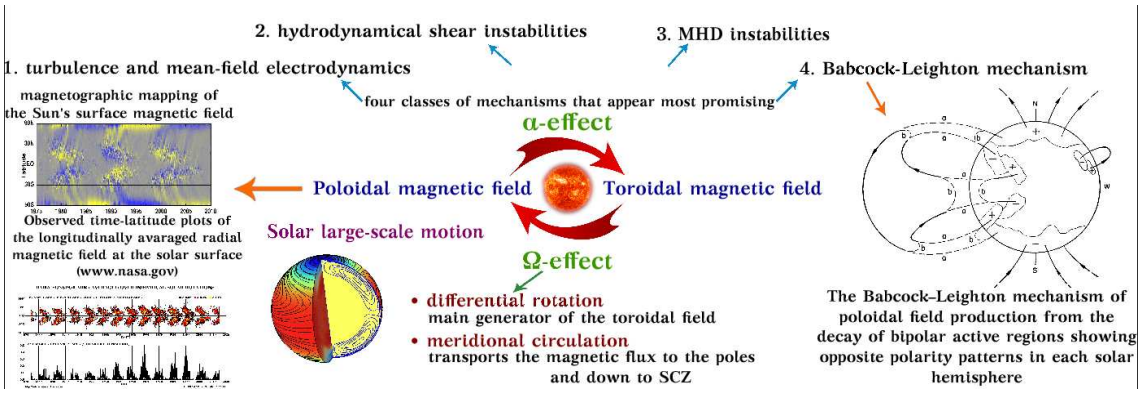

Figure 10: Schematic of α-Ω dynamo models.

The α-Ω dynamos with meridional circulation are so-called flux-transport dynamos, widely used variety of hydromagnetic dynamo models for the Sun. Observations suggest that production of large-scale magnetic field works as a two-step process. The generation of the strong toroidal (azimuthally-directed) magnetic component is produced when the poloidal component is stretched out and wound around by the Sun's differential rotation (Ω-effect). This is now widely accepted to occur deep in the solar convection zone, at or immediately beneath the tachocline. In the tachocline, the rotation rate changes very rapidly. The form and magnitude of the differential rotation at the core-envelope interface is known from helioseismology (Zhao et al., 2009; Corbard et al., 2001). The production of the poloidal component is generated with reversed polarity by the twisting of toroidal flux tubes by helical motions (α-effect). This process is more uncertain. The solar dynamo models can be classificated, (i) which mechanism is used as α-effect, (ii) are the α-effect and Ω-effect separated or undivided in space, and (iii) the butterfly diagram is explained

as dynamo wave or some flux-transport mechanism. Meridional circulation serves as a conveyor belt, transporting the poloidal component from the surface to the interior of convection zone, and the toroidal component to the lower latitudes at the core-envelope interface. In these models, this ingredient also plays an important role in determining the dynamo cycle period and in governing the memory of the Sun's past magnetic fields (Dikpati et al., 2006; Dikpati & Gilman, 2008). Although it has been detected by different observations (Hathaway et al., 1996; Braun & Fan, 1998), that the meridional circulation is poleward in the solar near-surface layers with flow speed of $10 - 20\,\mathrm{ms}^{-1}$, the equatorward return branch of the meridional circulation in the deep convection zone has not been observed. The poleward meridional circulation in the upper half of the convection zone down to about $0.85\,\mathrm{R}$ has been indicated by the helioseismology. Using time-distance helioseismology the most recent observations from SDO/HMI data infer meridional circulation with two cells in depth (Zhao et al., 2013). Ring-diagram analysis from GONG data infer that the surface flow is poleward up to about $\sim 60^\circ$ latitude (Haber et al., 2013; Basu & Antia, 2010; Komm et al., 2012), whereas Doppler measurements from Mount Wilson Observatory data, which can measure this flow at higher latitudes, infer a high-latitude, reverse flow associated with the primary poleward surface flow (Ulrich, 2010). Using a very long-term GONG database and applying time-distance technique (Kholikov et al., 2014) have found signatures of equatorward return-flow in the lower half of the convection zone, indicating a long, deep one-cell flow-pattern. A p-mode perturbation analysis by (Schad et al., 2013) infers four cells in latitude, each going down to about 0.8R. Thus observations do not yet give us a unique answer about the Sun's meridional circulation pattern. (Belucz et al., 2015)

(Babcock, 1961) proposed and (Leighton, 1964) elaborated that weak, diffuse fields drift poleward and produce poloidal fields at the surface from the observed decay of tilted, bipolar active regions. The tilt of sunspot pairs away from the east-west direction, as represented by Joy's law, generates a North-South (poloidal) component from an initial east-west (toroidal) magnetic field. An equivalent viewpoint is that the twist imparted by the Coriolis force on the rising flux ropes induces a mean poloidal field. Dynamo models relying on this poloidal field regeneration mechanism are called as "Babcock-Leighton dynamos". This process is actually observed, so in what follows the focus is placed on dynamo models relying on this poloidal field regeneration mechanism, because they are arguably the best exemples of flux transport dynamos (Charbonneau, 2007). Figure (11) shows the schematic of solar flux-transport dynamo processes.

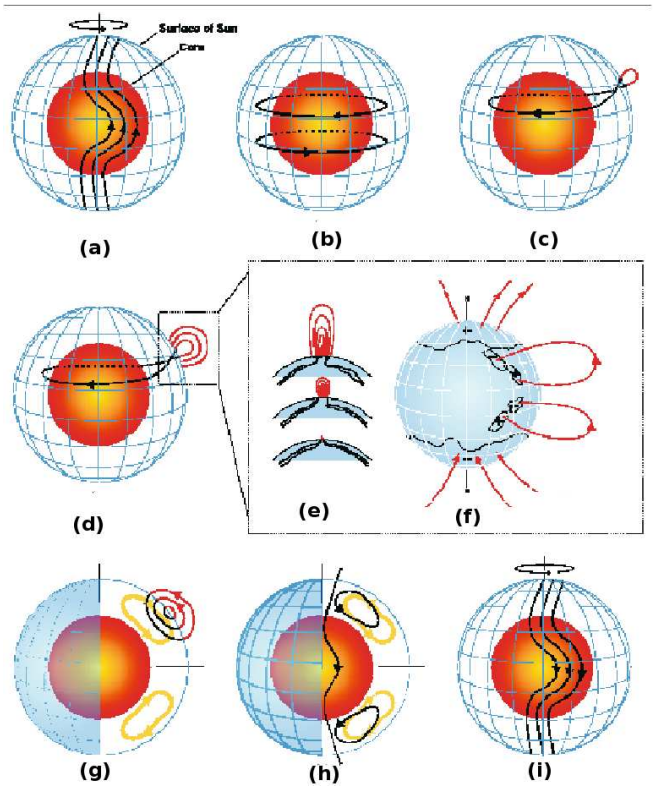

Figure 11: Schematic of solar flux-transport dynamo processes. *Red inner sphere represents the Sun's radiative core and blue mesh the solar surface. Between them is the solar convection zone where dynamo resides. (a) Shearing of poloidal field by the Suns differential rotation near the bottom of convection zone. The Sun rotates faster at the equator than the pole. (b) Toroidal field produced due to this shearing by differential rotation. (c) When toroidal field is strong enough, buoyant loops rise to the surface, twisting as they rise due to rotational influence. Sunspots (two black dots) are formed from these loops. (d, e, f) Additional flux emerges (d, e) and spreads (f) in latitude and longitude from decaying spots. (g) Meridional flow (yellow circulation with arrows) carries surface magnetic flux poleward, causing polar fields to reverse. (h) Some of this flux is then transported downward to the bottom and towards the equator. These poloidal fields have sign opposite to those at the beginning of the sequence, in frame (a). (i) This reversed poloidal flux is then sheared again near the bottom by the differential rotation to produce the new toroidal field opposite in sign to that shown in (b).*

Source: Dikpati & Gilman, 2008

Over the past two decades, Babcock-Leighton type solar dynamo models have been successful in reproducing many solar cycle features including equatorward migration of sunspot belts, the spatiotemporal evolution and the poleward drift of poloidal fields, correct phase relationship between the two magnetic field component. They naturally reproduce the observed solar cycle period and some observed patterns of solar cycle amplitude fluctuations, such as the Gnevyshev-Ohl rule (Wang et al., 1991; Choudhuri et. al., 1995; Durney, 1995; Dikpati & Charbonneau, 1999; Küker et al., 2001; Bonanno et al., 2005; Nandy & Choudhuri, 2001; Guerrero & Muñoz, 1995; Jouve & Brun, 2007; Charbonneau et al., 2007). It was possible to calibrate these models (Dikpati et al., 2006) for the Sun and so they were applied to prediction of solar cycle amplitude. Now, we know that solar cycle 24 amplitude forecast, namely a 30% to 50% stronger cycle 24 peak than the peak of cycle 23, has not been validated. One of the reasons is that the assumption of a steady, single-celled meridional circulation in each hemisphere may be oversimplified for the Sun. Both observations and models indicate that there may be more than one cell in either depth or latitude, or both, in each hemisphere, at least some times. In (Belucz et al., 2015), our aim was to study the effects of various plausible multi-cellular meridional flow patterns on a Babcock-Leighton solar dynamo model operating in a full spherical shell of the convection zone (see Section 4.).

Despite the observations supporting the Babcock-Leighton mechanism, much discussion exists on some issues. A detailed summary article about these questions and answers is (Charbonneau, 2010).

2.6. The SOLAR Babcock-Leighton Flux-transport Dynamo Model

We developed a C-language code for our Babcock-Leighton kinematic flux transport solar dynamo model (Belucz et al., 2013; Belucz & Dikpati, 2013; Belucz et al., 2015; SOLAR), this improved an earlier model (Dikpati & Charbonneau, 1999; DC99) in order to examine North-South (N-S) asymmetry. We also examined with this model the role of complex, multi-cellular circulation patterns in a Babcock-Leighton solar dynamo in advection- and diffusion-dominated regimes. The main components of the model are a solar-like internal differential rotation profile, a depth-dependent diffusivity, a tachocline α-effect and Babcock-Leighton type surface poloidal source and two different stream function (Forgács-Dajka & Petrovay, 2002 and Dikpati et al., 2010) to represent the meridional circulation.

2.6.1. Dynamo Equations

We use spherical polar coordinates $(\mathrm{r}, \theta, \phi)$, and assume axisymmetry. The magnetic field, as the sum of a toroidal component ($\mathbf{B}_\phi$) and a poloidal component ($\mathbf{B_p}$), can be written as:

$$\mathbf{B}(\mathrm{r}, \theta, \mathrm{t}) = \mathbf{B}_\phi(\mathrm{r}, \theta, \mathrm{t})\boldsymbol{e}_\phi + \boldsymbol{\nabla} \times [\mathrm{A}(\mathrm{r}, \theta, \mathrm{t})\boldsymbol{e}_\phi], \tag{26}$$

where the toroidal component of the magnetic field $\mathbf{B}_\phi(\mathrm{r}, \theta, \mathrm{t})$ and the vector potential $\mathrm{A}(\mathrm{r}, \theta, \mathrm{t})\mathbf{e}_\phi$. Both components can be generated by a flow. The large-scale flow field $\mathbf{U}(\mathrm{r}, \theta)$ be expressed as the sum of differential rotation ($\Omega(\mathrm{r}, \theta)$) and the meridional circulation ($\mathbf{u}(\mathrm{r}, \theta) = u_r(r, \theta)\mathbf{e_r} + u_\theta(r, \theta)\mathbf{e}_\theta$):

$$\mathbf{U}(\mathrm{r}, \theta) = \mathbf{u}(\mathrm{r}, \theta) + \mathrm{r}\sin\theta\Omega(\mathrm{r}, \theta)\mathbf{e}_\phi, \tag{27}$$

as toroidal and poloidal parts of the total flow field.

The evolution of the large-scale magnetic field B according to

$$\frac{\partial \mathbf{B}}{\partial \mathrm{t}} = \boldsymbol{\nabla} \times (\mathbf{U} \times \mathbf{B} - \eta \boldsymbol{\nabla} \times \mathbf{B}). \tag{28}$$

The toroidal component becomes

$$\frac{\partial \mathrm{B}_\phi}{\partial \mathrm{t}} = \mathrm{r}\sin\theta(\mathbf{B_p} \cdot \boldsymbol{\nabla})\Omega - \boldsymbol{\nabla}\eta \times \boldsymbol{\nabla} \times \mathrm{B}_\phi \boldsymbol{e}_\phi + \eta\left(\nabla^2 - \frac{1}{\mathrm{r}^2\sin^2\theta}\right)\mathrm{B}_\phi, \tag{29}$$

where $\eta(\mathrm{r})$ is the magnetic diffusivity.

$$\frac{\partial \mathrm{A}}{\partial \mathrm{t}} = \eta \left(\nabla^2 - \frac{1}{\mathrm{r}^2 \sin^2 \theta} \right) \mathrm{A} + \mathrm{S}(\mathrm{r}, \theta; \mathrm{B}_\phi), \tag{30}$$

where $\mathbf{B_p} = \boldsymbol{\nabla} \times (\mathrm{A}\boldsymbol{e}_\phi)$.

Flux-transport dynamo is driven by both a tachocline α-effect and Babcock-Leighton-type surface poloidal source. The decay of the tilted bipolar active regions can produce an amount of poloidal fields near the surface. To produce an antisymmetric toroidal field, the poloidal field needs to be sheared by differential rotation. On the other hand, a poloidal field significantly decay during the transport because it is detached from its source. We use the following expressions for Babcock-Leighton surface source:

$$\mathrm{S}(\mathrm{r}, \theta, \mathrm{B}_\phi) = \{\mathrm{S}_{\mathrm{BL}}(\mathrm{r}, \theta) + \mathrm{S}_{\mathrm{tachocline}}(\mathrm{r}, \theta)\} \left[1 + \left(\frac{\mathrm{B}_\phi(\mathrm{r}, \theta, \mathrm{t})}{\mathrm{B}_0} \right)^2 \right]^{-1} \tag{31a}$$

$$\mathrm{S}_{\mathrm{BL}}(\mathrm{r}, \theta) = \frac{\mathrm{s}_1}{2} \left[1 + \mathrm{erf}\left(\frac{\mathrm{r} - \mathrm{r}_4}{\mathrm{d}_4} \right) \right] \left[1 - \mathrm{erf}\left(\frac{\mathrm{r} - \mathrm{r}_5}{\mathrm{d}_5} \right) \right] \sin\theta \cos\theta \left[\frac{1}{1 + \mathrm{e}^{\gamma_1(\pi/4 - \theta)}} \right] \tag{31b}$$

for $\theta < \pi/2$ and for $\theta > \pi/2$

$$\mathrm{S}_{\mathrm{BL}}(\mathrm{r}, \theta) = \frac{\mathrm{s}_1}{2} \left[1 + \mathrm{erf}\left(\frac{\mathrm{r} - \mathrm{r}_4}{\mathrm{d}_4} \right) \right] \left[1 - \mathrm{erf}\left(\frac{\mathrm{r} - \mathrm{r}_5}{\mathrm{d}_5} \right) \right] \sin\theta \cos\theta \left[\frac{1}{1 + \mathrm{e}^{\gamma_1(\theta - 3\pi/4)}} \right] \tag{31c}$$

$$\mathrm{S}_{\mathrm{tachocline}}(r, \theta) = \frac{\mathrm{s}_2}{4} \sin\left[6 \left(\theta - \frac{\pi}{2} \right) \right] e^{-\beta(\theta - \pi/4)^2} \times \\ \times \frac{1}{e^{\gamma_2(\theta - \pi/3)} + 1} \left[1 + \mathrm{erf}\left(\frac{\mathrm{r} - \mathrm{r}_6}{\mathrm{d}_6} \right) \right] \left[1 - \mathrm{erf}\left(\frac{\mathrm{r} - \mathrm{r}_7}{\mathrm{d}_7} \right) \right] \tag{31d}$$

The parameters used in Equations (31b) and (31c) are following: the amplitudes for the strength of the Babcock-Leighton and tachocline source term $\mathrm{s}_1 = 2.5\,\mathrm{ms}^{-1}$, $\mathrm{s}_2 = 0.5\,\mathrm{ms}^{-1}$, location of the error functions $\mathrm{r}_4 = 0.95\,\mathrm{R}_\odot$, $\mathrm{r}_5 = 0.9875\,\mathrm{R}_\odot$, $\mathrm{r}_6 = 0.70579\,\mathrm{R}_\odot$, $\mathrm{r}_7 = 0.7245696\,\mathrm{R}_\odot$, length scales for the radial variation $\mathrm{d}_4 = \mathrm{d}_5 = \mathrm{d}_6 = \mathrm{d}_7 = 0.0125\,\mathrm{R}_\odot$, deep toridal field strength $\mathrm{B}_0 = 10\,\mathrm{kG}$ and other free parameters $\gamma_1 = 30.0$, $\gamma_2 = 40$, $\beta = 70.0$.

2.6.2. Differential Rotation Profile

The solar internal rotation profile includes primarily latitudinal shear in the convection zone as seen in two-dimensional helioseismic inversions. A solar-like internal differential

rotation profile (Dikpati & Charbonneau, 1999) is given by,

$$\Omega(\mathrm{r},\theta) = \Omega_\mathrm{s} + \frac{1}{2}\left[1 + \mathrm{erf}\left(2\frac{\mathrm{r}-\mathrm{r_c}}{\mathrm{d_1}}\right)\right]\{\Omega_\mathrm{s}(\theta) - \Omega_\mathrm{c}\} \tag{32a}$$

where

$$\Omega_\mathrm{s} = \Omega_\mathrm{Eq} + \mathrm{a_2}\cos^2\theta + \mathrm{a_4}\cos^4\theta \tag{32b}$$

is the surface latitudinal differential rotation. Values were chosen to closely resemblen the best fit helioseismic solution of (Charbonneau et al., 1998). The angular velocity of rigidly rotating core is $\Omega_\mathrm{c}/2\pi = 432.8\,\mathrm{nHz}$. $\Omega_\mathrm{Eq}/2\pi = 460.7\,\mathrm{nHz}$ is the rotation rate at the equator. The other parameters are set as $\mathrm{a_2}/2\pi = 62.69\,\mathrm{nHz}$, and $\mathrm{a_4}/2\pi = 67.13\,\mathrm{nHz}$. The $\mathrm{r_c} = 0.7\,\mathrm{R_\odot}$ indicates the central radius of the $\mathrm{d_1} = 0.0125\,\mathrm{R_\odot}$ thickness tachocline.

The differential rotation is known from helioseismic measurements relatively well for the Sun and there have been indication of a near-surface shear layer. The most frequently used differential rotation prescription is characterized by purely latitudinal differential rotation with equatorial acceleration, smoothly matching on the core rotating. We also use a differential rotation profile, including near-surface shear layer in some cases. The detailed differential rotation pattern follow (Dikpati, 2014)

$$\Omega(r,\theta) = A_1(r,\theta) + \psi_{tac}(r)(\Omega_{cz} - \Omega_c + a_2\cos^2\theta + a_4\cos^4\theta), \tag{33a}$$

$$A_1(r,\theta) = \Omega_c + \psi_{cz}\{\alpha(\theta)(r - r_{cz})\} + \psi_s(r) \times \frac{\Omega_{Eq} - \Omega_{cz} + \beta(\theta)(R - r_s)}{(r_s - r_{cz})}, \tag{33b}$$

$$\beta(\theta) = \beta_0 + \beta_3 cos^3\theta + \beta_6\cos^6\theta, \tag{33c}$$

$$\psi_i = \frac{1}{2}\left[1 + \mathrm{erf}\left(2\frac{r - r_i}{\omega_i}\right)\right], \qquad i = c, cz, s. \tag{33d}$$

Here $\Omega_\mathrm{Eq}/2\pi = 452.5\,\mathrm{nHz}$, $\Omega_\mathrm{c}/2\pi = 435\,\mathrm{nHz}$, $\mathrm{a_2}/2\pi = -61\,\mathrm{nHz}$, $\mathrm{a_4}/2\pi = -73.5\,\mathrm{nHz}$. What the other parameters denote and their values are as follows: the location at which the slope of the rotation contours starts $\mathrm{r_{cz}} = 0.71\,\mathrm{R_\odot}$; the equatorial rotation rate at $\mathrm{r_c z}$, $\Omega_\mathrm{cz}/2\pi = 453.5\,\mathrm{nHz}$, the width, $\omega_\mathrm{cz} = 0.05\,\mathrm{R_\odot}$; the position of the tachocline, $\mathrm{r_c} = 0.69\,\mathrm{R_\odot}$; width of the tachocline, $\omega_\mathrm{c} = 0.05\,\mathrm{R_\odot}$; the position of the maximum of near-surface shear, $\mathrm{r_s} = 0.97\,\mathrm{R_\odot}$; the width, $\omega_\mathrm{s} = 0.05\,\mathrm{R_\odot}$, and the near-surface shear is defined by $\beta_0/2\pi = 437\,\mathrm{nHz}$, $\beta_3/2\pi = -214\,\mathrm{nHz}$ and $\beta_6/2\pi = -503\,\mathrm{nHz}$.

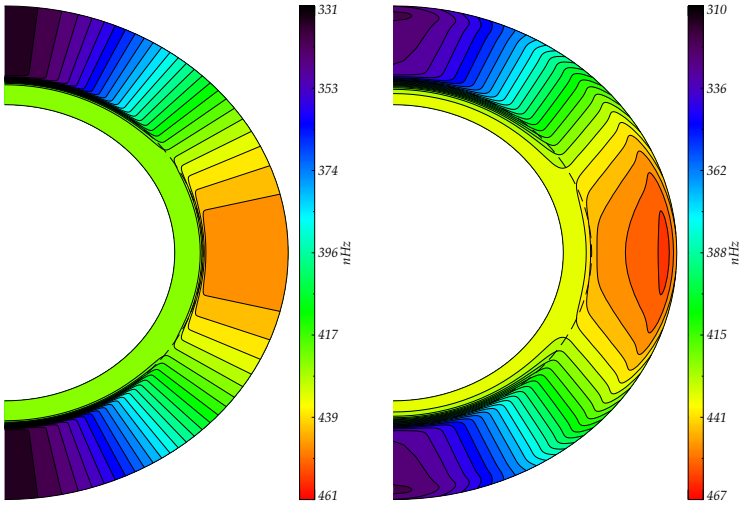

Figure 12: *The differential rotation profiles with and without near-surface shear layer prescribed in* (32a) *and* (33a).

2.6.3. Diffusivity Profile

Direct measurements of magnetic diffusivity as a function of depth are not possible yet. The mixing-length theory gives us an estimate of the supergranular diffusivity within a range ($\eta_{\rm super} = 10^{12} - 10^{14}\,{\rm cm^2 s^{-1}}$) in the supergranulation layer near the surface. The magnetic diffusivity in the envelope is dominated by its turbulent contribution, but below the convection zone there is much less turbulence, the core is stabler, the diffusivity should be determined essentially from the molecular contribution in the stably stratified deep radiative interior (Dikpati et al., 2006). We assume that the turbulence governs the diffusivity in the convection zone and it gets significantly reduced in the subadiabatically stratified radiative zone below (Dikpati et al., 2004). The diffusivity profile can be written as:

$$\eta({\rm r}) = \eta_{\rm core} + \frac{\eta_{\rm T}}{2}\left[1 + {\rm erf}\left(\frac{{\rm r} - {\rm r}_8}{{\rm d}_8}\right)\right] + \frac{\eta_{\rm super}}{2}\left[1 + {\rm erf}\left(\frac{{\rm r} - {\rm r}_9}{{\rm d}_9}\right)\right]. \qquad (34)$$

The parameters in the diffusivity profile: $\eta_{\rm T} = 1.5 \cdot 10^{11}\,{\rm cm^2 s^{-1}}$ is the turbulent diffusivity, $\eta_{\rm core} = 10^9\,{\rm cm^2 s^{-1}}$ is the core diffusivity, $\eta_{\rm super} = 3 \cdot 10^{12}\,{\rm cm^2 s^{-1}}$ is the supergranular diffusivity, locations of the error functions ${\rm r}_8 = 0.7\,{\rm R}_\odot$, ${\rm r}_9 = 0.9562\,{\rm R}_\odot$, length scales for the radial variation ${\rm d}_8 = 0.0125\,{\rm R}_\odot$, ${\rm d}_9 = 0.025\,{\rm R}_\odot$.

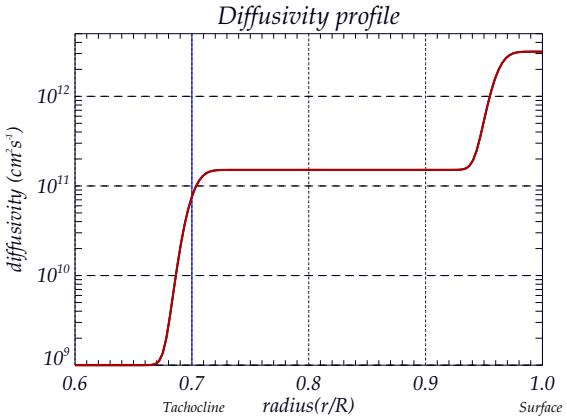

Figure 13: *The diffusivity profile is prescribed in* (34).

2.6.4. Stream Function

The circulation is represented in the spherical shell by a stream function of (Forgács-Dajka & Petrovay, 2002). The steamline flow applies to both of hemispheres. To study the effects of meridional circulation, we prescribe a simple and well-adjustable spatial structure with realistic amplitude. The components of the meridional circulation can be written as

$$\mathbf{u}(\mathrm{r}) = \frac{1}{\rho(\mathrm{r}) \cdot \mathrm{r}^2 \sin\theta} \cdot \frac{\partial}{\partial\theta} \mathbf{\Psi}(\mathrm{r}, \theta), \tag{35a}$$

$$\mathbf{u}(\theta) = \frac{-1}{\rho(\mathrm{r})\mathrm{r} \sin\theta} \cdot \frac{\partial}{\partial\mathrm{r}} \mathbf{\Psi}(\mathrm{r}, \theta). \tag{35b}$$

We represent the stream function in the following form:

$$\mathbf{\Psi}(\mathrm{r}, \theta) = \psi(\mathrm{r}) \sin^2 \mathrm{n}\theta \cos \mathrm{n}\theta, \tag{35c}$$

where the form of the given function $\psi(\mathrm{r})$ specifies the flow.

$$\psi(\mathrm{r}) = \psi_0 \sin\left[\frac{\mathrm{k}\pi\,(\mathrm{r} - \mathrm{r_{mc}})}{\mathrm{R} - \mathrm{r_{mc}}}\right] \exp\left[\frac{(\mathrm{r} - \mathrm{r}_0)^2}{\Gamma^2}\right], \tag{35d}$$

where ψ_0 sets the amplitude of the meridional circulation. Two geometric parameters have main role in the simulations. We can set the number of cells in latitude with the change of k parameter and the number of cells in radius with the change of n parameter. The r_0 and Γ are also geometric parameters, $\mathrm{r}_0 = (\mathrm{R} - \mathrm{r_{mc}})/30\,\mathrm{cm}$ and $\Gamma = 6.4 \cdot 10^{10}\,\mathrm{cm}$. The $\mathrm{r_{mc}}$ is the radius to which the meridional flow penetrates from the base of the convective zone. Keeping in mind the observed depth of the tachocline, we set $\mathrm{r_{mc}} = 4.79 \cdot 10^{10}\,\mathrm{cm}$.

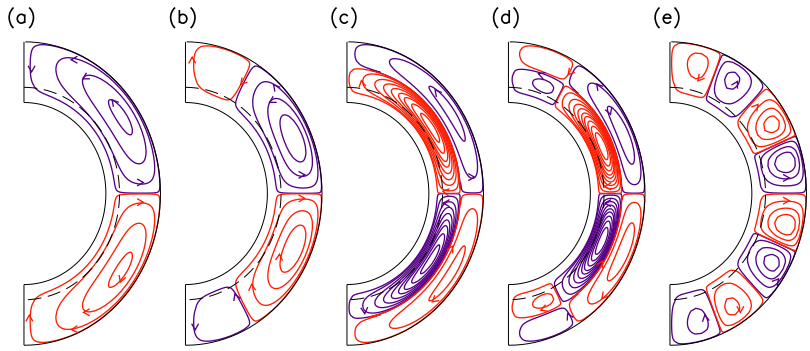

Figure 14: *Streamlines of the meridional circulation prescribed in* (35d). *(Source: Beluczet al., 2015)*

We also use an other stream function Ψ (Dikpati et al., 2010) as follows:

$$\psi r\sin\theta = \psi_0 \frac{(\theta-\theta_0)}{(\theta+\theta_0)} \sin\left[k\frac{\pi(r-R_b)}{(R-R_b)}\right] \left(1-\exp^{-\beta_1 r\theta^{\epsilon}}\right)\left(1-\exp^{\beta_2 r(\theta-\pi/2)}\right)\exp^{-((r-r_0)/\Gamma)^2} \tag{36}$$

The streamline flow can be obtained in the northern hemisphere by plotting the contours of $\psi r\sin\theta$ and in the South hemisphere by implementing mirror symmetry about the equator. The parameter values are: $\mathrm{k}=1$, $\mathrm{R_b}=0.69\,\mathrm{R_\odot}$, $\beta_1=0.1/(1.09\cdot10^{10})\,\mathrm{cm^{-1}}$, $\beta_2=0.3/(1.09\cdot10^{10})\,\mathrm{cm^{-1}}$, $\epsilon=2.00000001$, $\mathrm{r_0}=(\mathrm{R}-\mathrm{R_b})/5$, $\Gamma=3\cdot1.09\cdot10^{10}\,\mathrm{cm}$, $\theta_0=0$. This choice of the set of parameter values produce a flow pattern that peaks at a 24° latitude. The parameters depends on which meridional circulation pattern is used in particular cases.

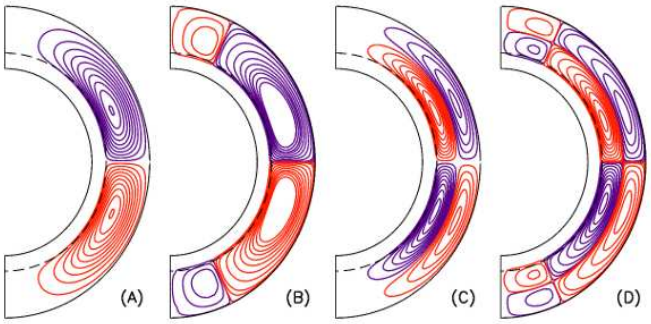

Figure 15: *Streamlines of the meridional circulation prescribed in* (36).

2.6.5. Bouldary Conditions and Solution Method

Equations (29) and (30) are solved in a full-spherical shell ($0 \geq \theta \geq \pi$), extending radially from the bottom of convection zone ($r/R_\odot = 0.6$) to the surface ($r/R_\odot = 1$). We used the 4th-order Runge-Kutta method with central finite difference scheme for r and θ derivatives to solve the equations.

The boundary conditions are obvious. Assuming the deep radiative core to behave effectively as a perfect conductor, we set $B_\phi = 0$ and $A = 0$ at the lower boundary. Both these quantities are also set to zero along the symmetry axis ($\theta = 0$ or π) to ensure regularity. To insure that the fields-lines match smoothly from northern to southern hemisphere, we have prescribed $\frac{\partial A}{\partial \theta} = 0$. At the surface, the A field satisfies the free space equation

$$\left(\nabla^2 - \frac{1}{r^2 sin^2\theta}\right) A = 0. \tag{37a}$$

A general solution to this equation can be written, (Dikpati & Choudhuri, 1994):

$$A(r \geq R, \theta, t) = \sum_n \frac{a_n(t)}{r^{n+1}} P_n^l(\cos\theta), \tag{37b}$$

$$a_n(t) = \frac{(2n+1)R^{n+1}}{n(n+1)} \int_0^{\pi/2} A(r = R, \theta, t) P_n^l(\cos\theta) \sin\theta d\theta, \tag{37c}$$

where $P_n^l(\cos\theta)$ is the associated Legendre polynomial. The derivative of A at the solar surface

$$\left.\frac{\partial A}{\partial r}\right|_{(r=R)} = -\sum_n \frac{(n+1)a_n(t)}{R^{n+2}} P_n^l(\cos\theta). \tag{37d}$$

3. Exploring the North-South Asymmetry

Solar cycles in the North and South hemispheres differ in cycle length, amplitude, profile, polar fields, and coronal structure.

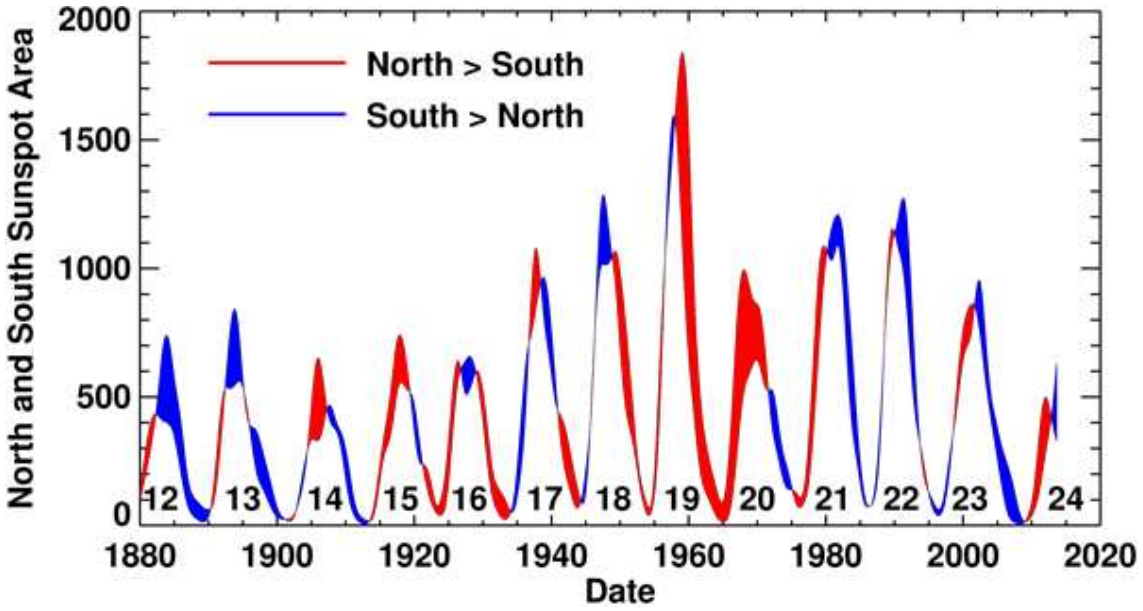

Figure 16: *Smoothed monthly sunspot areas for northern and southern hemispheres separately. The difference between the two curves is filled in red if the North dominates or in blue if the South dominates.*

(Source: Hathaway, 2015)

Statistical analyses of North-South asymmetry in solar cycle properties have been carried out for many years by using different methods and several kinds of solar cycle data, most commonly sunspot numbers and areas but also flares number, solar proton events, active prominences, solar wind velocity, interplanetary magnetic fields, geomagnetic activity indices, and galactic cosmic rays (Verma, 2000; Vernova et al., 2002; Li et al., 2002; Javaraiah, 2007; Nair & Nayar, 2008; Bankoti et al., 2010; Chowdhury et. al., 2013a; Chowdhury et. al., 2013b). (Joshi & Joshi, 2004) showed that the existence of a real N-S asymmetry which is strengthened during solar minimum. (Verma, 1993) showed that the N-S asymmetry indices for several solar phenomena of solar cycles. The study

indicates that the N-S asymmetry has a trend of a long-term characteristic time scale of about 100 yr. The solar activity was South dominated during solar cycle 21, 22, 23 and 24, but according to the predictions of the next solar cycle 25 (starting in 2020, peaking in 2025), the N-S asymmerty will shift to North hemisphere. (Verma, 2000)

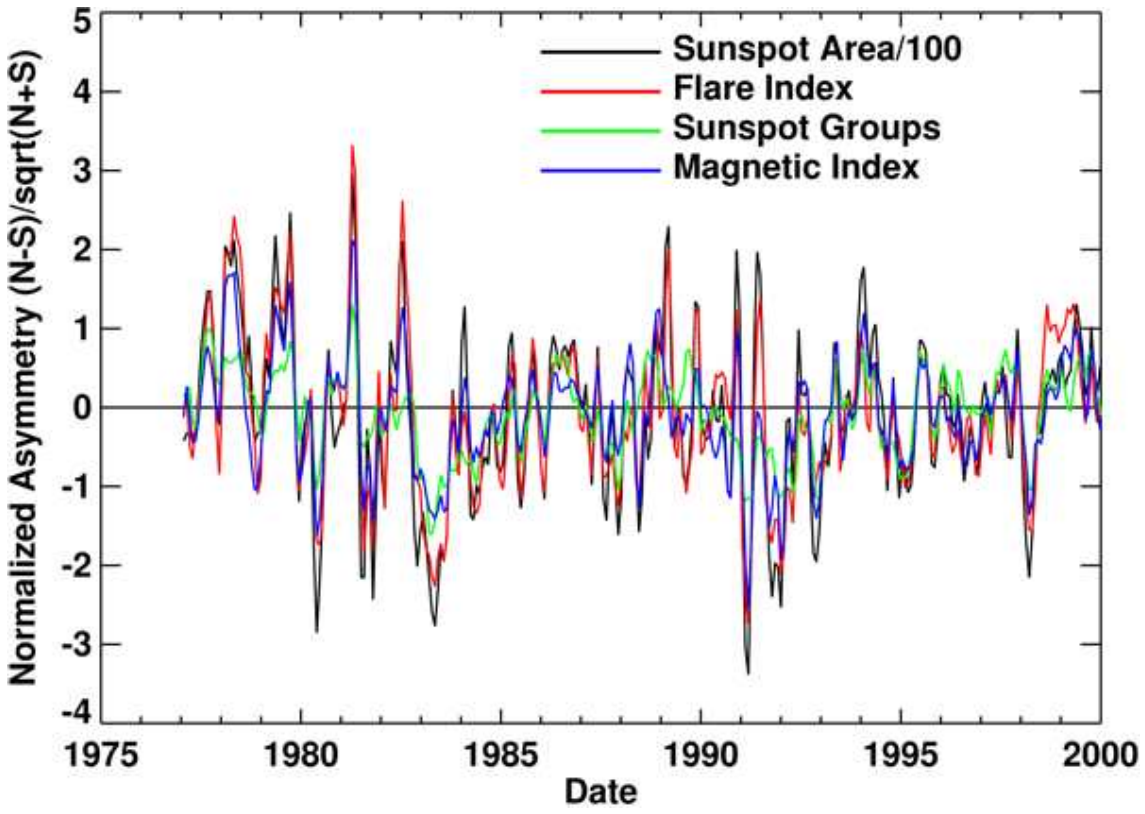

Figure 17: *Normalized North-South asymmetry* $(\mathrm{N}-\mathrm{S})/\sqrt{(\mathrm{N}+\mathrm{S})}$ *in four different activity indicators for individual Carrington rotations. Sunspot area is plotted in black. The Flare Index is shown in red. The number of sunspot groups is shown in green. The Magnetic Index is plotted in blue.*

(Source: Hathaway, 2015)

Different kinds of phase-shifts between the North-wing and South-wing of the butterfly diagram can be seen in different cycles, the amplitude and the latitude-extent of the butterfly wings in the northern and southern hemispheres are often various and the North-wing extends in latitude is often different than that of the South-wing. In some solar cycle the North-wing starts and ends before the South-wing does, although both wings start simultaneously, they end at different times. The progress of cycles can be inferred to be

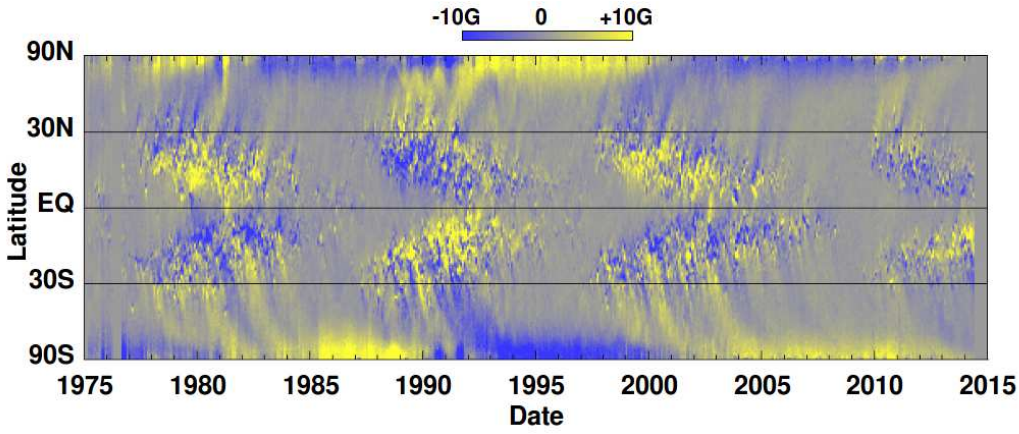

Figure 18: *A Magnetic Butterfly Diagram constructed from the longitudinally averaged radial magnetic field obtained from instruments on Kitt Peak and SOHO.*
(Source: Hathaway, 2015)

different also in the northern and southern hemispheres; the butterfly wing is often more vertical in the northern hemisphere, which means that the cycle is progressing faster in the northern hemisphere than in the southern hemisphere. The amplitude of the cycles in the northern and southern hemispheres are often different. Our purpose to investigate the two causes of such N-S asymmetry in the solar cycle pattern. One plausible source can be attributed to different Babcock-Leighton surface poloidal source in the northern and southern hemispheres. The other possibility is if the meridional circulation pattern is different; either the amplitude of the meridional circulation can be different, or there can be one-cell flow in one hemisphere, and a multi-cell flow in the other hemisphere.

3.1. Asymmetric Babcock-Leighton Poloidal Source in North and South (Belucz et al., 2013)

First, we present some results from simulation in the northern hemisphere only ($0 \geq \Theta \geq \pi/2$). The dynamo behaves like a classical $\alpha - \Omega$ dynamo as we can expect, when there is no meridional circulation. The average duration of solar activity cycle is about 11 years. We investigate the changing of the cycle length only as function of diffusivity without meridional circulation. (see Figure 19).

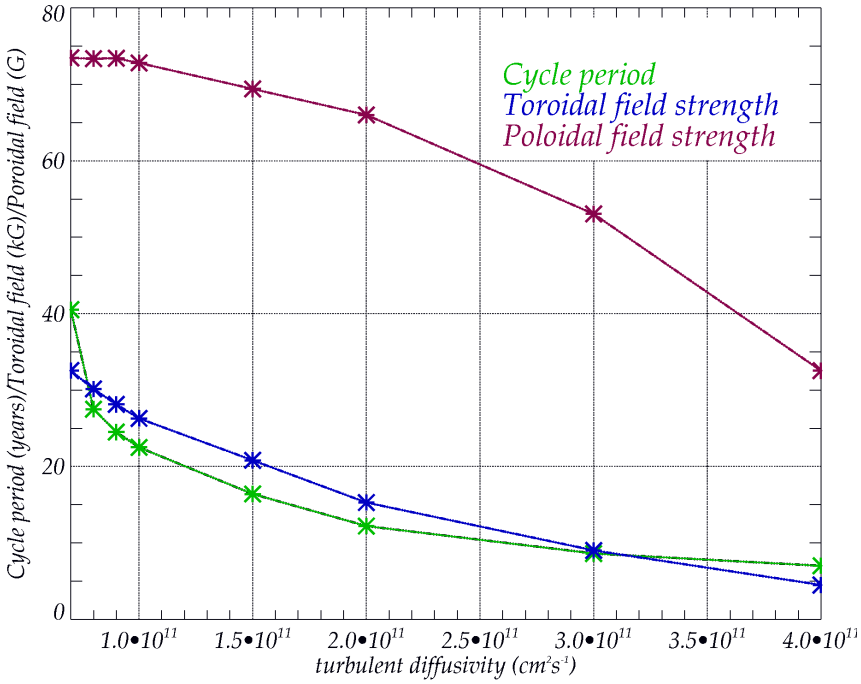

Figure 19: *The toroidal and poloidal field strength. The dynamo cycle period dependence on inverse power of* η_{T}

We simulate the dynamo in the northern and southern hemispheres. The formula for s_0 works fine when we extend our computation domain from single hemisphere to both hemispheres. We solve the induction equation in a full-spherical cell; the dynamo ingredients (symmetric differential rotation, antisymmetric α-effect, magnetic diffusivity) create the necessary connection between the two hemispheres. We carry out two simulations to examine the effect of differences in the s_0 in the northern and southern hemispheres.

We do not have meridional circulation switched on for the experiments, so this is a pure $\alpha - \Omega$ type Babcock-Leighton dynamo.

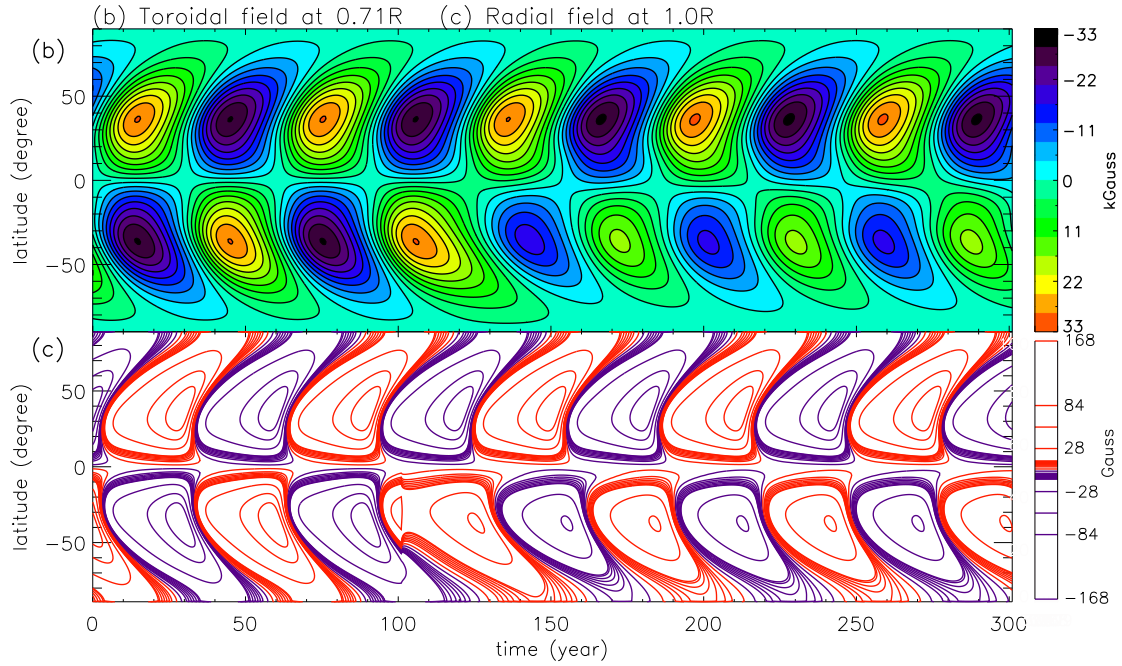

Figure 20: *Butterfly diagram for the toroidal field, taken near the bottom of the convection zone. After first two cycles, the source term in the southern hemisphere is reduced to half of its original amplitude, but the* s_0 *has its full amplitude in the northern hemisphere.*

The poloidal field is produced as a flux emergence across the solar convective envelope and the decay of the tilted bipolar active regions at the surface. The tilt of sunspot pairs away from the east-west direction, as represented by Joy's law, in effect generates the poloidal field. The nonlocal source term account for some of the properties of rising flux ropes revealed by the simulations.

We run the simulation, for the first two dynamo cycles, with a selected value of $s_0(= 3\text{m/s})$, and then we reduce the value of s_0, just in the southern hemisphere, by a factor of 2. In this case, the dynamo in both hemispheres continue to operate, but the butterfly diagram shows that the dynamo in the southern hemisphere becomes weaker (see Figure 20).

In our second simulation, we totally switch off the source term in the southern hemisphere after the first two cycles. In this case, as expected, the dynamo in the northern hemisphere continues its usual cycle, but the dynamo in the southern hemisphere does

not change sign anymore. Instead, it shows the sign of weakening, although takes a long time to completely decay away (see Figure 21).

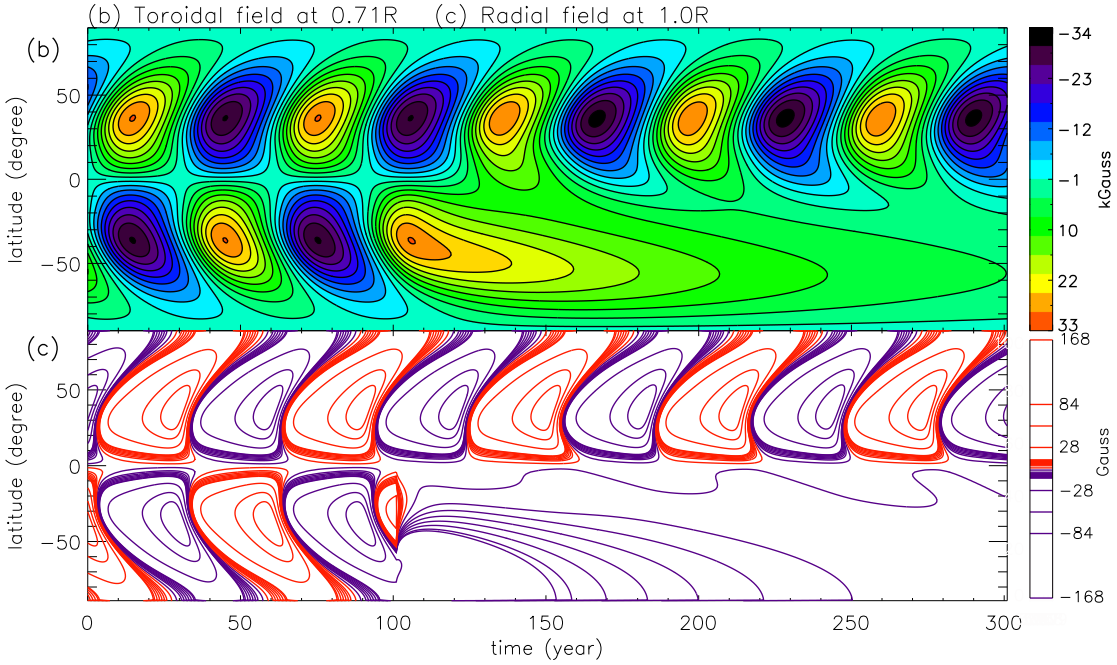

Figure 21: *After first two cycles, the source term in the southern hemisphere is switched off. The dynamo in the southern hemisphere does not produce cyclic features, instead slowly decays away.*

In the Babcock-Leighton flux-transport models, the meridional circulation determines the solar cycle period (Dikpati & Charbonneau, 1999) and sets its rise and fall patterns. Helioseismic observations of the Suns surface Doppler plasma flow from Mount Wilson Observatory data (Dikpati & Gilman, 2012) have shown that often a second reverse meridional flow cell appears at high latitudes in one hemisphere, or in both hemispheres with different sizes and amplitudes. These kind of asymmetries in meridional circulation can cause significant asymmetry in solar cycle patterns, such as in the butterfly diagram in North and South.

In general, the source-terms (Ω-effect and α-effect) and decay-terms in a dynamo model complete with each other. Depending on what term wins, the dynamo sustains or dies out. Our numerical simulations of suddenly switching off the poloidal source (s_0) in one of the hemispheres puts the dynamo under a situation that no new poloidal fields are generated, and previously produced poloidal fields will decay away under the action of

turbulent diffusion. That would eventually stop inducing toroidal fields also.

It is important to know how much time a dynamo model would take to wash out the previously generated fields if s_0 is suddenly set to zero. We perform several of such numerical simulations in our $\alpha - \Omega$ Babcock-Leighton dynamo using various initial s_0 values, and also using various turbulent diffusivity values, and we find that the decay time of the toroidal fields, after the source-term s_0 is set to zero, does not depend on the value of s_0, but it depends on the turbulent diffusivity. Figure 22 shows that the larger is η_T, the faster is the field decay.

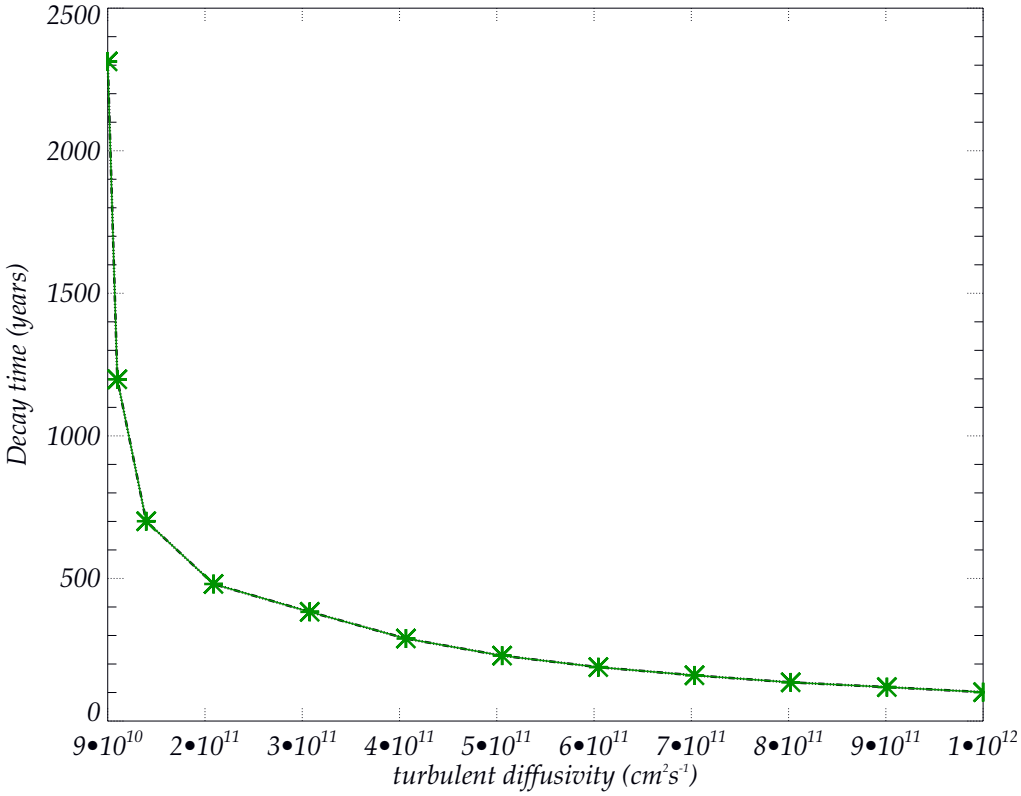

Figure 22: *Decay time versus turbulent diffusivity.*
(Source: Beluc z et al., 2013)

3.2. Asymmetry of the Meridional Circulation Pattern in the North and South Hemisphere (Beluczz & Dikpati, 2013)

In the results that follow, we first establish a reference dynamo solution that corresponds reasonably well to what is observed on the Sun but is antisymmetric about the equator. Then we carry out a sequence of simulations in which we change a property of the meridional flow in the South only, first for two periods of 3 yr and then for a much longer interval of 44 yr (∼4 sunspot cycles). All results are shown for a period of 100 yr after starting from a well-established periodic solution with steady meridional flow that has a single cell in each hemisphere containing poleward flow near the outer boundary.

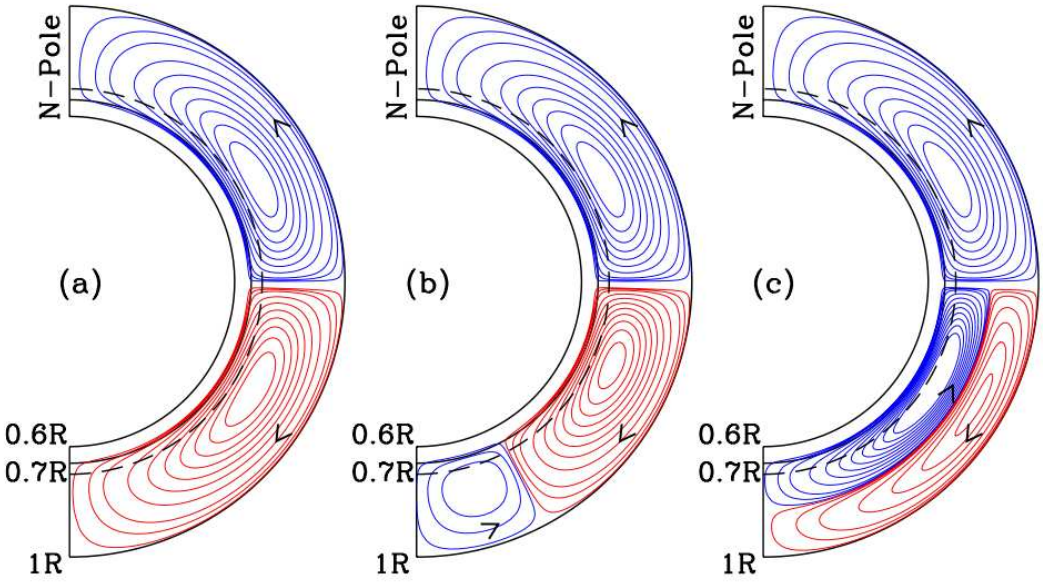

Figure 23: *Frame (a) shows a flow pattern that contains one cell in each hemisphere and is mirror symmetric about the equator; (b) and (c) show patterns containing one cell in the North and in the South, respectively, two cells in latitude and two cells in depth.*
(Source: Beluczz & Dikpati, 2013)

3.2.1. Steady Symmetric Single Cell in North and South

Figure 24 shows the reference case against which we compare all cases for which the South has different meridional circulation than the North. These patterns are produced when we use the meridional circulation shown in Figure 23, with a single cell in each hemisphere. Panel 23(a) is the surface poloidal field; panel 23(b) is the toroidal field amplitude near the bottom.

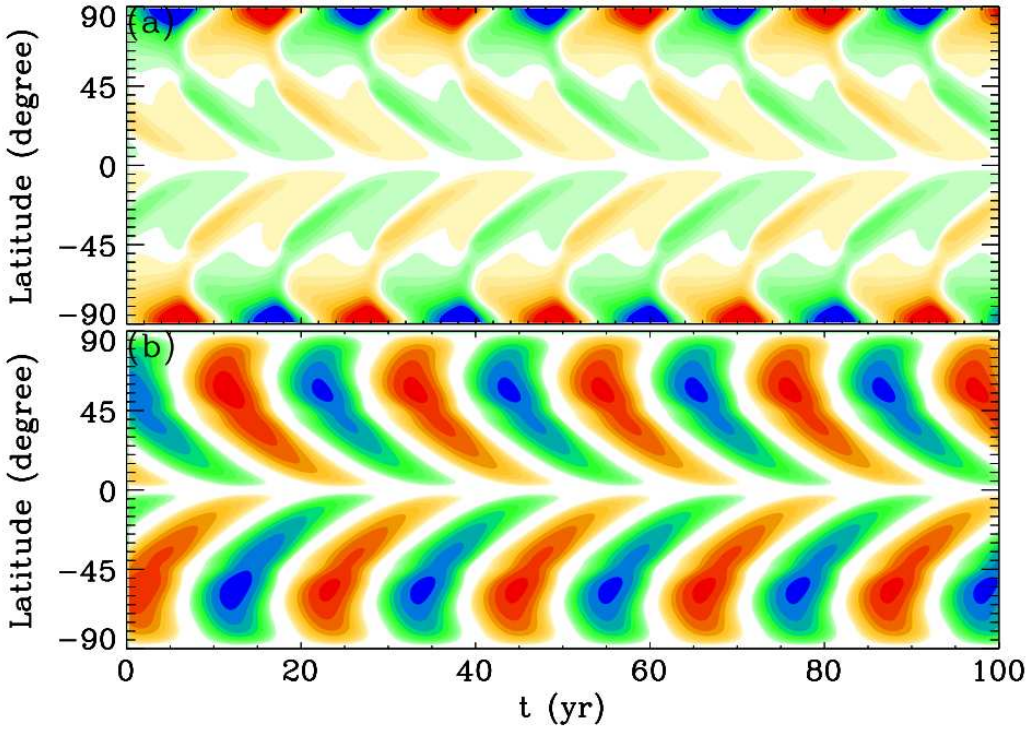

Figure 24: *Evolution of the (a) surface radial pattern and (b) tachocline toroidal field, in a time-latitude diagram, for a steady single celled meridional flow pattern that is mirror symmetric about the equator. Color-filled contours for surface radial fields (top frame) are in a linear interval of* 35 G*, with the lowest contours of* ±5 G *plotted in the lightest yellow for* $B_r = +5$ G *and in the lightest green for* $B_r = -5$ G*. For tachocline toroidal fields (bottom frame), color-filled contour levels are in logarithmic interval, six contours covering the range of one order of magnitude; the highest tachocline toroidal field is* ∼ 60 kG *(deep red/blue).*

(Source: Beluc̆z & Dikpati, 2013)

The butterfly wings are obvious, as is the appropriate phase relation between the surface polar field and the peak in toroidal field. That is, the polar field changes sign near the maximum in the toroidal field and reaches its maximum near the minimum of the toroidal field in mid-latitudes. The meridional flow is chosen so that the dynamo period is slightly longer than 20 yr. The toroidal field peak does occur at a higher latitude than is inferred for the Sun from the location of sunspots, but that detail does not seem that important for this study.

3.2.2. Varying Circulation Amplitude in South

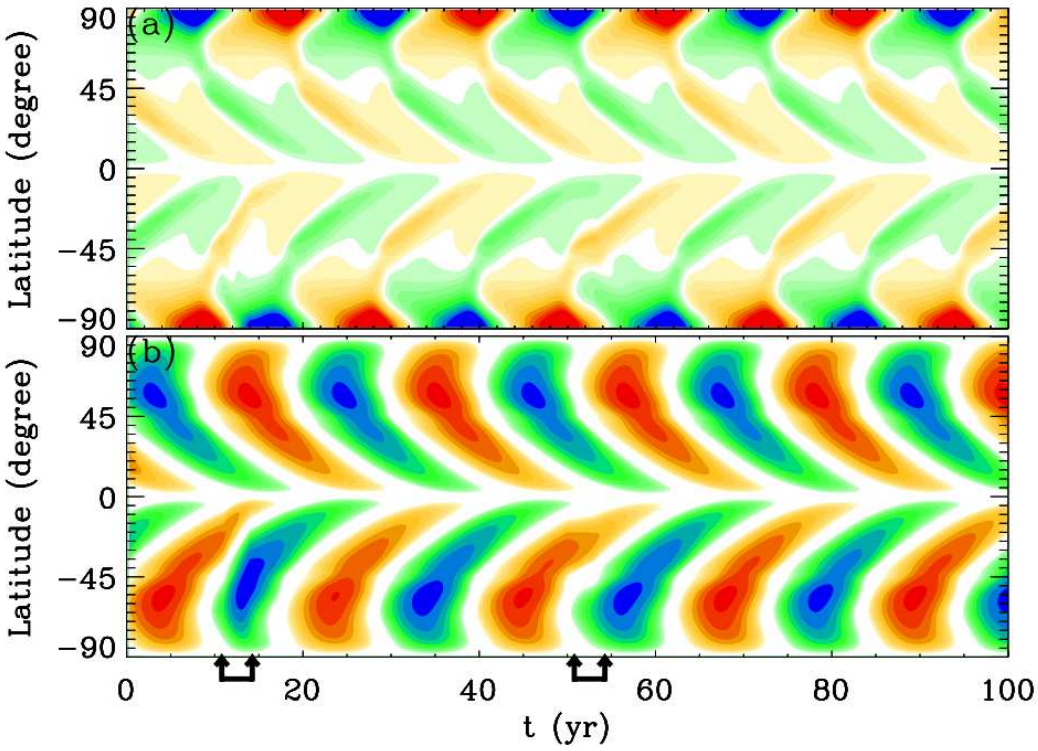

Figure 25: *Same as in Figure 24 but for a meridional flow pattern in which flow speed in the South is varied two times for 3 yr during a 100 yr simulation: starting at the 11th year and ending at 14th year, flow speed in the South is increased to double the flow speed in the North, and starting at the 50th year and ending at the 53rd year, the flow speed in the South is decreased to half the flow speed in the North for 3 yr.*

(Source: Beluczz & Dikpati, 2013)

In Figure 25, we give results for a 100 yr simulation in which during years 11-14 we have doubled the amplitude of meridional flow in the South only and during years 50-53 we have reduced it by 50%. We can see that because of the increased flow speed, the cycle phase advances faster in the South than the North, so the polar field peaks sooner in the South, and the next half cycle in the toroidal field does also. This phase-lead is preserved until the next change in meridional circulation, at 50 yr. But that is not the only effect. In the South, the peak in toroidal field migrates closer to the equator during the speedup, and the peak polar field is weaker than the peaks of both previous and following cycles. All of these changes are easily explained by the action of meridional flow. The faster cycle phase advancement is directly caused by the increased flow carrying toroidal field toward the equator faster and the poloidal field faster to the poles. This causes the peak toroidal fields to be found closer to the equator in that half cycle and weakens the polar field because it spends less time near the pole at a time close to its maximum value, before it is swept down to the bottom. Once the increased meridional flow speed is removed, subsequent cycles look much more like cycles before the speed was increased. But the phase of the South continues to be a few years ahead of the North.

The effect of slowing down the flow in years 50-53 has the effect of slowing down the phase advancement of the toroidal and polar fields in the South. The half cycle that immediately follows the change is now longer than the ones before and after it, resulting in a renewed synchronization of phase between the North and the South. However, we do not see much amplitude change in either the toroidal or poloidal field. This is probably due to the particular choice of 50-53 yr, which occurs just after the change of sign in toroidal fields at the highest latitudes and just before the sign change in polar fields.

What happens when the meridional flow speed is doubled in the South for a much longer duration, for example, 44 yr? Figure 26 gives answer. The most obvious effect is that the cycle period in the South is now half as long as it was before. The peak toroidal field is substantially weaker, which we should expect. Because the meridional flow advects it faster from high latitudes to low, the peak resides at a given latitude for a shorter time, giving less time for the latitudinal shear of the differential rotation to amplify it by shearing the poloidal field near the latitude of the peak. By contrast, the polar fields are about the same as for the lower meridional flow speed. For this to occur, two nearly compensating effects are required. The weaker toroidal field produces less surface poloidal flux in low and middle latitudes, but the faster poleward meridional flow carries what is produced faster toward the poles, so there is less loss by diffusion, and

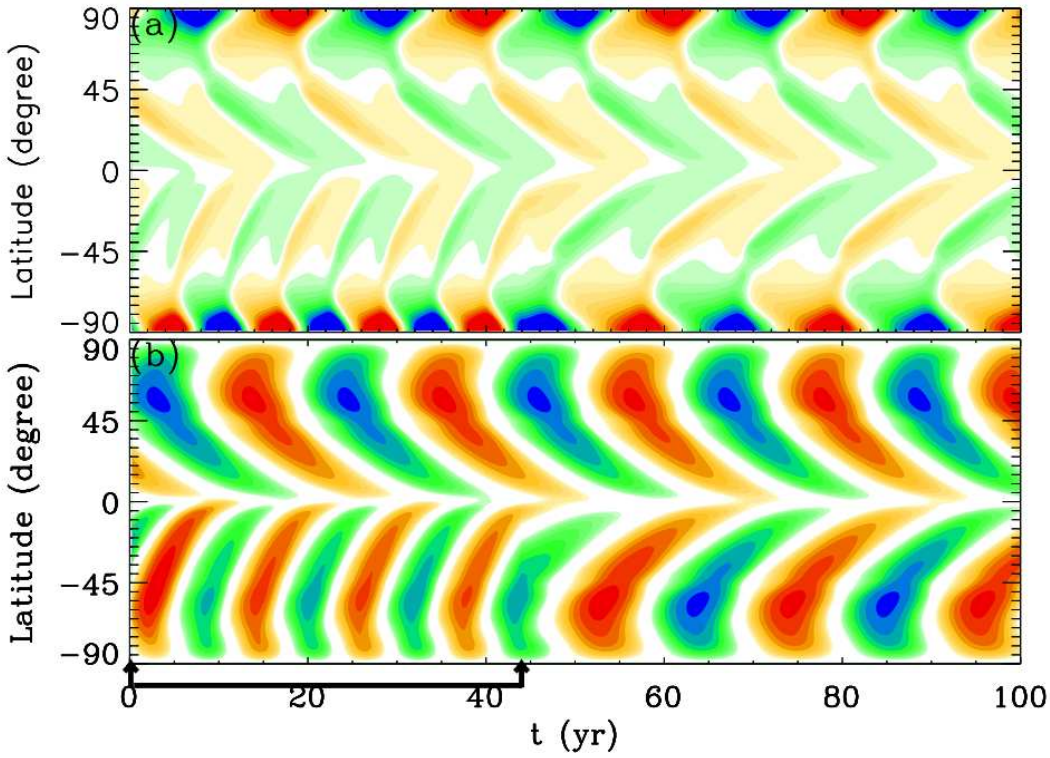

Figure 26: *Same as in Figure 24 but for a meridional flow pattern in which flow speed in the South is increased to double the flow speed in the North, for the first 44 yr of the simulation run.*

(Source: Beluczz & Dikpati, 2013)

then packs it more tightly against diffusion when it gets there.

Because of the duration of the higher flow speed, beyond the end of the 44 yr the South leads the North by about half a sunspot cycle, or 5 yr. This lead persists to the end of the simulation period shown. We have run this calculation for a few hundred more years, during which the South continues to lead. Throughout the whole simulation, the North changes virtually not at all, confirming that the linkage between hemispheres is weak.

3.2.3. Intermittent Second Cell in Latitude in South

In the next simulations we present, instead of changing the strength of the meridional circulation for a few or many years, we add a second, reversed meridional circulation at high latitudes. The form of this meridional circulation is shown in Figure 23(b). The

peak speed of the primary cell is held fixed, but the latitude of this peak is somewhat lower. The boundary between cells is near 60° latitude. The results for the same two 3 yr intervals as used before are shown in Figure 27.

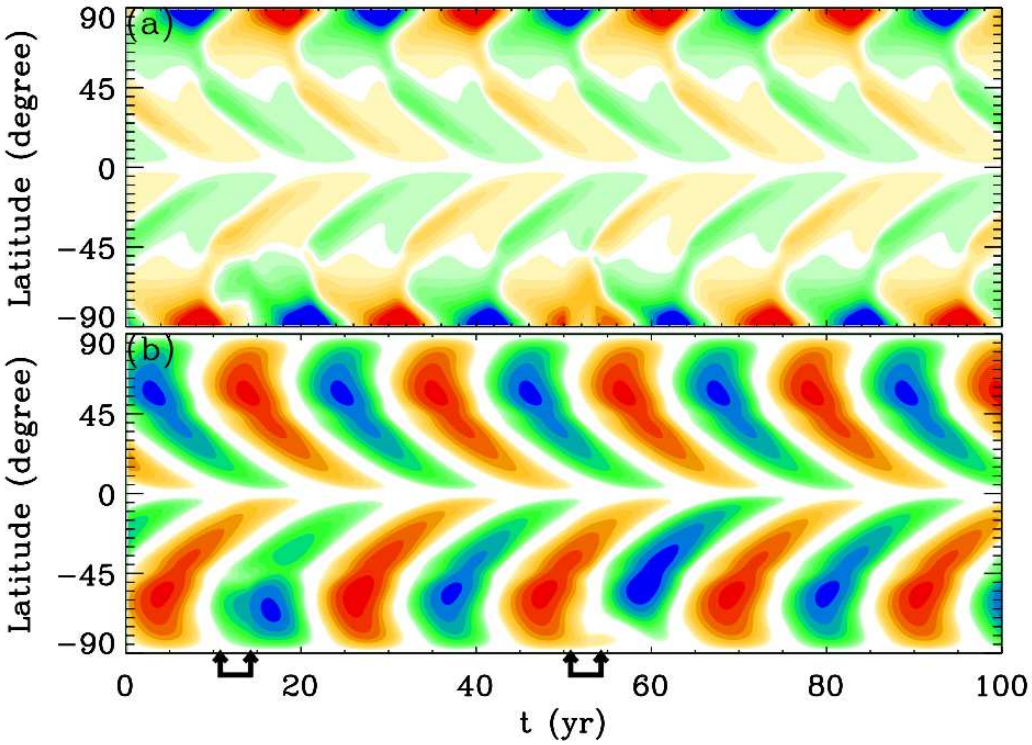

Figure 27: *Same as in Figure 24 but for a meridional flow pattern in which a high-latitude second reverse flow-cell appears in the South two times for 3 yr during 100 yr of simulation run: once starting at 11th year and ending at 14th year and a second time starting at the 50th year and ending at the 53rd year.*

(Source: Belucz & Dikpati, 2013)

We see that the effect of the second cell is to substantially prolong the rising phase of the cycle, as seen in the plot of toroidal field, and to delay the subsequent peak in the polar field. The low latitude toroidal field is weaker than it would have seen otherwise, and the strongest high-latitude toroidal field extends to a higher latitude.

All of these effects come from the presence of the second cell. The ascending phase of the toroidal field always starts near 60°, which is now near the boundary of the two cells. This placement causes some of the poloidal flux from above to be advected toward the pole near the bottom, helping to produce more toroidal field there. There is less poloidal

flux going toward the equator that is carried by the primary cell, so there the toroidal field does not amplify as much. The peak in polar field is delayed, because the temporary equatorward flow near the outer boundary prevents the poloidal flux from being advected there. But when the second cell is switched off, the primary cell takes over and completes the delayed poleward transport. Because of the lengthening of the ascending cycle phase, the whole cycle becomes longer than it would otherwise be, but this effect is absent in the next cycle. Nevertheless, the phase lag in the South introduced by the 3 yr presence of the second cell persists.

The second 3 yr interval of a second reversed cell produces different effects because it is introduced at a different phase in the cycle. Here, it occurs in the late declining phase of the toroidal field. Now the downflow near 60° gives the new cycle a head start with poloidal flux at a lower latitude than it would have been, so the peak in the toroidal field is closer to the equator and the ascending phase is shorter. At the same time, the peak polar field in the South is substantially reduced for that cycle. Because of the timing, the reversed cell has prevented the maximum in polar field from forming, because while it is present it is carrying flux away from the pole, some of which goes to the bottom near 60° to be sheared there to start the toroidal field. In the late descending phase of the high-latitude toroidal field, one can see a weak extension toward the pole, due to the second cell carrying some poloidal flux there to be sheared by differential rotation, but that goes away in the next half cycle because there remains very little poloidal flux there to be sheared.

When we keep the second reversed cell for 44 yr, as shown in Figure 28, we get even more profound changes. We get a pronounced high-latitude branch to the butterfly diagram, because now there is a steady advection of poloidal flux toward the pole near the bottom that is sheared by the differential rotation there. The pattern tilts forward in time closer to the pole, just as the low latitude pattern tilts forward in time toward the equator. The basic period is also somewhat shorter because the length of the primary conveyor belt is shorter, since the downflow is at 60° rather than at the poles. The poleward and equatorward parts of the butterfly diagram remain roughly in phase with each other because of the particular amplitude chosen for the second cell relative to the primary cell. That is, it takes roughly the same amount of time for the toroidal field pattern to go from 60° to the pole as it does to the equator. Obviously, other choices are possible, for which the relative phases would change significantly from cycle to cycle in low latitudes compared with high latitudes.

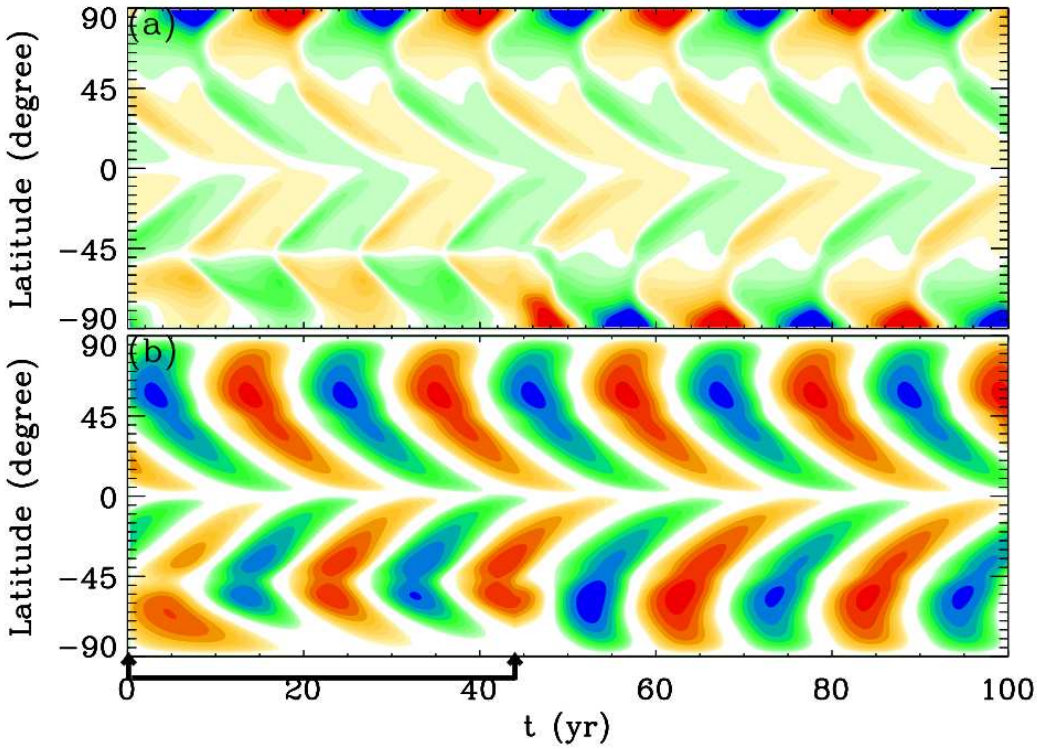

Figure 28: *Same as in Figure 24 but for a meridional flow pattern in which a high-latitude second reverse flow-cell prevails in the South for the first 44 yr of the simulation run. (Source: Beluczz & Dikpati, 2013)*

We see also in Figure 28 that while the second cell is present, the polar fields are much weaker than they otherwise would be. This is not only because the equatorward flow there keeps the field from concentrating at the pole but also because the surface poloidal source is much weaker there compared to what is present at low latitudes. Some of the poloidal flux at high latitudes near the bottom originates at lower latitudes near the top.

Finally, in the first complete half cycle in the South after the second cell has been removed, we get a particularly strong toroidal field. This is because poloidal flux that was being divided between polar and lower latitude branches is now all available for advection toward the equator and because the amplification of toroidal field in this branch starts at a higher latitude than before.

3.2.4. Intermittent Second Cell in Radius in South

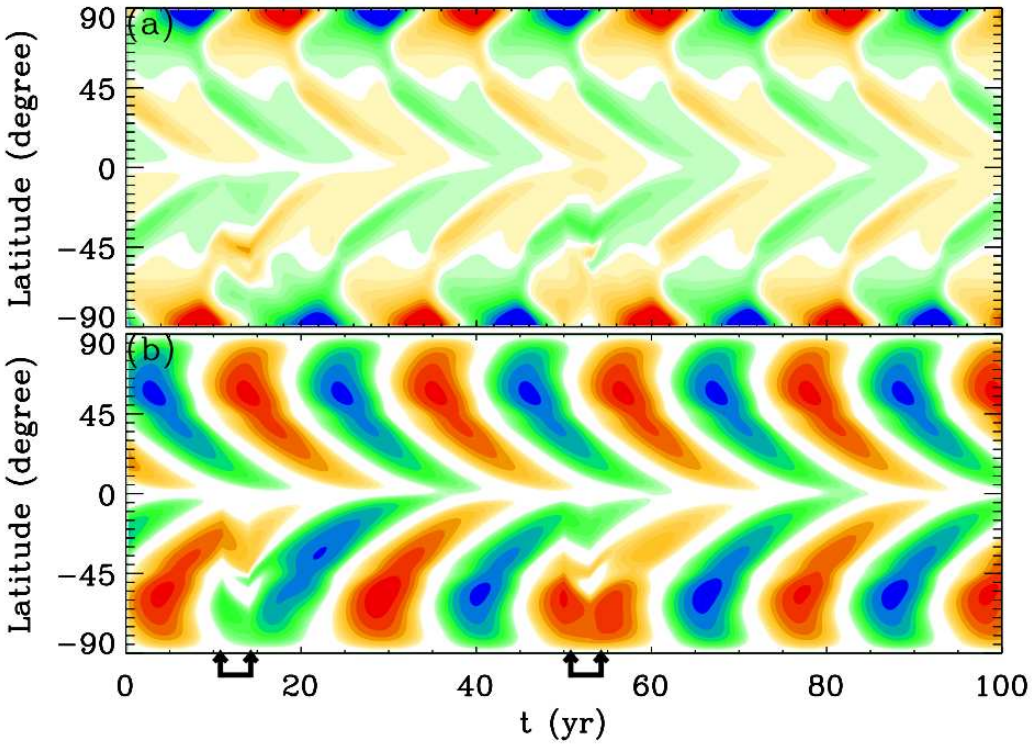

Figure 29: *Same as in Figure 24 but for a meridional flow pattern in which a second anticlockwise flow-cell below the primary clockwise cell appears in the South two times for 3 yr during a 100 yr simulation: once starting at the 11th year and ending at the 14th year and a second time starting at the 50th year and ending at the 53rd year.*

(Source: Belucz & Dikpati, 2013)

The results when we turn on a second meridional flow cell below the primary one for the same two 3 yr intervals as used above, so that at the bottom there is now flow toward the poles, are shown in Figure 29. This pattern is produced using the meridional circulation shown in Figure 23(c). We see that the effect on the butterfly diagram is immediate, in the form of a 3 yr reversal in the direction of migration of the toroidal field with time. This is seen clearly in both time intervals. As soon as the single cell with depth is restored, the equatorward migration resumes. The net effect on the dynamo period is to lengthen by 4-5 yr the cycle present when the circulation change was switched on. Once past the intervals of circulation change, the butterfly wing reverts to its original form and period. However, the phase lag in the South is retained so that the toroidal fields are

nearly in phase in North and South hemispheres. Many more cycles are needed to regain the correct phase difference of roughly half a spot cycle.

We can also see that subsequent to the first interval of changed circulation, the South polar field is much weaker than earlier. This is because the toroidal field that produced the surface poloidal source for this cycles South pole field was weaker at middle and high latitudes. By contrast, the second interval of circulation change leads to a long period of enhanced high-latitude toroidal fields, from which a relatively strong South pole field was produced. Thus, the effect on polar fields is sensitive to the phase of the cycle for which the circulation changed.

The change in direction of migration of peak toroidal fields when the second cell in radius is added is what we should expect for a dynamo in which the primary mode of migrating the peak toroidal field is advection by the meridional flow.

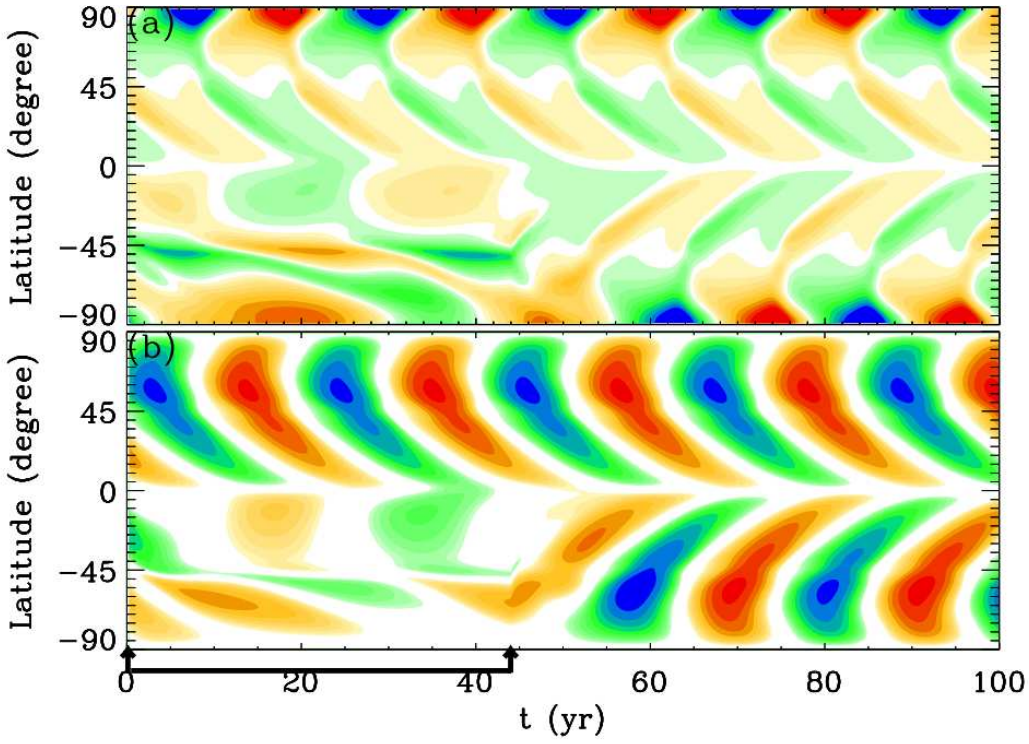

Figure 30: *Same as in Figure 24 but for a meridional flow pattern in which an anticlockwise flow cell below the primary clockwise cell prevails in the South for the first 44 yr of the simulation run.*

(Source: Belucz & Dikpati, 2013)

Results from a second cell in radius switched on for 44 yr are shown in Figure 30. Here the changes in both toroidal and poloidal fields are much more dramatic. In the latitude range $0° - 45°$, toroidal field migration essentially stops, while at high latitudes it migrates toward the pole at a relatively high rate. The South polar field maxima are much weaker than before, spread out in time, with irregular time spacing. In this case, equatorward of about $45°$, poleward migration due to the reversed meridional flow near the bottom is approximately balanced by the "$\alpha - \Omega$" dynamo wave effect causing propagation toward the equator. At higher latitudes this effect is reversed in sign, so that both meridional flow and dynamo wave properties are causing the toroidal field to migrate relatively quickly toward the pole. The weaker polar fields are a consequence of the weaker toroidal field at all latitudes that leads to a weaker surface poloidal source term.

Once the second circulation cell is switched off, within one full magnetic cycle the South butterfly diagram "wing" returns to essentially what it was before the second cell was switched on. In this particular example, the phase lag introduced by the second cell was close to a complete magnetic cycle period, so that after the effects of that change have disappeared, the North and South have returned to nearly the correct phase relation. Had we chosen a different time interval than 44 yr, that would not have been the case.

One might argue in the case of a second cell in radius that the proper toroidal field to use to produce a butterfly diagram becomes the toroidal field at mid-depth, where the meridional flow is still toward the equator. Perhaps there the butterfly diagram will look more solar-like. The problem with this reasoning is that in this class of models the toroidal field generated is much larger near the bottom, because of the lower turbulent magnetic diffusivity taken there. We should expect the surface butterfly pattern to be produced from the depth where the induced toroidal field is largest, regardless of the circulation pattern. Furthermore, there is a problem with keeping the toroidal field at mid-depth when magnetic buoyancy is working. Near the bottom, in the tachocline, the subadiabatic stratification expected there can hold the toroidal flux for long enough to amplify it to values large enough to produce sunspots seen at the surface.

4. Examining the Role of Complex Multi-cellular Meridional Circulation Pattern in the Babcock-Leighton Solar Dynamo Model (Belucz et al., 2015)

Over the past two decades Babcock-Leighton type solar dynamo models operating with single celled meridional circulation have been successful in reproducing many global solar cycle features, including equatorward migration of sunspot belts, poleward drift of poloidal fields and correct phase relationship between them (Wang et al., 1991; Choudhuri et. al., 1995; Durney, 1995; Dikpati & Charbonneau, 1999; Küker et al., 2001; Bonanno et al., 2002; Nandy & Choudhuri, 2001; Guerrero & Muñoz, 1995; Jouve et al., 2008), and have reached the stage that they can be used for making solar cycle predictions. Meridional circulation works in the flux-transport dynamo models like a conveyor-belt, carries a memory of the magnetic fields and enables the flux-transport dynamos to predict future solar cycle properties, similarly, like the great-ocean conveyor-belt carry signatures from the past climatological events and influence the determination of future events. (Dikpati & Gilman, 2006) has a simulation for the solar cycle 24 amplitude, and predicts that cycle 24 will be 30%-50% stronger than the cycle 23. Now we know that this forecast may not be validated. One of the reasons is that the steady, single-celled meridional circulation in both hemisphere may be oversimplified for the Sun. Both observations and models indicate that there may be more than one cell in either depth or latitude, or both, in each hemisphere, at least at some times.

Using time-distance helioseismology the most recent observations from SDO/HMI data show evidence of meridional circulation with two cells in depth (Zhao et al., 2013). Ring-diagram analysis from Gong data infer that the surface flow is poleward up to about $\sim 60^\circ$ latitude (Haber et al., 2013; Basu & Antia, 2010; Komm et al., 2012), whereas Doppler measurements from MWO data, which can measure this flow at higher latitudes, show a high-latitude, reverse flow associated with the primary poleward surface

flow (Ulrich, 2010). Using a very long-term GONG database and applying time-distance technique (Kholikov et al., 2014) have found signatures of equatorward return-flow in the lower half of the convection zone, indicating a long deep one cell flow-pattern. A p-mode perturbation analysis by (Schad et al., 2013) infers four cells in latitude, each going down to about 0.8R. Thus observations do not yet give us a unique answer about the Suns meridional circulation pattern.

Models indicate more complex patterns and model outputs vary from model to model. For example, mean-field models produce a long, counterclockwise primary cell often associated with a weak, reverse cell at high latitudes, both extending down to the bottom of convection zone (Kitchatinov & Rüdiger, 2005; Dikpati, 2014), whereas full 3D convection simulations produce multiple cells in latitude and depth (Guerrero et al., 2013; Featherstone & Miesch, 2015). The helioseismic measures observed the poleward meridional flow at the solar surface, but the form of the internal return flow is at present unconstrained observationally. The flow speed of the meridional circulation depends little or no on depth down to $r/R = 0.95$ and meridional flow decreases with depth (Schou & Bogart, 1998), but the measures currently do not provide accurate information at greater depth. However, deep in the envelope nearly all his simulations are characterized by an equatorward return flow that penetrates below the interface between the nominally stably stratified interior and the unstably stratified envelope (Dikpati & Charbonneau, 1999). Analysis of long-term meridional flow data available at Mount Wilson Observatory (MWO) shows a reversed meridional flow cell at high latitudes, poleward of 60° or so, during solar cycle 19, 20, 21 and 22. The second cell disappeared during most of cycle 23, but has reappeared during the ascending phase of the current cycle 24. Surface Doppler measurements are more able to measure meridional flow at the highest latitudes than are helioseismic measures, since latitudinal flow is nearly parallel to the line of sight there (Dikpati, 2014). Given the lack of knowledge about the uniqueness of meridional flow from observations and models, it is necessary to consider all plausible meridional circulation patterns for the Sun, and explore their effects on a Babcock-Leighton solar dynamo model.

Guided by the observational and modeling results cited above, we study the effects of multi-cellular meridional flow patterns on a Babcock-Leighton solar dynamo model operating in a full spherical shell of the convection zone. In a full spherical shell model, the equator is no longer a boundary of the computational domain and this fact is allows to study the issue of parity problem in flux-transport dynamo models. These include in each hemisphere Figure 14(a) a single cell with a poleward flow at the surface; Figure

14(b) a long primary cell from the equator to about 60° latitude, associated with a second, reversed cell at high latitudes; Figure 14(c) two cells in depth; Figure 14(d) two cells in depth and two in latitude; and Figure 14(e) four cells in latitude.

Using a Babcock-Leighton flux-transport dynamo model, simulations have been done for some of these multi-cells meridional circulation pattern; for example (Bonanno et al., 2005) explored a dynamo operating with two similar cells in latitude, the cell with poleward surface flow extended from the equator to the mid-latitude instead of up to 60° in latitude. They verified that the equatorwards migration in the butterfly diagram can be easily obtained by the combined action of two cells of meridional circulation. (Jouve & Brun, 2007) have simulated a Babcock-Leighton flux transport dynamo with four similar cells meridional circulation pattern that has two cells in depth and two in latitude. They confirmed that adding cells in latitude tends to speed up the dynamo cycle and adding cells in radius more than triples the period. They find, that the cycle period in the four cells model is less sensitive to the flow speed than in the other simpler meridional circulation profiles studied. In contrast with these simulations, we studied the effect of four-celled meridional circulation pattern containing two long cells in depth extending up to about 60° latitude and then associated with two small reversed cells in depth at the poles Figure 14(d). (Zhao et al., 2013) did not confirm whether the poleward surface flow continues up to the pole or stops at high latitudes. On the other hand, surface Doppler measurements indicate that the surface flow is poleward up to a certain high latitude (Ulrich, 2010) and then reverses beyond that.

We examine which of the five circulation patterns, mentioned in Figure 14(a-e), can produce cyclic features similar to the Sun. Furthermore, we perform a systematic parameter survey to compare dynamo model simulations for all five circulations using the same model and the same dynamo physics, and judge which models that use these circulation patterns can be calibrated to the Sun in diffusion and advection dominated regimes.

4.1. Time-latitude Diagrams for Multi-cell Flow

4.1.1. Reference Case

First, we establish a reference case dynamo solution, to which other individual solutions can be compared, to see what changes are created by changing the meridional circulation pattern.

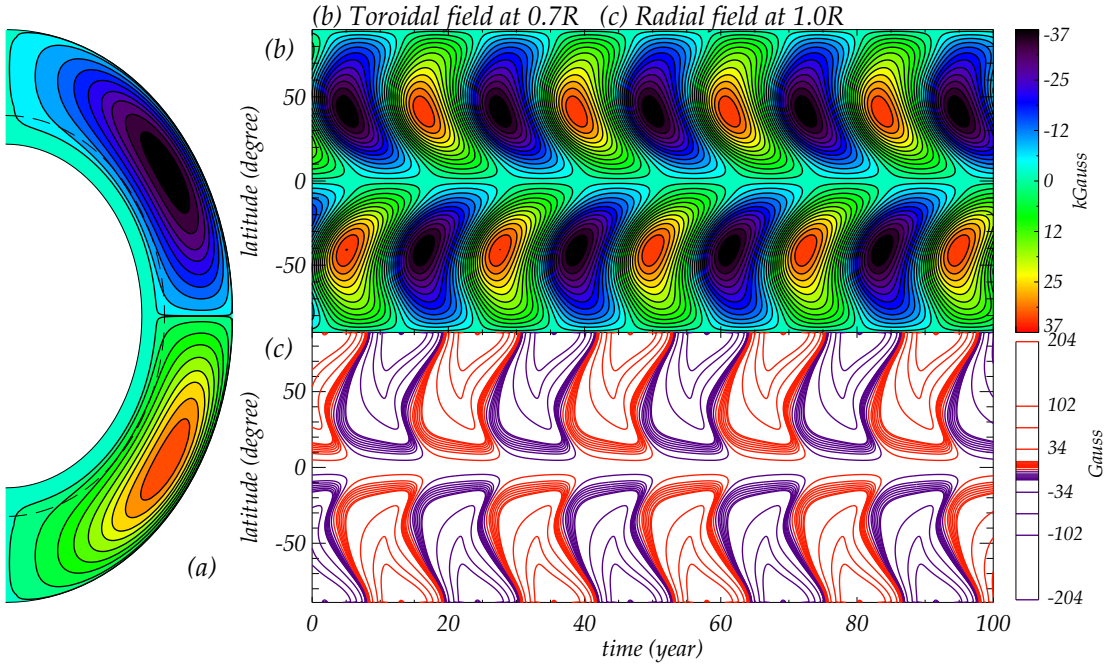

Figure 31: *Panel (a) displays the streamlines for single-celled meridional circulation in each hemisphere; blue-violet represents counterclockwise flow, green-orange clockwise flow. Panel (b) shows the time evolution of the tachocline toroidal field; panel (c) the same for surface radial fields. For tachocline toroidal fields, color-filled contour levels are* 3 kG*; the highest tachocline toroidal field is* $\sim$ 37 kG *(yellow/violet). The maximum value of the radial fields is* $\pm$210 G*, occuring near the poles.*

(Source: Beluc et al., 2015)

We choose for reference the frequently used single-cell meridional circulation that has poleward flow near the outer boundary, and return flow at the base of the convection zone (see Figure 14(a) and Figure 31(a)). This flow penetrates slightly below the tachocline. The thin black dashed semicircular arc represents the location of the center of the tachocline. Two frames, (b) and (c) on the right panel of Figure 31 show the

time-latitude diagrams respectively of toroidal field at the bottom of convection zone ($B_\phi|_{r=0.7R}$) and surface radial field ($B_r|_{r=1R}$). To get these results we took a maximum surface flow speed of $15\,ms^{-1}$, poloidal source amplitude of $s_1 = 3.0\,ms^{-1}$ and turbulent diffusivity $\eta_T = 3 \cdot 10^{11} cm^2 s^{-1}$.

Babcock-Leighton flux transport dynamo models with one-celled meridional circulation in each hemisphere can reproduce many features of the solar cycle. These include (i) the equatorward migration of toroidal flux at lower latitudes; (ii) the 11-year sunspot cycle; (iii) the observed phase-shift between poloidal and toroidal components; (iv) the short rise of toroidal field to maximum followed by the long decline to minimum - in the reference case, the ascending phase is 16.77% of the whole cycle; (v) peak tachocline toroidal fields are 37 kG; (vi) peak surface radial fields are ± 210 G, similar to values obtained by many previous authors (Wang et al., 1991; Choudhuri et. al., 1995; Durney, 1995; Dikpati & Charbonneau, 1999; Dikpati & Gilman, 2001; Rempel et al., 2005; Dikpati & Gilman, 2006; Jouve & Brun, 2007; Schrijver & Liu, 2008; Dikpati et al., 2010; Belucz & Dikpati, 2013). This solution also reproduces the observed phase shift between the surface poloidal field and the toroidal field at the tachocline; the poloidal field polarity changes from positive to negative when the toroidal field is near maximum and its polarity is negative.

Figure 32 shows how the poloidal and toroidal fields evolve through a sunspot cycle for the entire meridional cross-section. When the toroidal field is strong, it is confined to the lower layers of the domain, and its peak is clearly migrating toward the equator, along with the poloidal field lines that are sheared by differential rotation to produce it. We expect sunspots to emerge from at or near the latitude of maximum in the toroidal field. The reversal of polar fields is seen here in the interval between 5 and 6.25 years, at which time the toroidal is a maximum with its peak near 20°.

How dependent are the results described above on the particular choice of turbulent magnetic diffusivity? We address the question by repeating the dynamo simulations for the five meridional circulations using a lower value, $7 \cdot 10^{10}\,cm^2 s^{-1}$. These results are displayed in Figures 33-42. Figure 33 displays the reference case with single circulation cellfor the lower magnetic diffusivity. Panel (b) gives the toroidal field amplitude near the bottom, panel (c) the surface poloidal field. We use the same peak surface flow speed ($15\,ms^{-1}$) and poloidal source amplitude ($s_1 = 3.0\,ms^{-1}$) as for the solution seen in Figure 31.

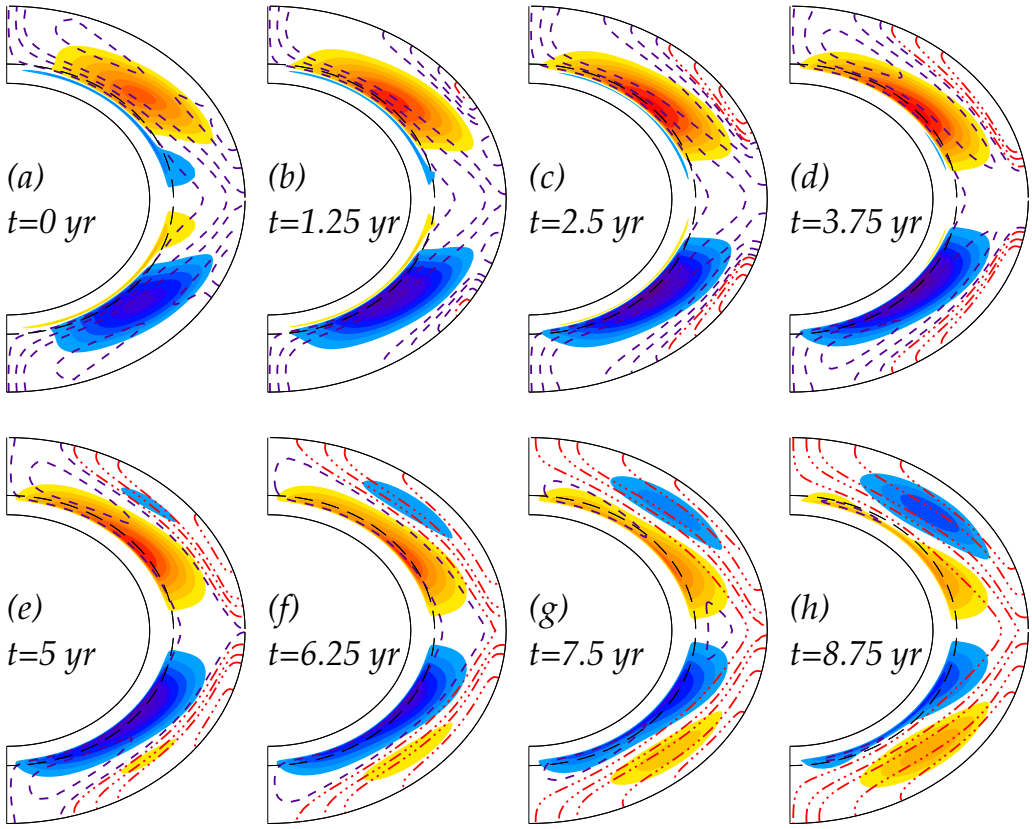

Figure 32: *Evolution of toroidal and poloidal fields with one-cell meridional circulation (Figure 14(a)). The filled contours show toroidal fields, yellow/red colors denoting positive (into the plane of the paper) and blue/purple negative (out of the plane). Red and blue contours respectively denote positive (clockwise) and negative (anticlockwise) poloidal fieldlines.*

(Source: Beluc z et al., 2015)

In lower diffusivity case, the model still reproduces the observed phase shift between the surface poloidal field and the tachocline toroidal field. Due to the the lower turbulent diffusivity, much stronger fields are produced. The highest tachocline toroidal field is 52 kG, and the maximum value of the radial fields is ± 208 G near the poles. The period is also somewhat longer than in Figure 31, namely 12.7 years, as measured by the time between adjacent peaks in toroidal and poloidal field at the same latitude. But there is also significant overlap between adjacent cycles, so the time between the high latitude

peak of a new sign of toroidal field to its disappearance at low latitudes is more than 20 years. How much overlap there is in the Sun itself is unclear, since from observations we know where the tachocline toroidal field is only from the latitude of sunspots seen. The slight poleward migration of tachocline toroidal fields seen at high latitudes comes from the strong negative radial shear there overcoming the relatively weak equatorward advection of toroidal field by the meridional flow there.

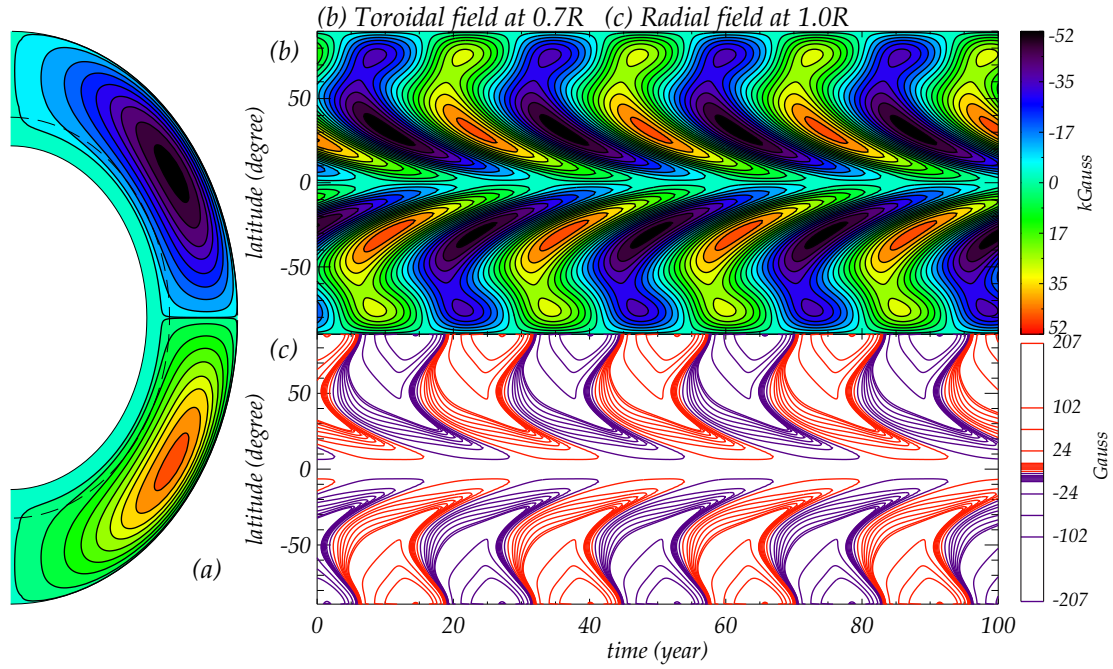

Figure 33: *Same as in Figure 31 but the turbulent diffusivity is* $7 \cdot 10^{10}\,\mathrm{cm^2 s^{-1}}$. *The highest tachocline toroidal field is* 52.4 kG *(red/violet). The maximum value of the radial fields is* ± 208 G *near the poles.*

(Source: Beluczet al., 2015)

4.1.2. Primary Cell with a High-latitude Second Reverse Flow-cell

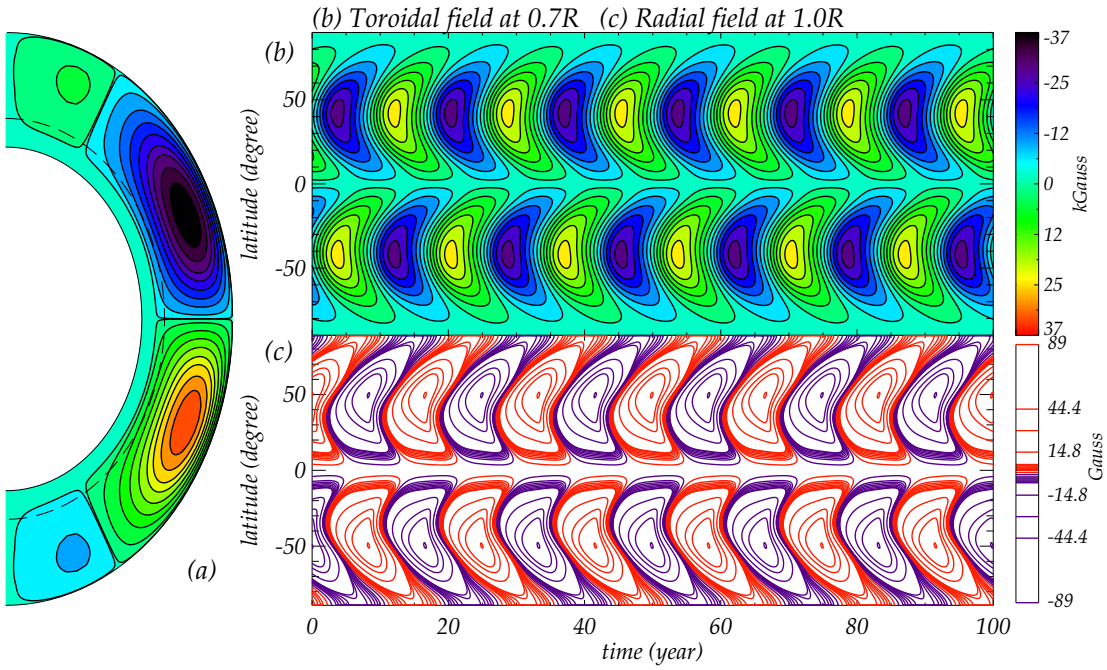

Figure 34: *Same as in Figure 31 but the meridional flow pattern has a high-latitude second reverse flow-cell (Figure 14b). The highest tachocline toroidal field is similar to that in Figure 31,* $\sim$ 37 kG *(yellow/violet). The maximum value of the radial fields is* $\pm$90 G*, at about* 50°

(Source: Beluc z et al., 2015)

In the next simulations, we study how the characteristic features of butterfly-diagram change when the meridional circulation cell contains a second, high-latitude, reverse cell. The form of this meridional circulation is shown in Figure 14(b) and Figure 34. The peak flowspeed of the primary cell is still 15 ms^{-1}, poleward at the surface, but the latitude of this peak is slightly lower, at 25.3°. The peak flow speed of the secondary cell is 3 ms^{-1}, equatorward at the surface. The boundary between cells is near 61° latitude.

The right panel of Figure 34 shows the time-latitude diagrams of $\mathrm{B}_\phi|_{\mathrm{r=0.7R}}$ in panel (b) and $\mathrm{B_r}|_{\mathrm{r=1R}}$ in panel (c). Not surprisingly, due to the effect of the second cell, a more pronounced poleward branch can be seen in the butterfly diagram of toroidal field in panel (b) compared to that in Figure 31. The sunspot cycle length (i.e. half magnetic

cycle) is just 8.3 years, due to the shorter primary conveyor belt. The strength of toroidal field is similar to that of reference case, 37 kG. Comparing the time-latitude diagrams of Figure 31(c) and 34(c), we find that the polar field peaks around 55° latitude instead of peaking near the pole as in the case of a single cell in each hemisphere. This is due to flow convergence at 61° latitude instead of at the pole. The second cell also causes a delay in the polarity change by advecting polar fields away from the pole.

The rise of the cycle from minimum to maximum in this case is slightly longer compared to that in the single cell case. This is probably because some of the poloidal flux advected to the bottom in between the primary and secondary cells is advected toward the poles, retarding the early production of the equatorward migrating branch of toroidal field there.

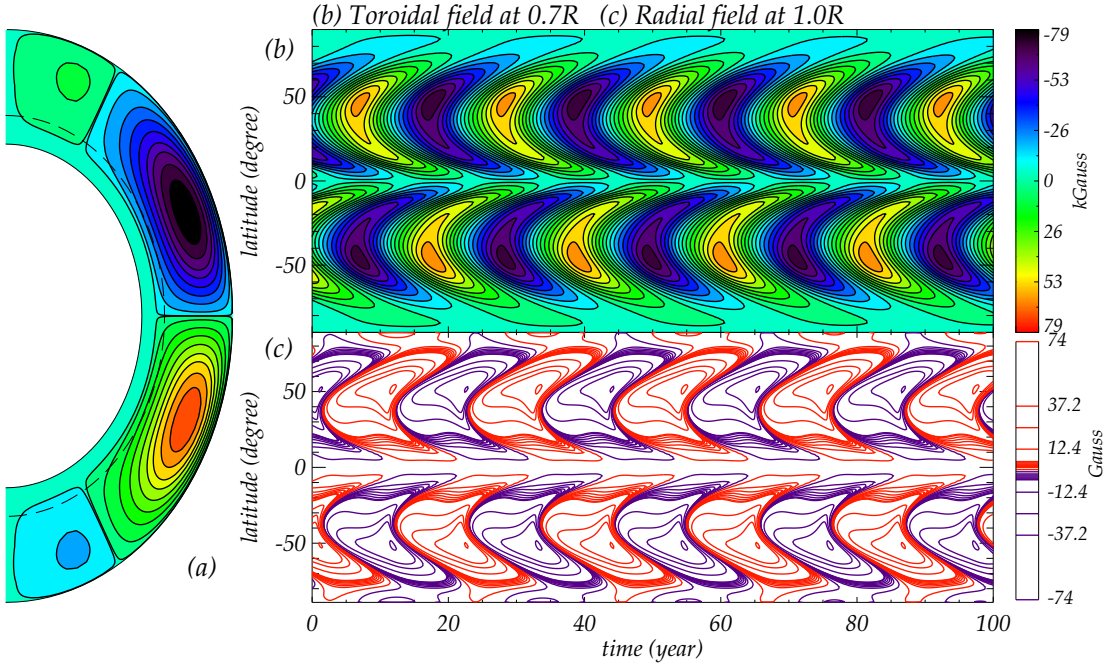

Figure 35: *Same as in Figure 34 but the turbulent diffusivity is* $7 \cdot 10^{10}\,\mathrm{cm^2 s^{-1}}$. *The highest tachocline toroidal field is* $\sim 78\,\mathrm{kG}$ *(red/violet). The maximum value of the radial fields is* $\pm 77\,\mathrm{G}$, *occuring near* 50°.

(Source: Beluc z et al., 2015)

Figure 35 shows the time-latitude diagrams of toroidal and radial fields in the two cell case (Figure 35a) with $7 \cdot 10^{10}\,\mathrm{cm^2 s^{-1}}$ turbulent diffusivity. For this case we see that the high and low latitude branches of the butterfly diagram for tachocline toroidal field

are about the same, despite the unequal amplitudes of the two circulation cells. Both the poleward meridional circulation at the bottom and the radial gradient of rotation in high latitudes at tachocline depths are contributing to this pattern, which is more pronounced than seen in Figure 33, for which the bottom meridional circulation is toward the equator at high latitudes. The sunspot cycle is shorter, about 10.7 years, due to the shorter conveyor belt that is the primary circulation cell. Here too, the induced toroidal field are stronger than in the high diffusivity solution with the same meridional circulation. The maximum value of the toroidal field is 78 kG; maximum radial field is 77 G. In this case we get substantially less overlap of adjacent cycles than in the higher diffusivity reference case (Figure 34).

4.1.3. The Two Similar Cells in Depth

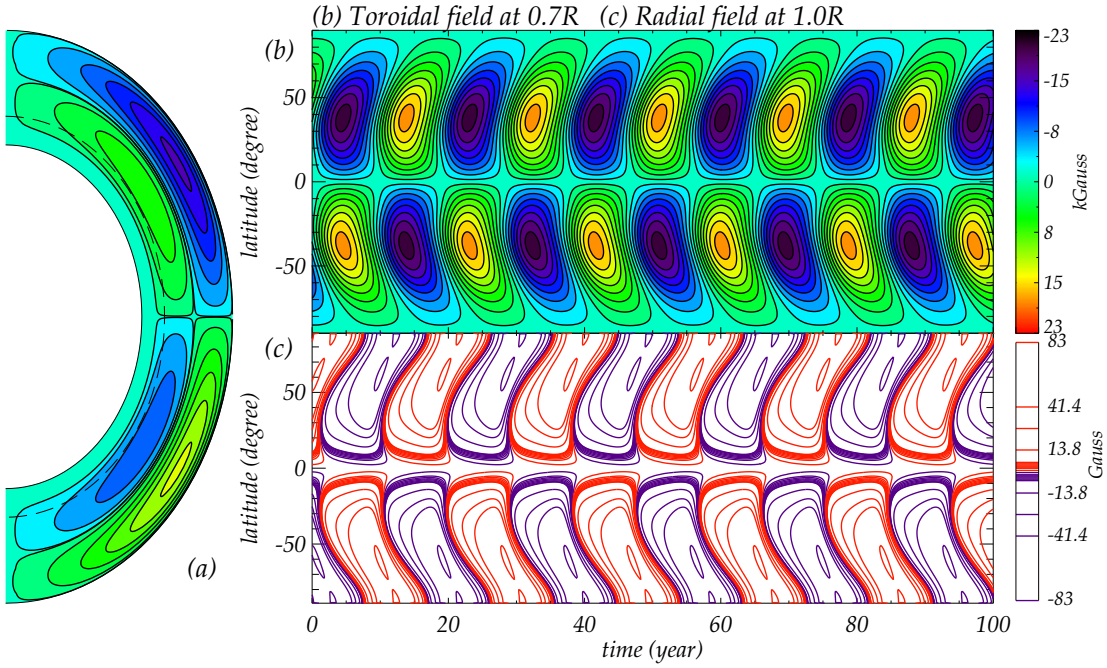

Figure 36: *Same as in Figure 31 but the meridional flow pattern has a second, reversed flow-cell below the primary cell (Figure 14c). The maximum tachocline toroidal field strength is* $\sim$ 23 kG *(orange/violet). Maximum value of the radial fields is* $\pm$ 83 G*, near the poles.*

(Source: Belucz et al., 2015)

For the next simulation, we add a second, reversed meridional cell below the primary cell (see Figure 14c). The two cells are similar in amplitude and radial extent. The results for this meridional flow are shown in Figure 36.

This dynamo solution is very different from the reference case. At all latitudes, the tachocline toroidal field is migrating with time toward the poles rather than the equator. The rate of this migration increases with latitude. This is due to the poleward flow at the bottom of the second cell. Thus, based on tachocline toroidal fields, this meridional circulation pattern produces an antisolar butterfly diagram. The toroidal field at the bottom of the domain is weaker than in the reference case, because polar fields are not brought down from the top, but instead are advected from lower latitudes near the bottom.

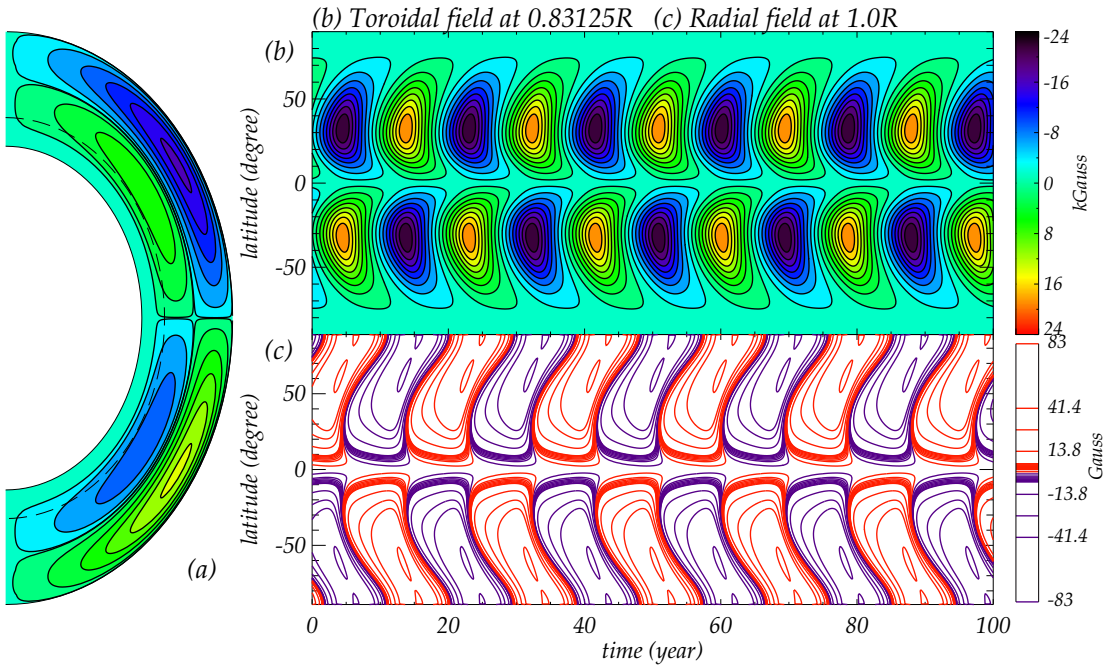

Figure 37: *Same as in Figure 36 but the toroidal fields are shown from* 0.83125 R. *A solar-like butterfly diagram is obtained to equatorward flow there.*

(Source: Beluczet al., 2015)

If we plot instead the toroidal field near the middle depth, for example, 0.83125 R, shown in Figure 37, we get a more solar-like butterfly, with both poleward and equatorward branches. This is because at these depths both circulation cells have equatorward flow, so they advect toroidal field toward the equator in lower latitudes. The relatively high speed total flow there also makes the dynamo period shorter (6.25 yr). In addition,

since in this case the poleward flow near the outer boundary reaches to a shallower depth, less poloidal flux is advected toward to the pole. These weaker polar fields lead to weaker toroidal fields at all latitudes.

In the next simulation, with low diffusivity, we turn on a second meridional cell below the primary cell, as for the case previously displayed in Figure 36. The results are shown in Figure 38. The most outstanding feature of the butterfly diagram is the longer sunspot cycle, about 50 years. What little migration of toroidal field there is, is toward the poles, leading to a slightly antisolar butterfly. Here, again, as in the higher diffusivity case shown in Figure 37, toroidal field contours (not shown) at mid-depth of the convection zone, yields a butterfly diagram with both poleward and equatorward branches.

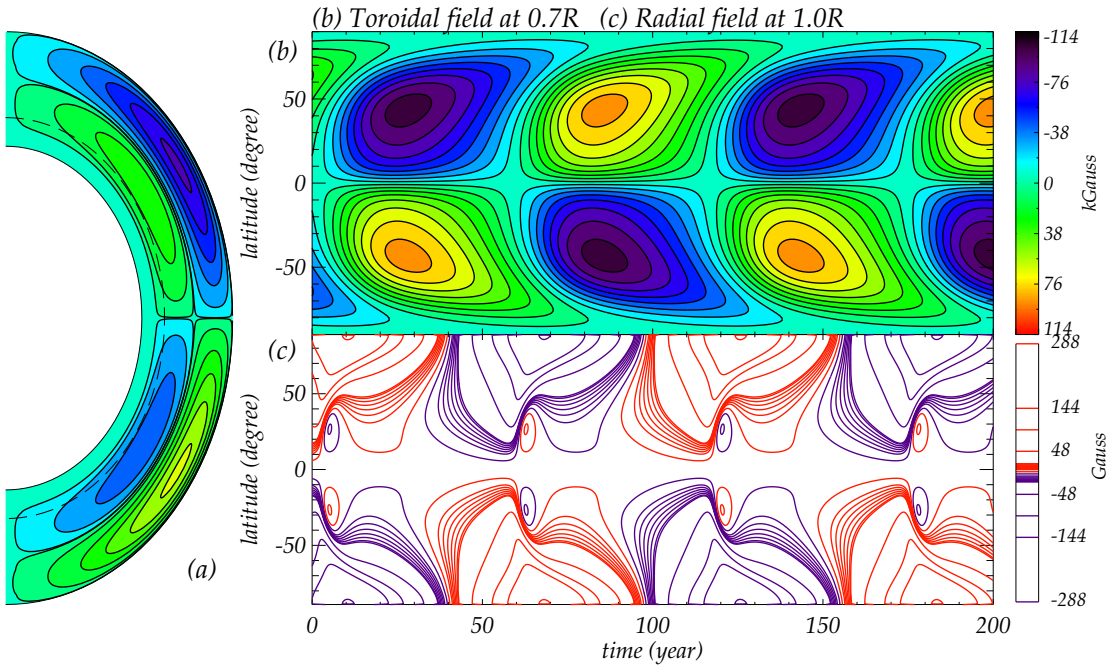

Figure 38: *Same as in Figure 36 but the turbulent diffusivity is* $7 \cdot 10^{10}\,\mathrm{cm^2 s^{-1}}$. *The highest tachocline toroidal field is* $\sim 114\,\mathrm{kG}$ *(red/violet). The maximal value of the radial fields is* $\pm 288\,\mathrm{G}$, *near the poles.*

(Source: Belucz et al., 2015)

4.1.4. Two Meridional Cells in both Latitude and Depth

The next dynamo simulation is for the case of two meridional cells in both latitude and depth in each hemisphere. The amplitudes of upper and lower cells is about the same. These results are shown in Figure 39. Panel (b), again, shows the toroidal fields near the bottom of convective zone. Panel (c) depicts the surface radial field. As in the case of two cells in radius, we again get an anti-solar butterfly diagram when we plot the toroidal field at the bottom. Again, this is because the flow is toward the pole at the bottom of the stack of cells at all latitudes except the highest. If we plot the toroidal field contours at mid-depth (not shown), we will again get a solar type butterfly, as seen in Figure 37. In comparison with that case, the dynamo period here is longer because the meridional flow speed is lower.

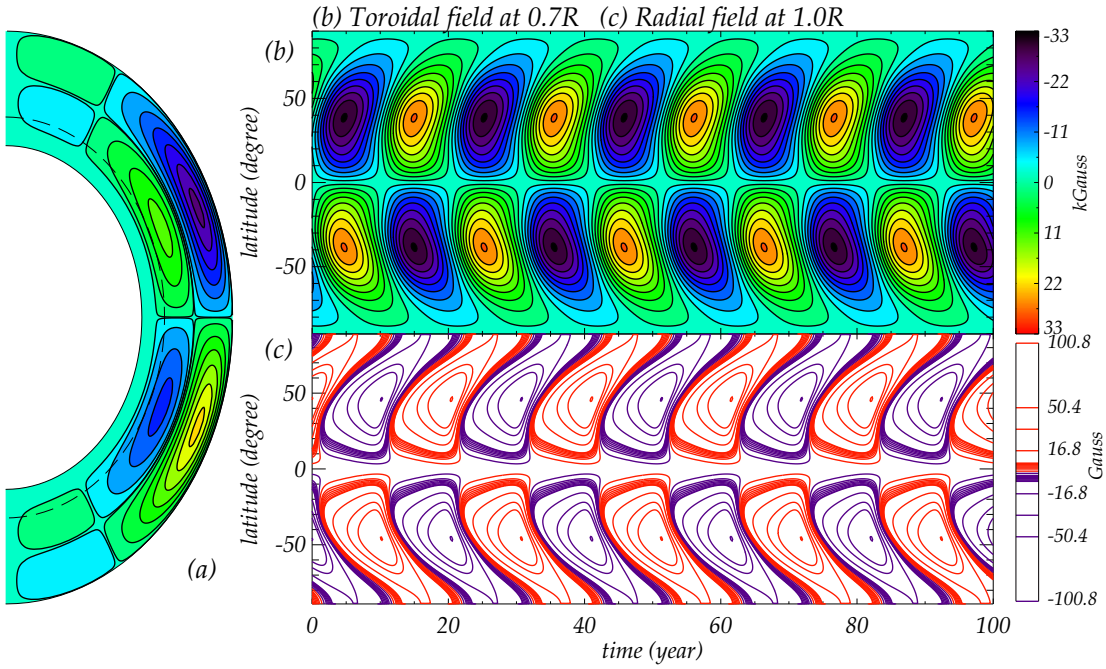

Figure 39: *Same as in Figure 31 but the meridional flow pattern has four flow-cells (Figure 14d). The highest tachocline toroidal field is* $\sim 33\,\mathrm{kG}$ *(yellow/violet). The maximum value of the radial fields is* $\pm 100\,\mathrm{G}$*, at around* $50°$*.*

(Source: Beluc et al., 2015)

The results of the next simulation is shown in Figure 40. Here, with two strong cells in low and mid-latitude, and two reversed relatively weak cells in polar latitudes, we again found a predominantly antisolar butterfly. Because of the low diffusivity, we actually get

a double set of butterfly wings. But both are tilted toward the poles with time. Since near the bottom, the latitudinal flow changes sign near 50°, only the low latitude butterfly wing can be due to poleward advection of toroidal field; the high latitude wing must come from radial shear of poloidal field there by the radial gradient of rotation. Finally, here again we can get a solar like butterfly for low and middle latitudes if we plot toroidal field contours at mid-depth in the dynamo domain.

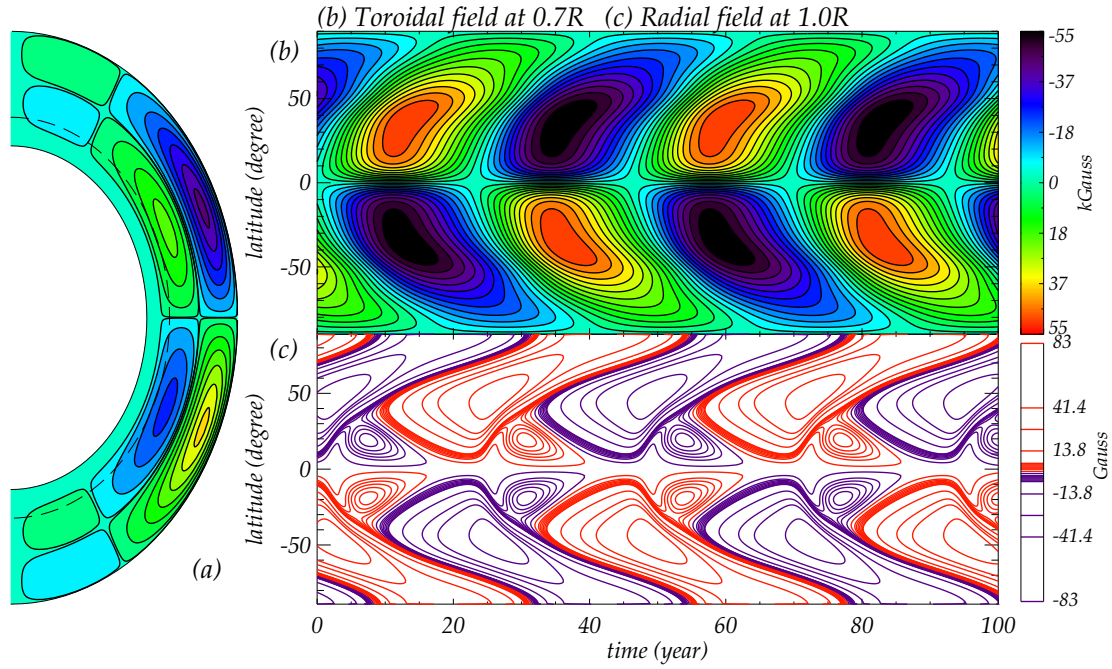

Figure 40: *Same as in Figure 39 but the turbulent diffusivity is* $7 \cdot 10^{10}\,\mathrm{cm^2 s^{-1}}$. *The highest tachocline toroidal field is* $\sim$ 123 kG *(red/violet). The maximum radial field is* ± 120 G, *from about* 50° *to near the poles.*

(Source: Beluczet al., 2015)

4.1.5. Four Cells

In the last simulation, we also have four cells, but these cells are located side by side, as seen in the Figure 14e. In this case (Figure 41), the fields are confined to lower latitudes because the multiple cells in latitude prevent poloidal field transport all the way to the poles as in the reference case. We get a solar-like time-latitude diagram up to about 22°; the toroidal field migration is equatorward. We do not see dynamo activity beyond

about 50°. The cycle length is very short, 3.125 years due to the very short conveyor belts represented by the two circulation cells closest to the equator. The strength of the toroidal field is just half of the reference case, because the dynamo is confined to the lower latitudes where the differential rotation is smaller so the production of toroidal field from a given poloidal field is smaller.

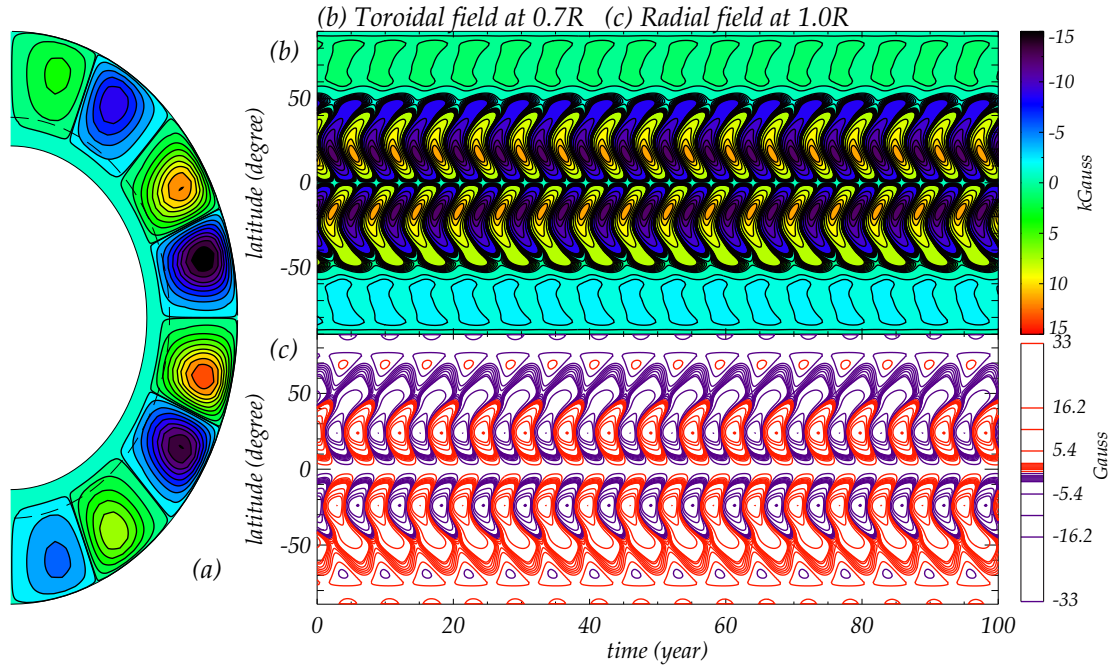

Figure 41: *Same as in Figure 31 but the meridional flow pattern has four flow-cells (Figure 14e). The highest tachocline toroidal field is* $\sim 15\,\mathrm{kG}$ *(red/violet). The maximal value of the radial fields is* $\pm 33\,\mathrm{G}$*, which occurs near* 25°.

(Source: Beluc et al., 2015)

In the last simulation, we show results for low diffusivity in Figure 42. Due to the short conveyor belts, decreasing the turbulent diffusivity does not significantly change the cycle length. But the lower turbulent diffusivity has other effects. First, the fields are stronger, as we should expect. Second, we can see dynamo activity at higher latitudes than in the high diffusivity case, though it is still low compared to that low latitudes. The orientation of the wings of the time-latitude diagram at the different latitudes is determined by the latitudinal direction of the flow near the bottom; equatorward flow leads locally to migration toward the equator, and poleward to migration toward the poles, as seen in Figure 42b.

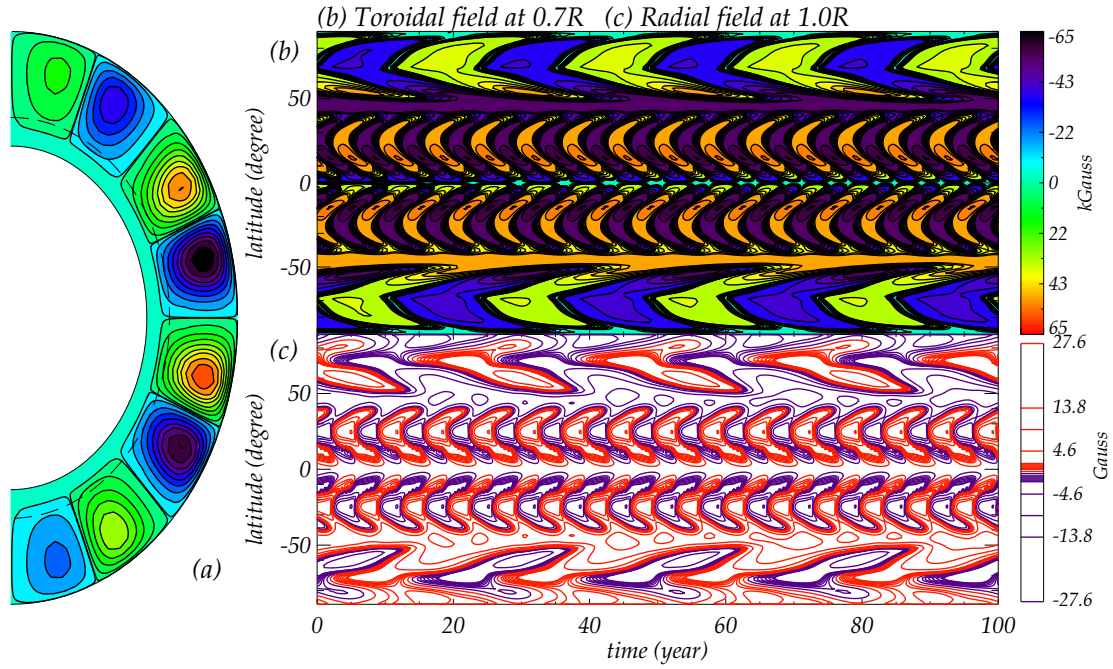

Figure 42: *Same as in Figure 8 but the turbulent diffusivity is* $7 \cdot 10^{10}\,\mathrm{cm^2 s^{-1}}$. *The highest tachocline toroidal field is* $\sim 65\,\mathrm{kG}$ *(red/violet). The maximum value of the radial fields is* $\pm 29\,\mathrm{G}$.

(Source: Beluczet al., 2015)

From all the time-latitude plots shown above, we can see that the most solar-like diagrams are produced if there is a single primary circulation cell in each hemisphere, with possibly a weaker secondary, reversed cell in polar latitudes. Circulation with two cells in depth, or two cells in both latitude and depth, give solar-like butterflies only from toroidal fields at mid-depth, not the bottom. For these to be correct for the Sun, the toroidal fields at the bottom must not come to the surface because of their magnetic buoyancy or for any other reason, and a mechanism must exist that keeps mid-depth toroidal fields from rising buoyantly too fast to be amplified to produce sunspots. Neither requirement is easily satisfied using known MHD processes.

4.2. Parameter Survey

We have shown how solutions from a solar flux transport dynamo model differ for different forms of meridional circulation. The solutions we obtained are all for the same differential rotation, since from helioseismic measurements that is relatively well known for the Sun. These were found for fixed meridional circulation amplitude, but that amplitude is not very constrained from observations, and it is bound to have time variations. In addition, there are uncertainties in the amplitude and form of the surface poloidal flux source as well as the turbulent magnetic diffusivity. It is of interest to know how basic characteristics of a simulated sunspot cycle differ for different values of these uncertain parameters. Three prominent features of simulated cycles to focus on are its period, amplitude, and shape - the times spent in ascending and descending phases.

Figure 43 displays the variation of cycle period with circulation amplitude (panel (a)), turbulent diffusivity (panel (b)) and poloidal source amplitude (panel (c)). We see from panel (a) that as the circulation amplitude is increased, in almost all cases the period declines. This is to be expected, because in all cases, unless diffusion dominates, the period is set by the speed of the conveyor belt. The primary exception we see is that for low speeds, decreasing the circulation in the single cell case (and to much lesser degree, the case with a second weak cell at high latitudes) leads to a decrease in period. This happens because as the circulation is decreased, turbulent diffusion starts to short-circuit the conveyor belt, since some poloidal flux is diffused toward the bottom from the top before it reaches polar latitudes.

This short-circuiting effect is even more evident in panel (b), where we have plotted cycle length versus turbulent diffusivity. For the same circulation amplitude, the solutions become more diffusion dominated to the right in the figure. The periods decline, in some cases by factors of five or more. This result shows that to have a flux transport dynamo calibrated to the observed sunspot cycle period requires careful choice of the turbulent diffusivity, no matter what circulation pattern is assumed. By contrast, panel (c) shows that the cycle period is almost independent of the amplitude of the surface poloidal source. This is also expected, because the dynamo is nearly linear. Changing the poloidal source amplitude should change primarily the peak amplitude of the cycle, as we shall see below.

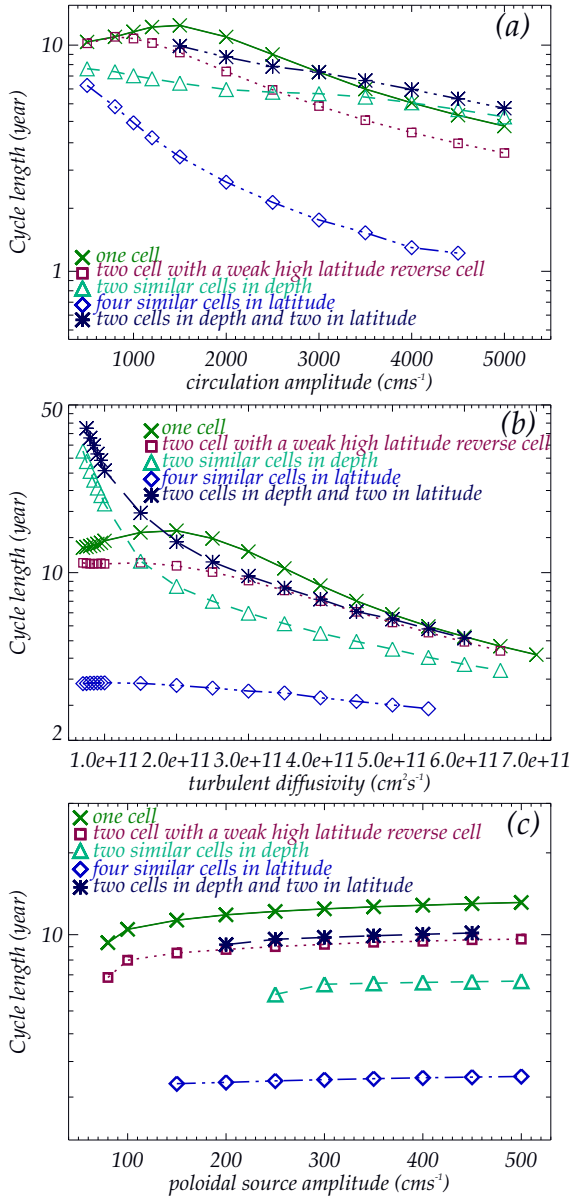

Figure 43: *Dependence of simulated sunspot cycle length on (a) amplitude of meridional circulation, (b) turbulent diffusivity and (c) amplitude of poloidal source term for the five circulation patterns used. The case of two cells in both latitude and depth is shown only for circulation amplitudes* $\geq 15\,\mathrm{ms}^{-1}$*. Below that amplitude, the solutions are quadrupolar rather than dipolar.*

(Source: Beluc et al., 2015)

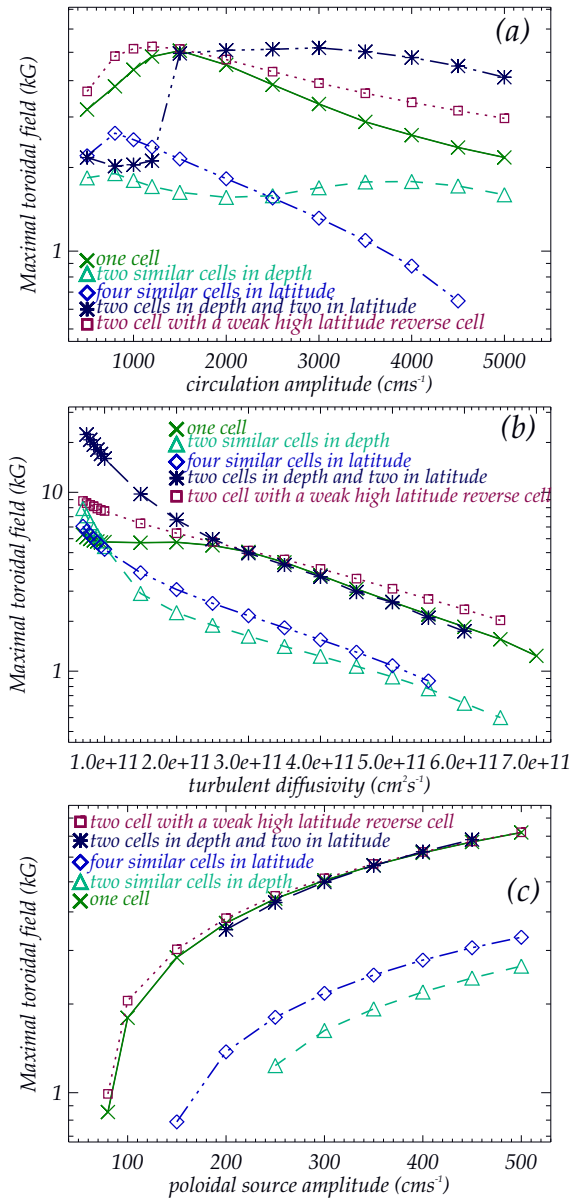

Figure 44: *Dependence of maximum toroidal field on (a) meridional circulation amplitude, (b) turbulent diffusivity and (c) amplitude of poloidal source term, for the five circulation patterns used. The sudden drop in cycle amplitude for the case of two cells in latitude and depth is due to the solution switching from dipolar to quadrupolar at a peak circulation amplitude of* $15\,\mathrm{ms}^{-1}$.

(Source: Beluczet al., 2015)

Figure 44 shows how depends the maximum toroidal field varies with meridional circulation (panel (a), turbulent diffusivity (panel (b)) and amplitude of the poloidal source term (panel (c)) for the five circulation patterns. From panel (c) we see that, as we should expect, raising the amplitude of the poloidal source raises the peak toroidal field amplitude. Because of the nonlinear quenching of the source term internal to the model, however, the amplitudes are beginning to approach asymptotic limits. Two cells in depth and four cells in latitude both generate much less toroidal field than the other patterns, which give almost the same amplitudes. In the four cell case, this is because the shearing of poloidal field is largely confined to low latitudes, where the latitudinal rotation gradient is weakest, by the short latitudinal extent of the conveyor belt, so less toroidal field is generated. In the case of two cells in depth, less of the poloidal flux gets to the bottom where the radial shear is strongest, again reducing the dynamos ability to amplify toroidal field.

In panel (b) the result that peak toroidal field declines with increasing magnetic diffusivity is simply due to the fact that there is more dissipation in the system than the induction processes in the dynamo have to overcome. Here too we see that, for all diffusivities, the configurations with four cells in latitude and two cells in depth generate less toroidal field for the same assumed diffusivity.

From panel (a) we see that the variation in peak toroidal field with changes in circulation amplitude are more complex. With two cells in depth the peak amplitude changes relatively little with circulation amplitude. With two cells in both latitude and depth, we see a similar result, except near circulation amplitude $15\,\mathrm{ms}^{-1}$ where the amplitude drops by more than 50% when the magnetic field configuration switches from dipolar to quadrupolar. In both cases, with the relatively fine scale meridional circulation pattern, the solutions are in the diffusively dominated regime, so the amplitude does not change. Meridional circulation acts mainly as a transporter of toroidal and poloidal flux, rather than as an amplifier.

The other three cases each show a largest value of toroidal field amplitude at a meridional circulation amplitude between about $8\,\mathrm{ms}^{-1}$ and $15\,\mathrm{ms}^{-1}$. At these speeds there is an optimum balance between amplification of toroidal field by differential rotation shearing, diffusive decay, and meridional transport of toroidal and poloidal flux. In each case, for larger than optimum circulation, the toroidal fields are moved in latitude and/or depth too fast to be as fully amplified; at less than optimum advection rate, more time is allowed at a given latitude and depth for the toroidal and poloidal fields to decay due to diffusion.

4.3. Parity Issue

In all the cases we have presented so far, we have found dipolar parity during the simulation time of our interest, i.e. about up to 500 years. We know that the growth rates of quadrupolar parity solutions are slightly higher than the dipolar parity in a Babcock-Leighton dynamo and the dipolar parity slowly drifts to quadrupolar one if the dynamo simulations run for more than 2000 years (Dikpati & Gilman, 2001; Bonanno et al., 2002; Hotta & Yokoyama, 2010; Miesch & Dikpati, 2014). However, (Jouve & Brun, 2007) have shown that this switching from dipolar to quadrupolar parity is very fast in the case of a four-celled meridional circulation which consists of two cells in latitude and two in depth. In our four-celled case consisting of two cells in latitude and two cells in depth (see Figure 41), the parity change did not occur so quickly. This is because the ratio of poleward surface flow-speed of the top cell to that of the bottom cell was too high, ~ 50, whereas in (Jouve & Brun, 2007) had that ratio ~ 6. In order to investigate the fast change of parity in the four-celled case, we consider a ratio of poleward surface flow-speed to poleward bottom flow-speed to be ~ 5 and simulate that case and present our results in Figures 45-46.

In Figure 45, as in earlier figures panel (b) shows the toroidal fields near the bottom of convective zone. Panel (c) depicts the surface radial field. We see here a radical change from the earlier examples. The toroidal and poloidal field patterns are now symmetric rather than antisymmetic about the equator. In other words, we have found quadrupolar type rather than dipole type parity. This difference in parity about the equator develops in just a few cycles, so the system in this case has a strong preference for quadrupole parity.

(Jouve & Brun, 2007) described when quadrupolar structure is favored as a function of meridional flow speed and diffusivity. In the case of a meridional circulation consisting of single cell in each hemisphere, (Dikpati & Gilman, 2001) discussed that slow switching to quadrupolar from dipolar parity occurs when bottom poloidal fields become weak enough after a long traversal via the conveyor-belt from surface to the bottom, and hence cannot connect with their opposite-hemisphere counterparts about the equator. A global statement would be that the quadrupole is selected when, for a particular meridional circulation, it is dissipated at a substantially lower rate than is the dipole. In other words, the growth rate for a quadrupolar mode is higher than for a dipole mode. Since a circulation pattern that has two cells in both latitude and depth is inherently more

complicated than one with a single cell, in which poloidal and toroidal flux of opposite signs and different amplitude are converged together in more places away from the equator, we expect quadrupolar symmetry to be favored, unless the upper and lower cells are very unequal in amplitude.

We find also in the low diffusivity case that having two cells in both latitude and radius leads to a quadrupolar solution (we do not produce here the time-latitude diagram for that). Therefore this fast switching from dipolar to quadrupolar parity is a typical phenomena in the four-celled meridional circulation case, irrespective of turbulent diffusivity value.

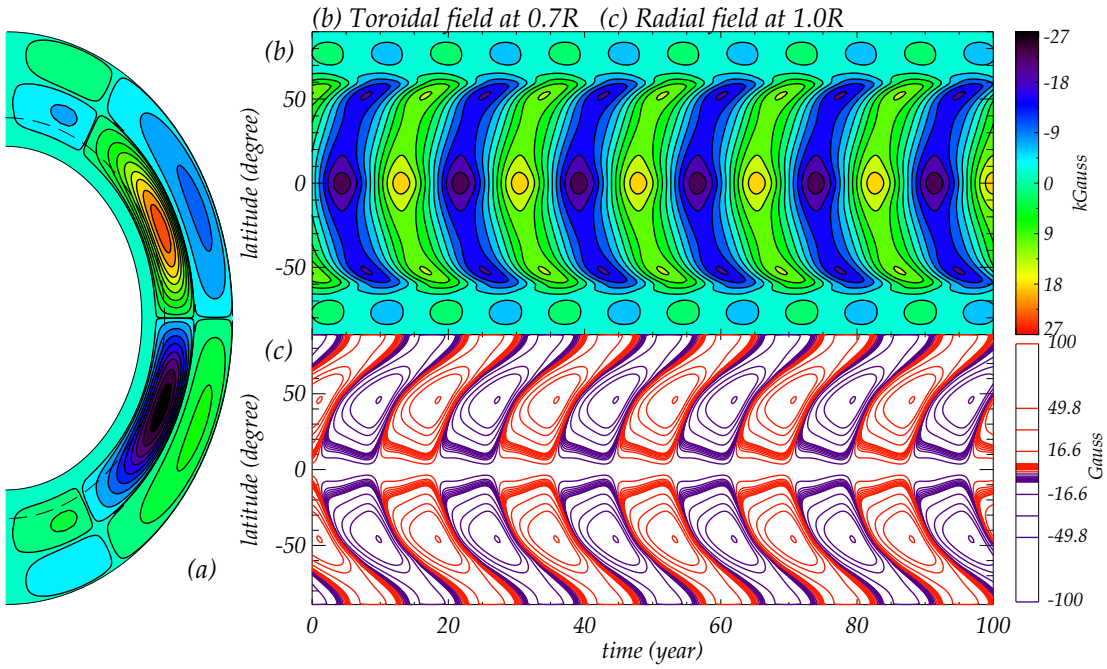

Figure 45: *Same as in Figure 41 but the bottom cell of this four-celled meridional circulation pattern has about ten times stronger poleward flow compared to that in 41a. The highest toroidal field amplitude is about* $\sim 27\,\mathrm{kG}$ *(yellow/violet). The maximum value of the radial fields is* $\pm 150\,\mathrm{G}$*, near* 50°

(Source: Belucz et al., 2015)

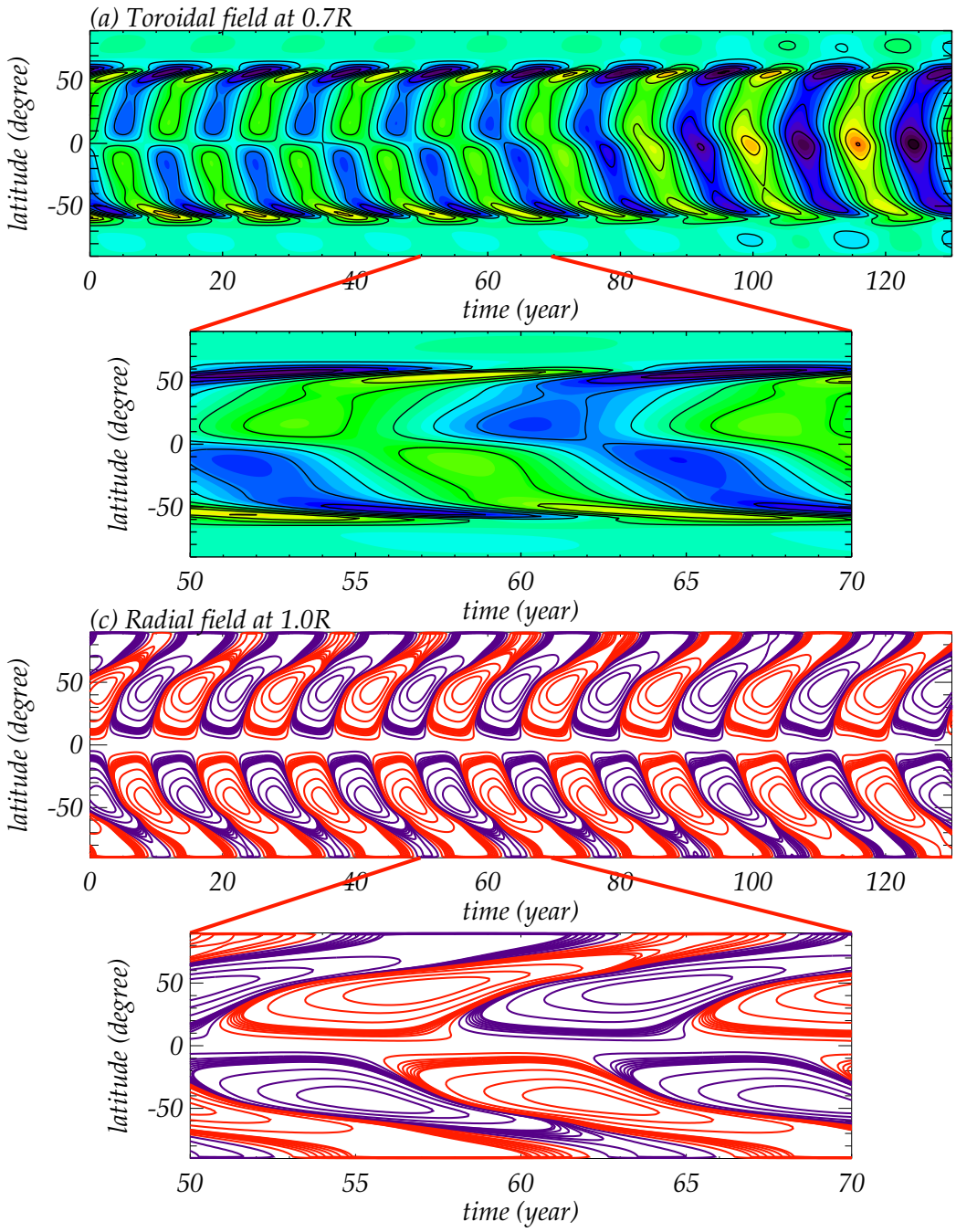

Figure 46: *Panels (a) and (c) show time-latitude diagrams for tachocline toroidal fields and surface radial fields respectively; evolution of parity from dipolar to quadrupolar is shown in enlarged form in panels (b) and (d).*

(Source: Belucz et al., 2015)

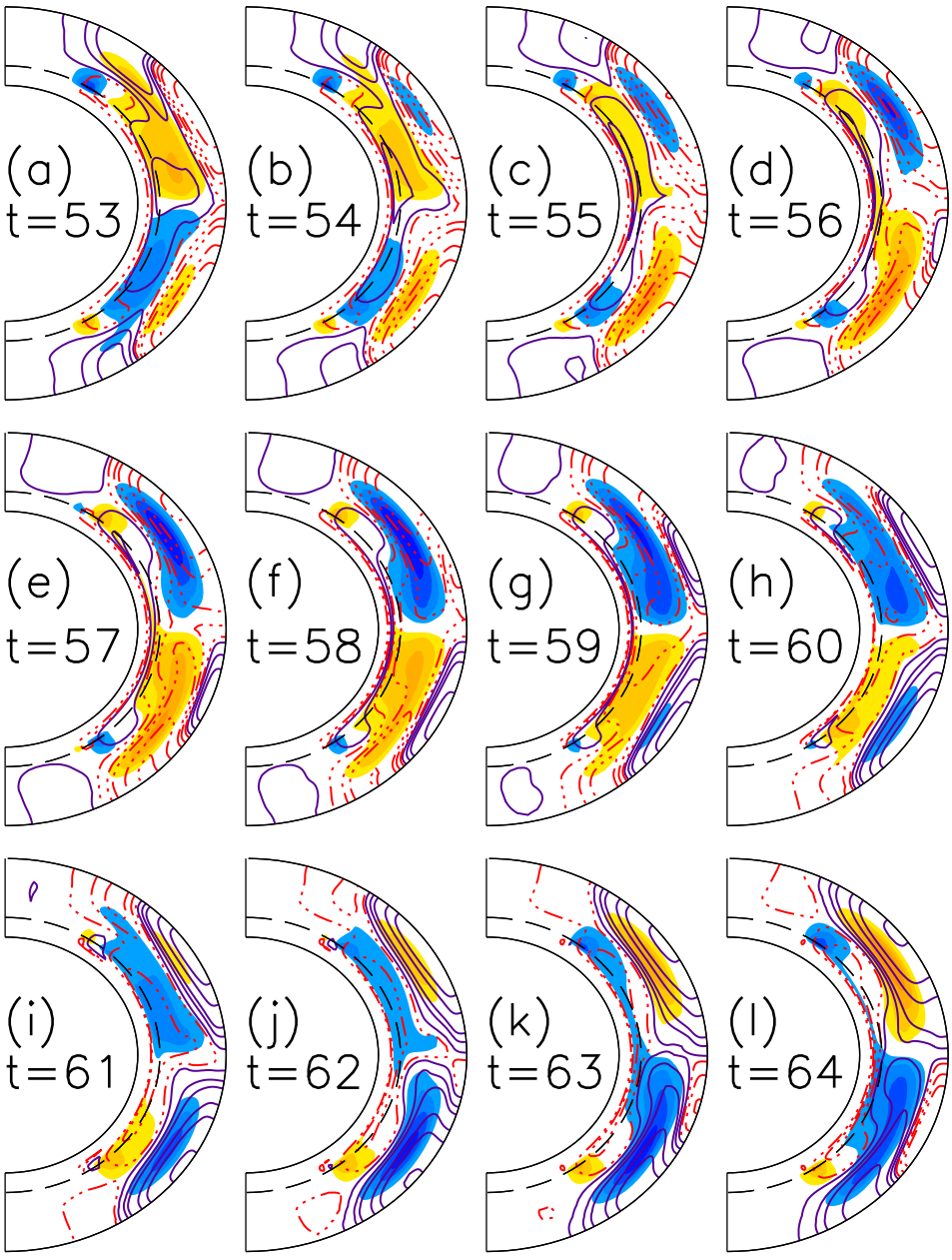

Figure 47: *Twelve snapshots of toroidal fields in orange/violet color-filled contours and poloidal fields in red (positive) and blue (negative) contours show the evolution of fields during parity change.*

(Source: Beluczet al., 2015)

Figures 46 and 47 give details of the actual transition from dipolar to quadrupolar symmetry. In Figure 46, panels (a) and (c) we see by eye that the transition occur iappears to occur in about 120 years (16-18 sunspot cycles) in the tachocline toroidal field and surface poloidal field respectively. Frames (b) and (d) show finer detail for each in the middle of this transition. The simulation was started from a previous dipole simulation, which inevitably has some slight departures from dipole symmetry at the truncation error level. The quadrupolar symmetry is so strongly preferred for the parameters chosen that even these small differences are enough to start the process of symmetry switching.

What we see in Figure 46 is a very simple process in which switching occurs by the southern hemisphere developing a phase lag relative to the northern hemisphere, which grows until the South lags by a sunspot or half magnetic cycle, with very little change in pattern in each hemisphere. Presumably in another simulation with different truncation errors, it could be the northern hemisphere that lags, ending up with the same final state.

In Figure 47, we show meridional cross-sections of both toroidal field (blue/yellow shading) and poloidal field (solid black and dashed red lines) in 1-year intervals in the middle of the transition. We can see particularly that the peak toroidal fields are moving up in the domain to a mid-depth where the flow in low latitudes is toward the equator. In addition, the polar field reversals are evolving to a state in which they go from positive to negative at both poles at the same time.

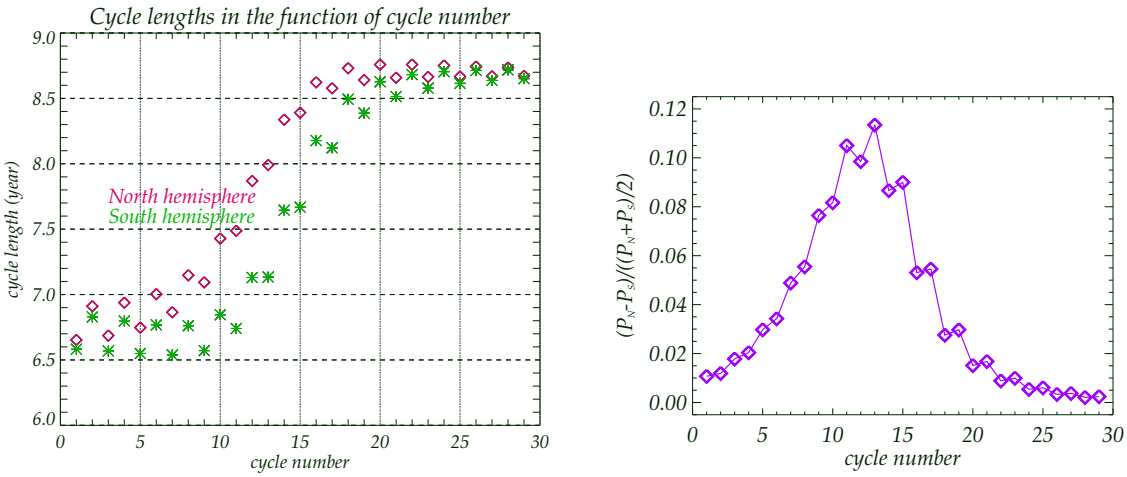

Figure 48: *Normalized difference in cycle-lengths in North and South as function of cycle number during change in dipolar to quadrupolar parity.*

(Source: Beluc et al., 2015)

We can quantify how long the transition takes by measuring the difference in cycle periods between South and North as a function of time. This result is shown in Figure 48. We see that during this transition, the North develops a phase lag relative to the South, which reaches 12% midway through the transition. What is actually happening is that the periods of both hemispheres are getting longer, from about 6.5yr to 8.5yr, but the North reaches the longer period faster than the South, so the South gains on it in phase. Therefore the difference in period length between North and South is positive.

This switching is possible because with the circulation pattern chosen, there is much less linking of flux between hemispheres at the equator. With dipole symmetry there is strong diffusion across the equator, whereas with quadrupole symmetry there is much less since both sides have the same sign of field there. Furthermore, dipole symmetry is best preserved when the toroidal fields of both signs are strongest where they are being brought into close proximity near the equator. This is guaranteed when these is single cell in depth in low and mid latitudes, with equatorward flow near the bottom where the turbulent magnetic diffusion is smaller.

5. Summary and Future Plans

The solar activity regularly affects the Sun's plasma and energetic particle populations, and these effects and changes cause the space weather that may influence long-term climate trends. Space Weather combines several research fields and important to economy because solar activities affect the Earth's climate and the advanced technology we become so dependent upon in our lives. The physical phenomena of space weather are the geomagnetic storms and substorms, ionospheric disturbances, aurora at high, middle and low latitudes, energization of the Van Allen radiation belts, and geomagnetically induced currents at Earth's surface. Coronal mass ejections and their associated shock waves can compress the magnetosphere and trigger geomagnetic storms. The CMEs and solar flares accelerate the solar energetic particles (SEP) that can damage electronics onboard spacecraft.

There has been significant interest to predicte the future solar cycles (Thompson, 1993; Badalyan et al., 2001; Dikpati et al., 2006; Du & Du, 2006; Cameron & Schssler, 2007; Javaraiah, 2007; Kane, 2007; Javaraiah, 2015). The aim of dynamo theory today, in the context of the Sun, is to understand how the dynamo actually operates to produce the magnetic fields we observe. For Cycles 22 and 23, prediction methods were primarily statistical rather than dynamical. That is, no physical laws were integrated forward in time, as in the meteorological and climate predictions. For solar cycle 24, to began in 2008, the first such dynamo-based cycle prediction, which involves integrating forward in time a form of Faradays law of electromagnetic theory, has now been made (Dikpati & Gilman, 2006).

Over the past two decades the Babcock-Leighton flux-transport solar dynamo models have been successful in reproducing many solar cycle features including equatorward migration of sunspot belts, poleward drift of poloidal fields and correct phase relationship between them (Wang & Sheeley, 1991; Choudhuri et. al., 1995; Durney, 1995; Dikpati & Charbonneau, 1999; Küker et al., 2001; Bonanno et al., 2002; Nandy & Choudhuri, 2001; Guerrero & Muñoz, 1995; Jouve et al., 2008). The models are relatively well-constrained observationally. The Babcock-Leigton flux-transport dynamo models are able to produce long-term prediction of extensive solar activity, which is of great interest in the context of long-term forecasting, and also determine the possible solar influences on terrestrial climate.

We have performed simulations of a Babcock-Leighton flux-transport dynamo model in a full-spherical shell to study the observed asymmetry in the northern and southern hemispheres and multi-cellural meridional circulation patterns suggested by solar observations and/or hydrodynamic models and simulations applied to the Sun.

The single hemisphere calculations showed how the dynamo cycle period varies as function of turbulent diffusivity, basically confirming the results that can be obtained in a classical α-Ω dynamo without meridional circulation that is the magnetic fields within the Sun are stretched out and wound around the Sun by differential rotation to creating the toroidal components and twisting of the magnetic field lines is caused to issue the poloidal component from the toroidal component.

In a full spherical shell calculations we studied the features of dynamos operating in the northern and southern hemispheres when (i) the Babcock-Leighton poloidal source terms have different amplitudes (Belucz et al., 2013), (ii) the meridional circulation amplitude, the number of circulation cells in latitude, and then in radius changes (Belucz & Dikpati, 2013).

We found that the dynamos in North and South operates mostly independently, with very little cross-talk between them. If the Babcock-Leighton source is very small or even zero in the southern hemisphere, the dynamo becomes weaker or stops cycling in the South, but the dynamo in the northern hemisphere operates unaffected.

From the next sets of dynamo simulations, for which we varied in succession the meridional circulation amplitude, the number of circulation cells in latitude, and then in radius, we have shown that the resulting properties of the magnetic cycles produced vary greatly in the South, where we applied the changes, compared with the North, which we kept steady. These changes include changes in dynamo period, shape of the butterfly diagram, strength of the polar and toroidal fields, and phase relations between polar and peak toroidal fields.

When we increase the speed of the meridional circulation, we get the expected shortening of the cycle period in the South, together with a persistent phase gain relative to the North. When the speedup occurs during the ascending phase, both the peaks of polar and toroidal fields are weakened because the poloidal flux spends less time at the pole, and the toroidal flux less time near its peak latitude, resulting in less amplification there. When we lowered the speed of meridional flow during the late declining phase of a later cycle, the cycle period in the South declined and restored the phase relation with the North, but the peak amplitudes did not change much because of the timing of the speed

change. For a speed increase that lasts for several cycles, the toroidal field peak is still weakened for the same reason as with speed increases of short duration, but the polar field peaks are not weaker. Here the surface poloidal source is weaker, but it is advected to the pole faster, reducing the loss by diffusion, so the polar field peaks are nearly the same.

When we temporarily add a second reversed meridional circulation at high latitudes, the subsequent changes in cycle properties are quite sensitive to the timing of introduction of the second cell. When it is introduced for 3 yr in the ascending phase of a cycle, the polar flux peak is weakened by the temporarily equatorward flow near the outer boundary, and the toroidal flux peak that follows is weakened because some of the poloidal flux made available near the bottom is advected toward the pole there rather than toward the equator when there is only the primary cell present. Both cause the rising phase of that cycle to lengthen in time. By contrast, when later a second reversed cell is introduced in the late declining phase, the cycle is actually sped up because we more poloidal flux near the bottom at lower latitudes earlier. When the second cell lasts for several cycles, we get a persistent polar branch of the butterfly diagram (which is not observed on the Sun) and weaker polar field peaks because it is harder for low latitude poloidal flux to get to the pole.

When we introduce a second meridional circulation cell with depth, the changes in the toroidal field and butterfly diagram are particularly large. The butterfly wings reverse in direction for the duration of the second cell. The polar field peaks are particularly sensitive to timing, with the peak decreasing when the second cell occurs during the ascending phase and increasing when the second cell is added during the late declining phase. The amplitude changes persist only while the second cell is present, but the phase differences with the North persist for a much longer time. When the second cell in radius is present for several cycles, then much more radical changes occur. The butterfly diagram moves far away from the observed one, and even the dynamo periods are quite different between low and high latitudes in the South. Low latitude periods get much longer because the poleward flow near the bottom and the "α-Ω" dynamo wave effect near the bottom nearly cancel each other in low latitudes, while they add in high latitudes. Polar field peaks are always lower because their toroidal source is always lower.

The changes in meridional flow we have used all fall within the range of possible solar circulations. An analysis of (Ulrich, 2010) indicates an amplitude variation of up to $\sim$50% and an appearance and disappearance of a second high-latitude reverse cell, whereas a

recent analysis of (Zhao et al., 2013) shows evidence of a second cell in depth. Our results reinforce the need to measure meridional circulation in the Sun as accurately as possible at all latitudes and depths within the convection zone, and for long time periods. It also reinforces the need for time dependent theories of solar meridional circulation that can tell us theoretically how this circulation may change its amplitude and form in each hemisphere. It is important to realize that all the changes in cycle properties are produced using a surface poloidal source function that varies the surface poloidal source only in response to changes in the toroidal field at the bottom. In the Sun, surface poloidal fields could change due to changes in other processes not included in the surface source. The results also show that in this class of solar dynamo, the North and South are linked very weakly, since the North experienced virtually no change from all the changes occurring in the South over several decades. In the Sun, the kinds of changes we have introduced in the South should be occurring in both the South and the North, not necessarily well correlated between hemispheres. Nevertheless, it is apparent from longterm solar observations that the differences in cycle phase between the North and the South are never large enough to negate the basic antisymmetric pattern of polar and spot fields. Therefore, there must be some limit to the differences in circulation behavior in the two hemispheres.

Finally, it worth noting that our results suggest it is unlikely that there can be a second meridional circulation cell with depth that persists for more than a few years, if the Sun is a flux transport dynamo, because if there were a very persistent second cell with reversed flow at the bottom, the butterfly diagram would look very different than that observed for the Sun and there would be large changes in the dynamo period, particularly in low and middle latitudes where it is well observed. But from these simulations we can see that we cannot rule out the possibility that a second cell in radius is present for a few years at a time, because the presence of such a second cell for a few years does not radically change the solar cycle patterns from a flux transport dynamo. Note that second cell in depth found by (Zhao et al., 2013) is from the analysis of about two years SDO/HMI data. However, it is yet to be seen whether the second cell in depth persists for a solar cycle timescale or longer.

Finally, we have compared flux-transport dynamo model results for five meridional circulation patterns that may occur in the solar convection zone, as suggested by solar observations and/or hydrodynamic models and simulations applied to the Sun (Belucz et al., 2015). We carried out simulations for both diffusion and advection dominated regimes. Only the circulation pattern is different in each simulation; all other physical

processes included are the same. We find a wide variety of dynamo behavior, as measured by simulated time-latitude diagrams of toroidal and poloidal fields.

In general, circulation patterns with only one cell in depth and no more than two cells in latitude produce the most solar like butterfly diagrams. Two cells in depth leads to antisolar butterflies from tachocline toroidal fields, but solar like butterflies at mid-depth where both cells have equatorward flow. For this pattern to work for the Sun physical mechanisms must exist to inhibit magnetic buoyancy there long enough to allow enough amplification of toroidal fields to produce spots, while preventing tachocline toroidal fields from reaching the solar surface in any observable form. Four cells in latitude leads to some solar-like magnetic patterns, but very fast cycle periods compared to the Sun. Surface Doppler measurements also do not support the existence of four cells distributed evenly in latitude, though multiple cells confined to polar latitudes can not be ruled out. All of the solutions we have found retain dipole or solar-like symmetry about the equator, except the case of two circulation cells in latitude and depth when the upper and lower cell amplitudes differ by less than a certain amount. In that case, starting from a small difference between hemispheres (probably truncation), even when starting from essentially dipole symmetry, the solution switches to quadrupole type within several magnetic cycles and stays there. This switch is achieved simply by one hemisphere temporarily changing its period relative to the other until the relative phase changes by one-half cycle, without changing the pattern itself in either hemisphere. A milder version of this effect could be partly responsible in the Sun for differences in phase between northern and southern hemispheres that do not go so far as to switch the dominant symmetry observed, which is dipolar.

Despite producing significantly different butterfly diagrams for toroidal and poloidal fields, our flux transport dynamo simulations with different meridional circulations have many properties in common, as revealed by our parameter survey. In almost all cases for all paramters chosen, cycle length declines with increasing circulation amplitude and increasing turbulent magnetic diffusivity, but is nearly independent of poloidal source amplitude. Maximum fields generated decline with increasing diffusivity, but increase with poloidal source amplitude. Only changes in circulation amplitude produce a variety of changes in peak fields for different circulation patterns.

There are at least two important effects related to MHD turbulence that we have not included in the model we have used, that we need to examine in future studies. Both would add nonlinearities to the system. One is the so-called turbulent pumping mechanism

(see (Guerrero et al., 2009) and references therein), and the other is diffusivity quenching (Guerrero & de Gouveia Dal Pino, 2008). It is currently not known how these effects would change dynamo behavior for the full range of circulation patterns we have considered here.

In forthcoming papers, we propose to calibrate and improve the our dynamo model to simulate the observed activity cycles and stellar dynamos the solar-type cool dwarf stars and define the best ingredients to a calibrated solar dynamo model to predict of future solar cycles.

Because of Sun's proximity, it is an excellent target for studying magnetic cycles on different time and wavelengths. The magnetic fields present in the Sun, and in similar stars with deep surface convection zones, are believed to be generated by a hydrodynamic dynamo. A model of the solar dynamo should also simulate the stellar dynamos of solar-type cool dwarf stars, able to accurate predictions of the solar cycle, and determine the ingredients to a calibrated solar dynamo model for prediction of future solar cycles. The lengths of stellar data sets are much shorter than that of the Sun, the data sets are ideal to calibrate a stellar dynamo model and study the magnetic cycles of stars.

We will evaluate and calibrate the 2D Babcock-Leighton dynamo model (Belucz et al., 2015) to simulate the cycles of solar-type star using ground- and space-based data of stellar activity as well as differential rotation. We will use guidance from available observations (Frasca et al., 2010; Kővári & Oláh, 2014; Kővári et al., 2015) as well as theoretical concepts to specify values for the needed dynamo ingredients, as differential rotation, density profile and diffusivity profile. Rotation of many solar-type stars is fairly well-known from observations, and convection thickness is well constrained by stellar interior structure models. Surface differential rotation is also available for some. From these parameters and convection simulations we constrain $\Omega(r, \Theta)$ to different categories likely to occur in solar-type stars, such as equatorial, mid-latitude and polar acceleration, deceleration and accompanying meridional circulation. Plausible turbulent diffusivities and α-effects can be inferred from available Doppler broadening data for stellar turbulence together with guidance from convection models and active region decay times.

We propose a 3D Babcock-Leighton flux-transport dynamo model to simulate active longitudes, couple shallow-water model of the tachocline (Dikpati & Gilman, 2005) and the 2D Babcock-Leighton dynamo model (Belucz et al., 2015) by the bottom boundary condition in the overshoot tachocline zone. We estimate the axisymmetric component of longitude-dependent Babcock-Leighton source. We develop a 3D Babcock-Leighton flux-transport dynamo model to interpret the longitudinal concentrations of enhanced solar

activity known as active longitudes determined by sunspot groups and the longitudinal distribution of macrospicules.

(Gyenge et al., 2016) show connection between active longitude and flare activities with a similar short time-scale periodicity, very important for Space Weather. For more than half a century, it has been observed that solar active regions tend to emerge near the location of previous or currently existent magnetic flux (Gaizauskas et al., 1983; Brouwer & Zwaan, 1990; Harvey & Zwaan, 1919). These preferential longitudes of solar activity are commonly referred to as Active Longitudes, and have been observed some cool, active stars and young solar analogs (Olah et al., 1991; Lanza et al., 2009; García-Alvarez et al., 2011).

(Gyenge et al., 2015) found statistical relationships between the active longitude determined by sunspot groups and the longitudinal distribution of macrospicules. The latitudinal distribution of macrospicules concentrates around the poles, but the longitudinal distribution of macrospicules shows inhomogeneous properties and concentrates certain belts suggest that there is a relationship between the position occurrence and the generation of the global magnetic field. Coronal holes are related to the Sun's large-scale poloidal field (Gonzalez & Schatten, 1987; Bravo & Otaola, 1990) and macrospicules observed at the limb in polar coronal holes. Finding connections between the latitude distribution of sunspots and macrospicules and the relationship between macrospicules formation and the solar dynamo would be a great step for a better physical understanding of these phenomena. We will build and develop a 2D axisymmetric mean-field dynamo (Simard et al., 2013) with solar rotation profiles (derived from helioseismology) incorporate the alpha-effect using the 3D EULAG-MHD to verify the suggestion that there is a relationship between the position occurrence of macrospicules and the generation of the global magnetic field.

References

Babcock, H.W., 1961, *ApJ, 133, 572*

Babcock, H. W. & Cowling, T. G., 1953, *MNRAS, 113, 357*

Badalyan, O.G.; Obridko, V. & Sykora, N.J., 2001, *Solar Phys. 199, 421*

Bankoti, N. S.; Joshi, N. C.; Pande, S.; Pande, B. & Pandey, K., 2010, *NewA, 15, 561*

Basu, S. & Antia, H.M., 2010, *ApJ, 717, 488*

Belucz B.; Forgács-Dajka E. & Dikpati, M., 2013, *AN, 334, 960*

Belucz B. & Dikpati, M., 2013, *ApJ, 779, 4*

Belucz B.; Dikpati, M. & Forgács-Dajka E., 2015, *ApJ, 806, 169*

Bethe, H.A. & Critchfield, C.L., 1938, *Phys. Rev. 54, 248*

Biermann, L., 1941, *Vierteljahresschrift der Astronomischen Gesellschaft, 76, 194-200*

Bonanno, A.; Elstner, D.; Rüdiger, G. & Belvedere, G., 2002, *ApJ, 390, 673*

Bonanno, A.; Elstner, D.; Belvedere, G. & Rüdiger, G., 2005, *AN, 326, 170*

Bravo, S. & Otaola, J. A., 1989, *Solar Phys., 122, 335*

Braun, D.C. & Fan, Y., 1998, *ApJ, 508, 105*

Brouwer, M. P. & Zwaan, C., 1990, *Solar Phys., 129, 221*

Brown, T. M., Christensen-Dalsgaard, J., Dziembowski, W. A., Goode, P. R., Gough, D. O., & Morrow, C. A., 1953, *ApJ, 343, 526*

Cameron, R. & Schssler, M., 2007, *ApJ, 659, 801*

Carrington, R.C., 1858, *MNRAS, 19, 1*

Carrington, R.C., 1860, *MNRAS, 20, 13*

Carrington, R.C., 1863, *Observations of the Spots on the Sun, 221, 244*

Charbonneau, P.; Tomczyk, S.; Schou, J. & Thompson, M.J., 1998, *ApJ, 496, 1015*

Charbonneau, P., 2007, *Advances in Space Research 39, 1661*

Charbonneau, P., 2010, *Living Rev. Solar Phys., 7, 3*

Charbonneau, P.; Beaubien, G. & St-Jean, C., 2007, *ApJ, 658, 657*

Choudhuri, A. R.; Schussler, M. & Dikpati, M., 1995, *A&A, 303, L29*

Chowdhury, P.; Choudhary, D. P. & Gosain, S., 2013a, *ApJ, 768, 188*

Chowdhury, P.; Kudela, K. & Diwedi, B. N., 2013b, *Solar Phys., 286, 577*

Cliver, E.W., 2005, *Advances in Space Research, 38, 119-129*

Corbard, T.; Jimnez-Reyes, S.J.; Tomczyk, S.; Dikpati, M. & Gilman, P., 2001, in Helio- and Asteroseismology at the Dawn of the Millennium, *ESA Publ. SP-464, 265*

Cowling, T.G., 1934, *MNRAS, 94, 39*

Dikpati, M., 2014, *MNRAS, 438, 2380*

Dikpati, M. & Choudhuri, A.R., 1994, *A&A, 291, 975*

Dikpati, M. & Charbonneau, P., 1999, *ApJ, 518, 508*

Dikpati, M.; de Toma, G. & Gilman, P.A., 2006, *Geophys. Res. Lett. 33, L05102*

Dikpati, M.; de Toma, G.; Gilman, P.A.; Arge, C.N. & White, O.R., 2004, *ApJ, 601, 1136*

Dikpati, M.; Gilman, P.A. & de Toma, G., 2008, *ApJ Lett., 673, L99*

Dikpati, M.; Gilman, P.A.; de Toma, G. & Ulrich, R.K., 2010, *Geophys. Res. Lett., 37, L14107*

Dikpati, M., Gilman, P.A., & MacGregor, K.B., 2006, *ApJ, 638, 564*

Dikpati, M., & Gilman, P.A., 2001, *ApJ, 559, 428*

Dikpati, M., & Gilman, P.A., 2005, *ApJ, 635, 193*

Dikpati, M., & Gilman, P.A., 2006, *ApJ, 649, 498*

Dikpati, M., & Gilman, P.A., 2008, *JApA, 29, 29*

Dikpati, M., & Gilman, P.A., 2012, *ApJ, 746, 65*

Du, Z. & Du, S., 2006, *Solar Phys., 238, 431*

Durney, B. R., 1995, *Solar Phys., 160, 213*

Evershed, J., 1909, *The Observatory, 32, 291*

Featherstone, N. & Miesch, M. S., 2015, *ApJ, 804, 67*

Forgács-Dajka, E. & Petrovay, K., 2002, *A&A, 389, 629*

Foukal, P.V., 2004, *Solar Astrophysics*, Second, Revised Edition, WILEY-VCH Verlag CmbH & Co. KCaA

Frasca, A.; Biazzo, K.; Kővári, Zs.; Marilli, E. & Cakirli, Ö., 2010, *A&A, 518A, 48*

Gaizauskas, V.; Harvey, K. L.; Harvey, J. W. & Zwaan, C., 1983, *ApJ, 265, 1056*

García-Alvarez, D.; Lanza, A. F.; Messina, S.; Drake, J. J.; van Wyk, F.; Shobbrook, R. R.; Butler, C. J.; Kilkenny, D.; Doyle, J. G. & Kashyap, V. L., 2011, *A&A, 533, 30*

Gizon, L. & Birch A.C., 2005, *Living Rev. Solar Phys., 2, 6*

Gnevyshev, M.N. & Ohl, A.I., 1948, *Astron. Zh., 25, 18*

Gonzalez, G. & Schatten, K. H., 1987, *Solar Phys., 114, 189*

Guerrero, G. & de Gouveia Dal Pino, E.M., 2008, *A&A, 485, 267*

Guerrero, G.; Dikpati, M. & de Gouveia Dal Pino, E.M., 2009, *ApJ, 701, 725*

Guerrero, G. & Muñoz, J. D., 2004, *MNRAS, 350, 317*

Guerrero, G. A.; Smolarkiewicz, P. K.; Kosovichev, A. G. & Mansour, N. N., 2013, *ApJ, 779, 176*

Gyenge, N.; Bennett, S. & Erdélyi, R., 2015, *JApA, 36, 103*

Gyenge N.; Ludmány A. & Baranyi T., 2016, *ApJ, 818, 127*

Haber, D.A.; Hindman, B.W.; Toomre, J.; Bogart, R.S.; Larsen, R.M. & Hill, F., 2002, *ApJ, 570, 855*

Hale, G.E., 1908, *ApJ, 28, 315*

Hale, G.E.; Ellerman, F.; Nicholson, S.B. & Joy, A.H., 1919, *ApJ, 49, 153*

Harvey, K.L. & Zwaan, C., 1993, *Solar Phys., 148, 85*

Hathaway, D.H.; Gilman, P.A.; Harvey, J.W.; Hill, F.; Howard, R.F.; Jones, H.P.; Kasher, J.C.; Leibacher, J.W.; Pintar, J.A. & Simon, G.W., 1996, *Science, 272, 1306*

Hathaway, D.H., 2010, *Living Rev. Solar Phys., 7, 1*

Hathaway, D. H., 2015, *Living Rev. Solar Phys., 12, 4*

Hazra, G.; Karak, B.B. & Choudhuri, A.R., 2014, *ApJ, 782, 93*

Hotta, H. & Yokoyama, T., 2010, *ApJ, 714, L308*

Javaraiah, J., 2007, *MNRAS, 377, L34*

Javaraiah, J., 2015, *New Astronomy, 34, 54*

Joshi, B. & Joshi, A., 2004, *Solar Phys., 219, 343*

Jouve, L. & Brun, A.S., 2007, *A&A, 474, 239J*

Jouve, L.; Brun, A.S.; Arlt, R.; Brandenburg, A.; Dikpati, M.; Bonanno, A.; Käpylä P.J.; Moss, D.; Rempel, M.; Gilman, P.A.; Korpi, M.J. & Kosovichev, A.G., 2008, *A&A, 483, 949*

Kane, R.P., 2007, *Solar Phys. 243, 205*

Kholikov, S.; Serebryanskiy, A. & Jackiewicz, J., 2014, *ApJ, 784, 145*

Kitchatinov, L.L. & Rüdiger, G., 2005, *AN, 326, 379*

Komm, R.; González-Hernández, I.; Hill, F.; Bogart, R.; Rabello-Soares, M.C. & Haber, D., 2012, *Solar Phys., 287, 85*

Kővári, Zs.; Kriskovics, L.; Künstler, A.; Carroll, T. A.; Strassmeier, K. G.; Vida, K.; Oláh, K.; Bartus, J. & Weber, M., 2015, *A&A 573, 98*

Kővári, Zs. & Oláh, K., 2014, *SSRv, 186, 457*

Küker, M.; Rüdiger, G. & Schultz, M., 2001, *A&A, 374, 301*

Langley, S.P., 1874, *Am. J. of Sci., Series 3, 7, 87*

Lanza, A.F.; Aigrain, S.; Messina, S.; Leto, G.; Pagano, I.; Auvergne, M.; Baglin, A.; Barge, P.; Bonomo, A.S.; Collier Cameron, A.; Cutispoto, G.; Deleuil, M.; de Medeiros, J.R.; Foing, B. & Moutou, C., 2009, *A&A 506, 255*

Leighton, R.B., 1964, *ApJ, 140, 1547*

Li, K.J.; Wang, J.X.; Xiong, S. Y.; et al., 2002, *A&A, 383, 648*

Maunder, E.W., 1904, *Popular Astronomy, 12, 616*

McIntosh, P., 1990, *Solar Phys., 125, 251*

Meadows, A.J., 1970, *Early Solar Physics*

Miesch, M.S. & Dikpati, M., 2014, *ApJ, 785, L8, 5*

Nair, V.S.; & Nayar, S.R.P., 2008, *IJRSP, 37, 391*

Nandy, D. & Choudhuri, A.R., 2001, *ApJ, 551, 576*

Olah, K.; Hall, D.S. & Henry, G.W., 1991, 1991, *A&A 251, 531*

Parker, E.N., 1955, *ApJ, 122, 293*

Priest, E.R., 2014, *Solar Magnetohydrodynamics*, ISBN 978-0-521-85471-9

Rempel, M.; Dikpati, M. & MacGregor, K.B., 2005, *in Proc. 13th Cambridge Workshop on Cool Stars, Stellar Systems and the Sun*, ed. F. Favata, G.A.J. Hussain, & B. Battrick (ESA SP-560)

Ribes, J.C. & Nesme-Ribes, E., 1993, *A&A, 276, 549*

Schad, A.; Timmer, J., & Roth, M., 2013, *ApJ, 778, L38*

Schou, J. & Bogart, R.S., 1998, *ApJ, 504, L31*

Schrijver, C.J. & Liu, Y., 2008, *Solar Phys., 252, 19*

Schwabe, S.H., 1843, *AN, 21, 233*

Simard, C.; Charbonneau, P. & Bouchat, A., 2013, *ApJ, 768, 18*

Solanki, S.K., 2003, *The Astron Astrophys Rev 11, 153*

Spörer, G., 1889, *Nova Acta der Ksl. 53, 283*

Thomas, J.H.; Weiss, N.O.; Tobias, S.M. & Brummell, N.H., 2002, *Nature 420, 390*

Thompson, R.J., 1993, *Solar Phys. 148, 383*

Ulrich, R.K., 2010, *ApJ, 725, 658*

Verma, V.K., 1993, *ApJ, 403, 797*

Verma, V.K., 2000, *Astrophys. Astr. 21, 173*

Vernova, E.S.; Mursula, K.; Tyasto, M.I. & Baranov, D.G., 2002, *Solar Phys., 205, 371*

Waldmeier, M., 1935, *Astron. Mitt. Zurich, 14(133), 105*

Waldmeier, M., 1939, *Astron. Mitt. Zurich, 14(138), 470*

Wang, Y.M.; Sheeley, N.R., Jr. & Nash, A.G., 1991, *ApJ, 383, 431*

Wang, Y.M. & Sheeley, N.R., Jr., 1991, *ApJ, 375, 761*

Wolf, R. & Brunner W., 1936, *MiZur, 14, 137-190, 15*

Yuhong, F., 2009, *Living Rev. Solar Phys., 6, 4*

Zhao, J.; Hartlep, T.; Kosovichev, A.G. & Mansour, N.N., 2009, *ApJ, 702, 115*

Zhao, J.; Bogart, R.S.; Kosovichev, A.G.; Duvall, T.L. & Hartlep, T., 2013, *ApJ, 774, L29*

List of Figures

Acknowledgements

I would like to share my gratitude and appreciation for her encouragement to my supervisior, Dr. Emese Forgács-Dajka who was an inspiration to me. I am grateful to have the opportunity to work with her. She supports me through thick and thin. Many thanks Emese.

This is the best way to say thank you to my terrific co-supervisor, Dr Mausumi Dikpati who I admire in so many ways and who is an amazing mentor. I see her as a friend, and a colleague also. She is a wealth of knowledge and a renowned expert in her fields. I've learned a lot from her and consider myself very fortunate to have her as a co-supervisor. She allows me to get a world-class education and become part of the scientific community. The days working with her in Boulder will be my most treasured memory. Thank you, Mausumi!

Most importantly, none of this would have been possible without the love and support of my family. They have maintained a constant source of love, concern, patience and strength all these years. I would like to represent my heart-felt gratitude to my husband, my daughter, my parents, my siblings and my grandparents.

I would like to share my gratitude to my colleagues and many friends for their support and friendship at Department of Astronomy. Specifically, I am grateful to Dr. Kristóf Petrovay for helpful comments and constructive criticisms what were thought-provoking and they helped me focus my ideas. Thanks to Professor Robertus Erdlyi for his encouragement, belief in me and opportunity that I became a member of the staff at Debrecen Heliophysical Observatory. I am also grateful to the staff at the Eötvös Lorand University for their support and friendship during my graduate study.

Finally, I gratefully acknowledge for the funding received from University Corporation for Atmospheric Research and from the High Altitude Observatory of the National Center for Atmospheric Research. My work was partially supported by NASAs Living With a Star program too. Special thanks to Dr. Mausumi Dikpati and the researchers of NCAR HAO who made the few months in Boulder wonderful. I thank the anonymous referees for very helpful comments which have helped improve the papers significantly.